1 cm

Department of Precision and Microsystems Engineering

Fabrication of a glass microfluidic gas exchanger using a femtosecond laser

J.H. (Jelle) Smit

Report no   : 2024.024
Coach   : Z. (Zhilin) Wang & N.J.H. (Harold) Raat
Professor   : M.K. (Murali) Ghatkesar
Specialisation   : Micro- and Nano Engineering (MNE)
Type of report   : Design Report
Date   : 16 May 2024

MSc Thesis report in Mechanical Engineering

Fabrication of a glass microfluidic gas exchanger using a femtosecond laser

Jelle Haye Smit

May 2024

To obtain the degree of Master of Science at the Delft University of Technology, to be defended publicly on Friday, May 31, 2024, at 9:00 AM.

Thesis Committee:
M.K. (Murali) Ghatkesar, TU Delft
Z. (Zhilin) Wang, TU Delft
N.J.H. (Harold) Raat, Erasmus Medical Center

Report number: 2024.024
Student Number: 4713303
Master Track: High-Tech Engineering (HTE)
Specialization: Micro-and Nano Engineering (MNE)

Type of Report: Design Report

Summary

The iMicrofluidics research collaboration, involving TU Delft, Erasmus Medical Center, and Bronkhorst High Tech B.V., endeavors to create an integrated, portable, and incubator-free Organ-on-Chip (OoC) platform. Building on previous achievements, such as the development of a portable microfluidic platform by Zhu et al. (2020)[54] and an Arduino-controlled heating mechanism by El Hassan et al. (2023)[20], the initiative focuses on addressing the critical parameter of dissolved oxygen regulation. This thesis project explores using femtosecond (Fs) laser fabrication to produce a microfluidic gas exchanger, crucial for oxygen regulation and advancing the incubator-free OoC platform.

The project begins with the design of a sandwich-structured gas exchanger using SolidWorks, followed by simulations using COMSOL Multiphysics to assess flow dynamics, diffusion, and membrane deformation. Minimizing membrane deformation to prevent channel blockages or leakages is emphasized. An alignment tool is then designed and 3D printed to aid in accurately aligning the layers of the sandwich structure.

Next, systematic optimization of Fs laser fabrication settings is conducted for through holes and channel engravings. Characterization using a Keyence digital microscope, including 3D imaging and surface roughness analysis, confirms the optimal settings' ability to replicate the desired design from simulations accurately. These settings are then applied to fabricate the gas exchanger device and integrate the optical oxygen sensor.

The assembly process involves a specific protocol, including plasma bonding, heat treatment, and glue bonding of connection ports. Testing reveals leak-free gas and liquid flow, albeit with limitations in gas flow rates, restricting the system to air or pure nitrogen input gases. Furthermore, the gas exchanger exhibits slower response times and reaches equilibrium at unexpected oxygen concentrations, indicating less efficiency than anticipated. Operator-induced errors, such as loose connectors, significantly impact oxygen regulation, highlighting the need for further research on gas-tight connections.

In conclusion, while Fs fabrication shows promise, challenges like glass debris clogging and dimensional losses during fabrication persist. Sensor integration is successful, but the gas exchanger requires additional testing and validation for more robust conclusions, particularly regarding its reliability in real cell applications at 37°C. Future work includes biomedical validation and addressing issues like bubble formation to enhance system functionality.

Contents

List of Figures

1. Background

This chapter delves into existing research and essential background theories necessary to provide context before delving into the main thesis article.

1.1. iMicrofluidics research

A joint effort between TU Delft, Erasmus Medical Center, and Bronkhorst High Tech B.V. explores the feasibility of creating a portable, integrated, incubator-free Organ-on-Chip (OOC) platform. Within this collaboration, Zhu et al. (2020) devised a prototype portable microfluidic platform, subsequently dubbed "Haoyu's platform," representing an initial stride towards a compact, modular, integrated system capable of emulating various organs. This platform enables automatic control and switching between liquid and gas flow [54], as illustrated in Figure 1.
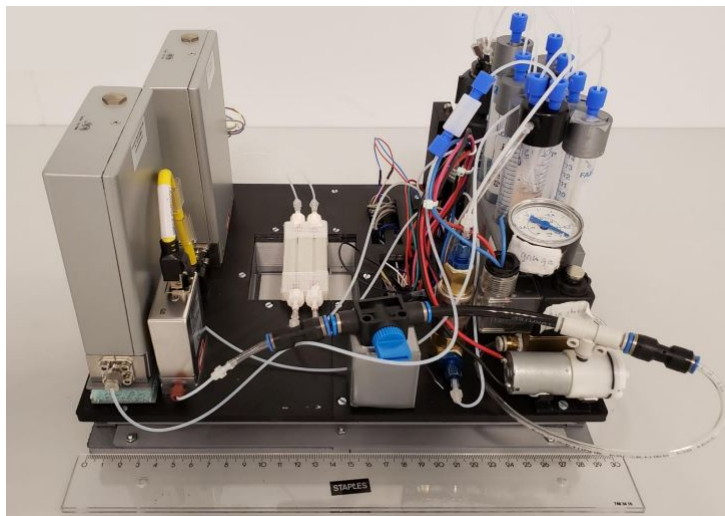
Figure 1.: Haoyu's platform, adjusted from [54]

Subsequently, an Arduino-controlled heating mechanism incorporating Peltier elements is developed to precisely regulate the temperature of the microfluidic chip. This heating mechanism, depicted in Figure 2, was devised by El Hassan et al. (2023) within the framework of the iMicrofluidics project. Proportional-integral-derivative
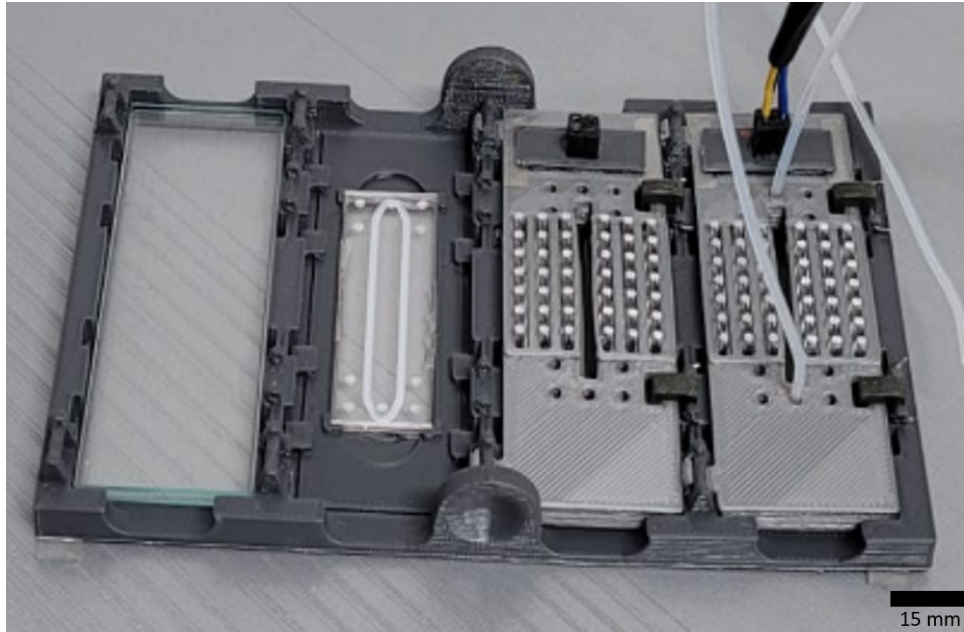
Figure 2.: Chip heating element [20]

(PID) control is employed to mitigate temperature fluctuations and fine-tune the input voltage and heating rate. A Resistance Detector Sensor (RTD) is used to measure the real-time temperature outside the chip but within the core of the microfluidic chip. A printed circuit board (PCB) facilitates voltage amplification for other system components. El Hassan et al. (2023) provide detailed argumentation regarding the selection of Peltier elements, PID control, and other design choices in their thesis report [20]. This contribution brings us one step closer to an incubator-free OoC system.

1.2. Biological background

1.2.1. Liver physiology and functions

This chapter will discuss essential background information regarding liver physiology and functions to enhance comprehension of this intricate organ. Given that liver cells will be the focus of research in the iMicrofluidics project, it is imperative to understand how to accurately replicate the liver microenvironment.

1.2.2. Liver functions and cell types

The liver is one of the largest, most important organs of the human body [1][16][33]. The liver is located in the upper-right abdomen, underneath the rib cage. A human liver has around 500 vital functions, among which [50][9][16][1][33]:

- Metabolism: The liver helps to metabolize fats, carbohydrates, and proteins. It also plays a role in the metabolism of medications and other substances.

- Detoxification: The liver helps to detoxify the body by removing harmful substances, such as alcohol and drugs, from the bloodstream.

- Production of bile: The liver produces bile, which is necessary for digesting fats and the absorption of fat-soluble vitamins.

- Storage: The liver stores several important substances, including glycogen (a source of energy), vitamins, and minerals.

- Blood sugar regulation: The liver helps to regulate blood sugar levels by releasing glucose into the bloodstream when needed and storing excess glucose as glycogen.

- Blood clotting: The liver plays a role in the production of clotting factors, which are necessary to form blood clots.

For optimal performance of these tasks, a constant blood supply is necessary [45]. The liver has a double blood supply, with oxygen-rich blood from the heart entering the liver from hepatic arteries and oxygen-poor blood from the gastrointestinal tract, spleen, pancreas, and gallbladder entering the liver from the liver portal vein as shown in figure 3 [12][1]. Filtered blood leaves the liver deoxygenated by hepatic veins back to the heart.

The liver has 4 primary lobes or sections, which are separated from each other by connective tissue, which contains cells that produce extracellular matrix (ECM)[35]. Thousands of hexagonally-shaped lobules make up these liver lobes. These lobules are small liver segments of blood vessels, bile ducts, sinusoids, and liver cells [9]. An overview of a lobule is shown in figure 3. As the blood flows through the liver, it comes into contact with the hepatocytes and other cells within the liver.
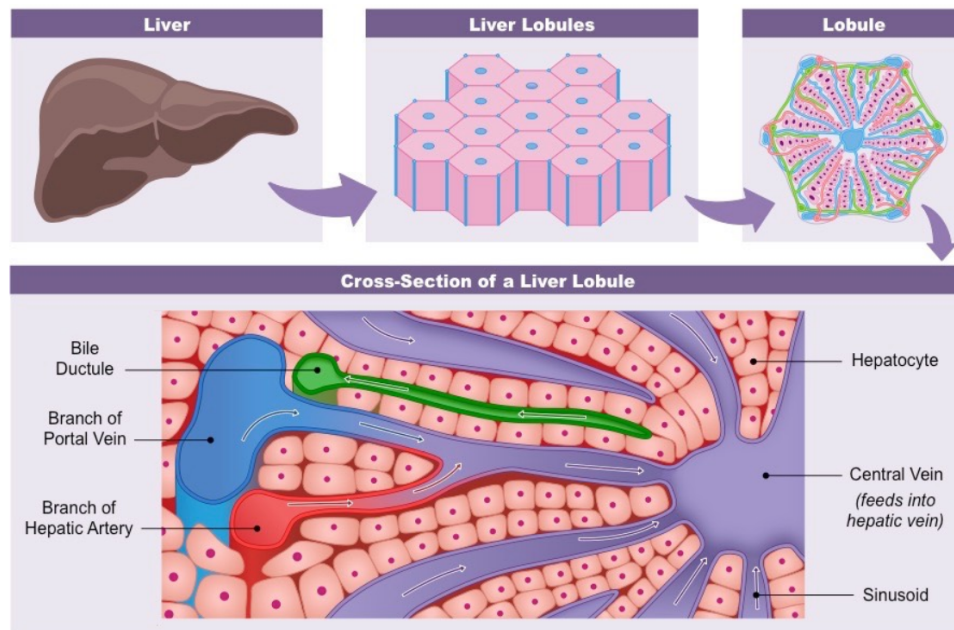
Figure 3.: Liver composition [15]

Hepatocytes are the most abundant type of liver cell and are responsible for the majority of the liver's functions [25]. They filter the blood and remove toxins, waste products, and other substances that are harmful to the body [26]. They also produce bile, which is a yellowish-green fluid that helps to digest fats and absorb fat-soluble vitamins. Bile is secreted into small bile ducts within the liver and is then carried to the gallbladder for storage.

Hepatocytes are in contact with blood via sinusoids, which are small, thin-walled blood vessels that are found within the liver. They are lined with fenestrated endothelial cells, which have small openings or pores on their surface. These openings allow small molecules, such as oxygen and nutrients, to pass through the endothelial cells and into the liver tissue, while larger molecules, such as cells and proteins, are retained within the bloodstream [11][52]. Figure 4 shows the sinusoid overview with a variety of different liver cell types.
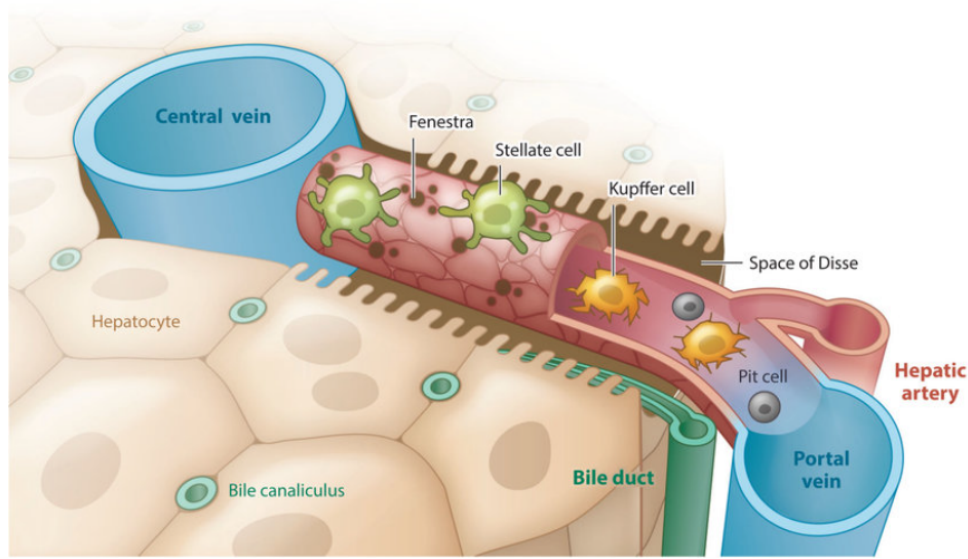
Figure 4.: Liver sinusoid [18]

1.2.3. Key physiological parameters of the liver

A few key parameters influence the physiology and functioning of the liver as shown in figure 5. These will be elaborated on in the following subsections.
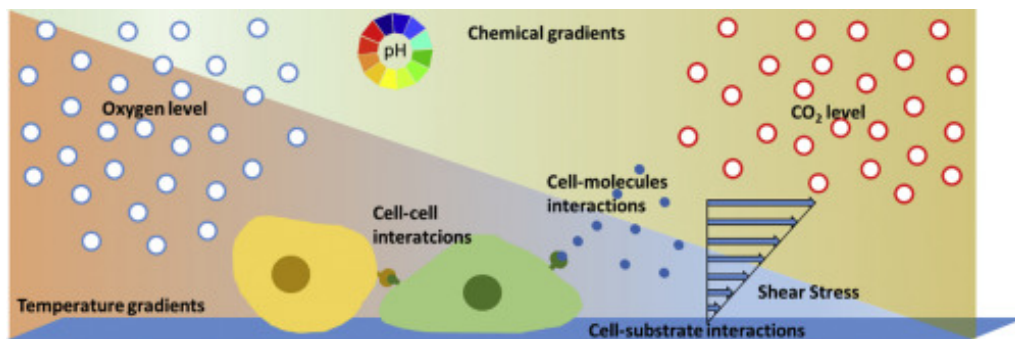
Figure 5.: Key parameters in the liver micro-environment [14]

Oxygen

Like all cells in the human body, liver cells use oxygen in cellular respiration to produce energy. During cellular respiration, glucose, and oxygen are converted into energy in the form of adenosine triphosphate (ATP), as well as carbon dioxide and water as waste products [39]. This process occurs in the mitochondria of the liver cell and is known as oxidative phosphorylation. The energy produced is used by the liver cell to carry out various functions such as metabolism, synthesis, and detoxification. The total process of cellular respiration is shown in figure 6.
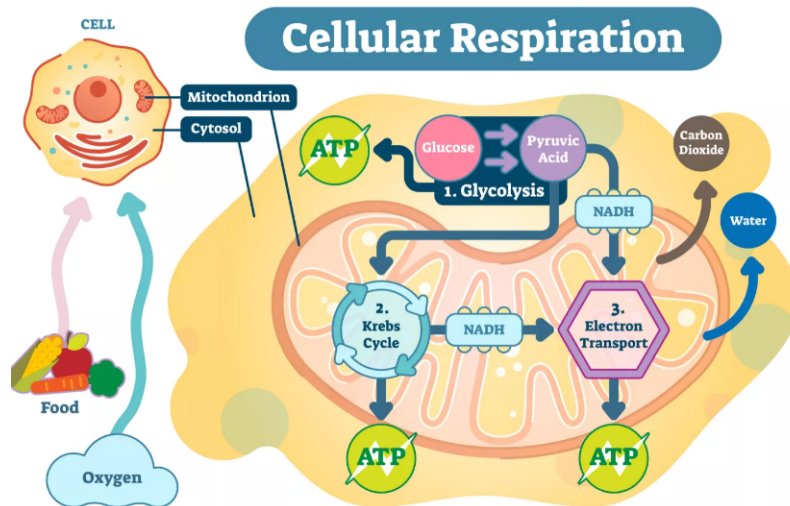
Figure 6.: Cellular respiration [39]

Within the hepatic sinusoid, there exists a gradient in the partial pressure of dissolved oxygen. Specifically, at the point of entry where blood flows in from the hepatic artery and portal vein, the partial pressure of oxygen measures approximately 60-65 mmHg (millimeters of Mercury), whereas, at the point of exit where blood flows out through the hepatic vein, the partial pressure of oxygen is reduced to 30-35 mmHg [27]. The concentration of dissolved oxygen in a liquid, such as blood or water, is typically measured in milligrams per liter (mg/L) or parts per million (ppm). The conversion between dissolved oxygen level and concentration depends on various factors, including temperature, pressure, and salinity, among others. In the case of a dissolved oxygen level in mmHg, this is equivalent to the partial pressure of oxygen in the liquid, which can be converted to a concentration of dissolved oxygen using the Henry's Law equation. At standard body temperature and pressure, a dissolved oxygen level of 65 mmHg translates to a dissolved oxygen concentration of approximately 8.7 mg/L, whereas a dissolved oxygen level of 30 mmHg corresponds to a concentration of roughly 4.0 mg/L [53].
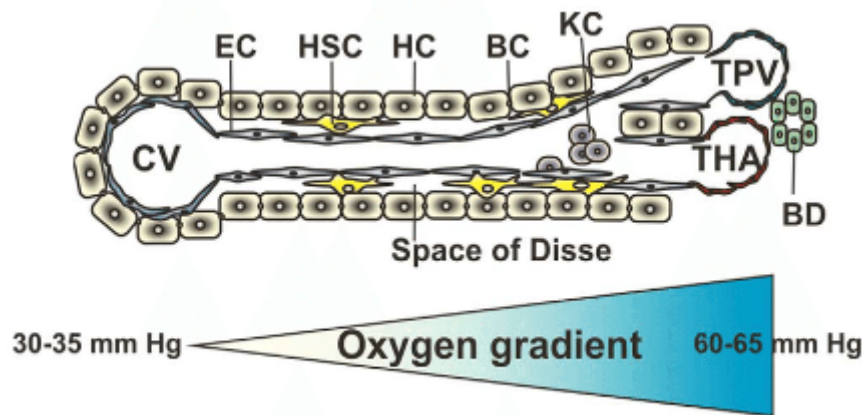
Figure 7.: Oxygen gradient throughout the liver lobule [27]

Too little or too much oxygen supply can have significant effects on liver cell physiology. When the liver cells have too little oxygen, also known as hypoxia, they activate a series of responses to adapt to the low-oxygen environment. These responses include the activation of signaling pathways that regulate the expression of genes involved in the cellular adaptation to hypoxia, such as the hypoxia-inducible factor (HIF) transcription factor. However, chronic hypoxia can lead to cellular damage and impaired liver function, ultimately leading to severe liver diseases [27][23].

On the other hand, liver cells supplied with too high concentrations of dissolved oxygen, also known as hyperoxia, can lead to the production of reactive oxygen species (ROS), which can damage cellular components such as proteins, lipids, and deoxyribonucleic acid (DNA). This damage can cause inflammation, leading to the development of liver diseases such as non-alcoholic fatty liver disease (NAFLD) and non-alcoholic steatohepatitis (NASH) [23].

In summary, it is essential to maintain an appropriate balance of oxygen supply to the liver cells to ensure optimal liver function and prevent the development of liver diseases.

Flow
The flow of blood through the liver sinusoids is unique because of its low velocity and intermittent nature [28]. The slow flow of blood through the liver allows for more prolonged contact between the blood and the hepatocytes, enabling the liver to carry out its many functions efficiently [52].

The liver's unique flow type also plays a critical role in the regulation of blood pressure and blood volume in the body. The liver can store and release blood as needed, and the slow flow of blood through the liver allows for precise regulation of blood pressure and blood volume [19].

Temperature
The optimal temperature in the human liver is around 37 °C. The liver is a highly

metabolic organ that performs many essential functions, including the synthesis of proteins, detoxification of harmful substances, and the regulation of glucose levels in the blood. These functions require a specific temperature range to operate optimally.

If the temperature in the liver becomes too high (hyperthermia) or too low (hypothermia), it can have significant effects on liver function. High temperatures can cause cellular damage and impair liver function, while low temperatures can slow down metabolic processes and reduce the liver's ability to carry out its many functions [49][46].

Therefore, maintaining a consistent and optimal temperature is crucial for optimal liver function.

Carbon dioxide
Carbon dioxide (CO_2) is an important component of the bicarbonate (HCO_3^-) buffer system, which is responsible for maintaining the pH value in the liver microenvironment. The buffer system helps to prevent rapid changes in the pH that could be harmful to cells and bodily functions. It consists of a weak acid, carbonic acid H_2CO_3, and its conjugate base, bicarbonate ion HCO_3^-, which are present in the blood and other bodily fluids [37]. The enzyme carbonic anhydrase (CA), found in among others red blood cells [13], facilitates the conversion of CO_2 and water (H_2O) into H_2CO_3, and is involved in the reverse reaction where H_2CO_3 is converted back into CO_2 and H_2O. The total bicarbonate buffer system working inside the liver microenvironment is shown in figure 8 and the total bicarbonate buffer system equation is shown in equation 1.1.
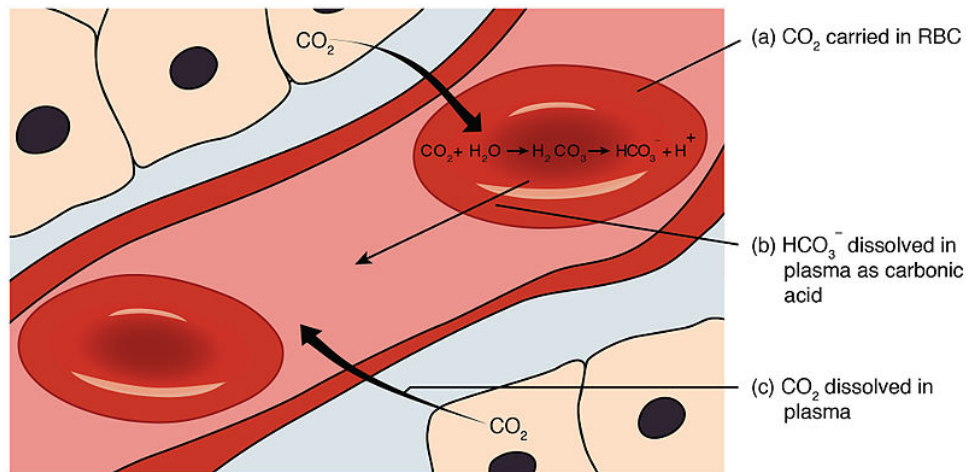
Figure 8.: Bicarbonate buffer system inside the liver microenvironment [4]

$$CO_2 + H_2O \rightleftharpoons H_2CO_3 \rightleftharpoons HCO_3^- + H^+ \tag{1.1}$$

Proper regulation of dissolved CO_2 levels is critical for maintaining acid-base balance and preventing the development of acidosis or alkalosis, which can have severe consequences for overall health [7].

1.3. Dissolved gases control unit

In an LoC, oxygen can be absorbed from the medium that perfuses the cells by diffusion [24][8][23]. To ensure liver functioning, there should always be sufficient oxygen available for uptake. This uptake rate depends on a lot of factors like contact area, the number of cells, flow rate, and oxygen availability [8]. Since liver cells require a specific oxygen partial pressure as stated in Section 1.2.3, oxygen must be controlled precisely. Oxygen can be supplied by either an incubator or an external oxygen supply for instance a canister or from ambient air. One alternative approach is to commence with a DO concentration that is completely saturated and subsequently decrease the concentration until the desired level is achieved. To reduce the concentration of dissolved oxygen, gas sparging adds for instance nitrogen gas into the solution through bubbling. Van Reeuwijk et al. (2021) developed a gas exchanger that utilizes gas-permeable silicon tubing and adjustable levels of nitrogen gas to decrease the DO concentration [51]. Figure 9 shows the gas exchanger box. Another solution is the use of oxygen scavenging, which involves adding a chemical agent that reacts with oxygen and removes it from the solution [34]. Unfortunately, residual oxygen scavengers may remain in the culture medium, which could impact the experiment results. The amount of oxygen that can dissolve in water or other aquatic liquids is inversely proportional to the temperature [41][5]. This relationship can be observed in figure 10. It is crucial to consider this relationship when setting the dissolved oxygen concentration, as an over-saturation of dissolved oxygen can lead to bubble formation, which must be avoided at all costs [32]. The concentration of DO in the culture medium cannot be compared directly to that in human blood supplied to liver cells since the mechanisms for oxygen uptake and delivery differ. In the human body, oxygen is carried by the circulatory system and binds to hemoglobin in red blood cells, as stated in Section 1.2.3. In contrast, in the culture medium, oxygen is dissolved and diffuses across cell membranes to reach the cells. Therefore, the concentration of DO needed in the culture medium is not identical to the liver physiological value stated in Section 1.2.3. In microfluidic experiments with liver cells, the concentration of DO for good results is often stated in mmHg, with normal organs ranging between 30-60 mmHg or 4% to 7.5% oxygen in the total gas composition. although it depends on cell type, culture conditions, and other factors[36].
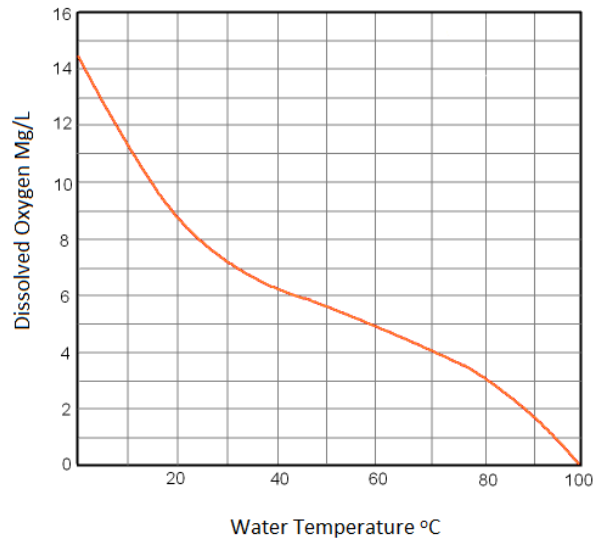
Figure 10.: Oxygen solubility in water [5]

15 mm
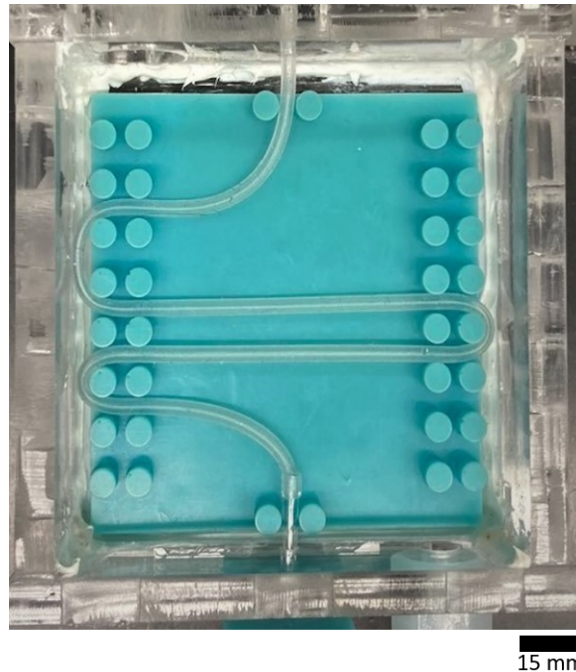
Figure 9.: Gas exchanger box by Van Reeuwijk et al. (2021) [51]

There are several options available to accurately measure the concentration of DO, including DO probes or readout components. These options differ primarily in their principles of operation, such as optical, polarographic, and electrochemical methods, as well as their price, accuracy, ease of calibration, and invasiveness [2][30][43][42].

- Optical DO probes measure DO by detecting changes in the fluorescence of an oxygen-sensitive luminophore in response to changes in oxygen concentration.

These types of probes are non-invasive and do not require calibration, making them relatively easy to use.

- Polarographic DO probes, on the other hand, use a membrane-covered electrode to measure oxygen concentration. These types of probes are more invasive and require regular calibration, but they offer high accuracy and stability.

- Electrochemical DO probes use a thin, gas-permeable membrane to separate the sensor from the sample and measure oxygen concentration by measuring the current generated by a redox reaction. These types of probes are also relatively invasive and require calibration, but they are often more affordable than polarographic probes.

- Invasive dipping probes are probably the most common type of DO probe and are typically used in benchtop applications. They work by physically dipping a sensor into the sample to measure oxygen concentration. These types of probes are relatively inexpensive and accurate, but require frequent calibration and can be prone to contamination.

- Flow-through sensors are similar to dipping probes but are designed to be integrated into a flow system. They work by passing the sample over a sensor that measures oxygen concentration and are often used in industrial applications. These types of probes are highly accurate but can be expensive and require careful calibration. Figure 12 illustrates a flow-through setup.

- Non-invasive sensor spots are a non-invasive method for measuring DO in a culture medium. These sensors work by using a fluorescent dye that is sensitive to oxygen levels. There are two main types of sensor spots: those that measure by dynamic luminescence quenching and those that measure by the difference in fluorescence. The sensor spot is placed on the outside of a transparent vessel, such as a culture flask. The sensor spot measures changes in luminescence or fluorescence(depending on the used technique) in response to changes in oxygen concentration and is non-invasive and easy to use. However, these types of sensors may not be as accurate as invasive probes and require careful calibration. Figure 11 shows a sensor spot readout system.

To be able to perform research regarding oxygen consumption, a chip material with low permeability to oxygen should be chosen. This way, only oxygen molecules that entered the chip through the perfusion medium can be consumed, resulting in useful results. The choice of microfluidic chip will be the Micronit resealable flow cell because it consists of borosilicate glass slides with a very low oxygen permeability [48].

Maintaining proper CO_2 levels is crucial for the bicarbonate buffer system present in the culture medium, which helps to maintain a pH similar to that in the liver. CO_2 is needed to keep this buffer system working properly. Hence, a CO_2-supplying incubator or an external CO_2 supply into the culture medium can be used to regulate CO_2 levels. Since one of the goals of this project is to design an incubator-free platform,

11
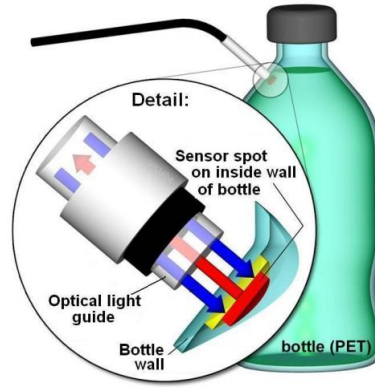
Figure 11.: Sensor spot setup [17]
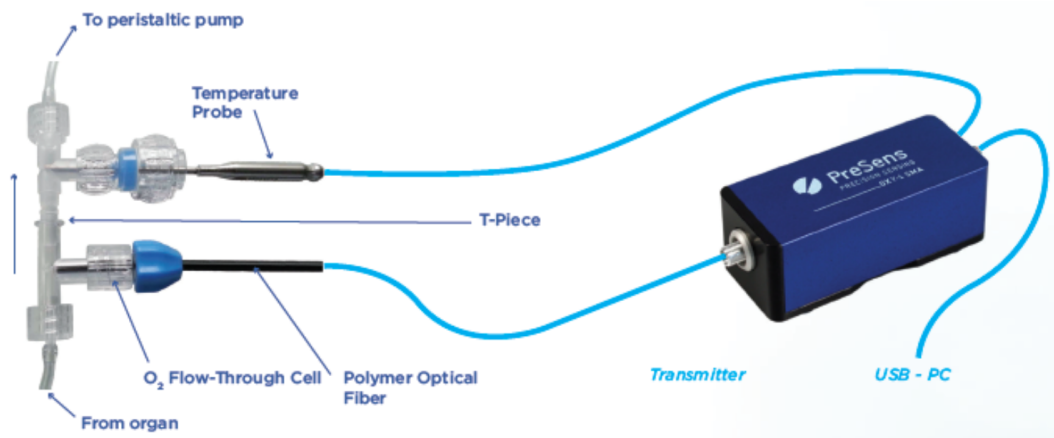
Figure 12.: Flow-through sensor setup [3]

an external CO_2 supply will be chosen. A pH probe can be used to ensure optimal pH and therefore functioning of the buffer system inside the culture medium. Additionally, a visual inspection of the color of the culture medium can be done, if a pH indicator dye is included in the medium. as it will change color when the pH is too low or too high. Phenol red is a commonly used pH indicator dye that is added to many types of cell culture media, including Williams E medium. It turns yellow at acidic pH levels (below 6.8) and pink at alkaline pH levels (above 8.2), making it easy to visually monitor the pH of the medium. This can help ensure that the medium remains at the optimal pH range for cell growth and functioning [31].

The culture medium used in the experiment is not completely air-tight when stored, and therefore, small concentrations of dissolved gases from the ambient air may be present. It is important to take this into account as these concentrations may vary between bottles and different volumes of the medium. Figure 13 displays a bottle containing culture medium and showcases the issue of varying air volumes above the medium and bottle materials, resulting in possible differences in the concentrations of dissolved gases between different bottles.

Figure 13.: A bottle containing Williams E medium [6]

The culture medium will be perfused from the reservoir to the microfluidic chip through the tubing. To prevent changes in the set concentration of DO, the tubing should have an extremely low gas permeability. The tubing should also be highly inert to be able to be used for biological experiments. Temperatures between 0-40 degrees Celcius should not be a problem for the tubing as well. Common tubing in microfluidic instrumentation setups include polyether ether ketone (PEEK), polytetrafluoroethylene (PFTE) Teflon, Tygon, fluorinated ethylene propylene (FEP), ethylene tetrafluoroethylene (EFTE), and polypropylene (PP) tubing [47]. They mostly differ in chemical and pressure resistance and should be chosen based on the specific needs of this project.

1.4. Flow control unit

Accurately meeting the physiological flow requirement of liver cells is crucial, and the flow control unit plays a key role in achieving this.

1.4.1. Flow system

For this project, the end user will use liver cells. The same Micronit chip as in research by El Hassan et al. (2023) will be used. The resealable Organ-on-Chip by Micronit consists of only a glass slide containing holes for perfusion and an elastomer gasket. Cells can be easily seeded on a regular glass slide and afterward, the two parts can be clamped together. Because the chip is made of glass, Micronit also developed a clamping mechanism for their Organ-on-Chip, to ensure proper clamping and prevent leakage of perfusion media or entering of air. The chip holder including the chip, before closing, is shown in figure 14.

Figure 14.: Micronit chip holder

1.4.2. Flow rate

Flow is necessary to mimic liver physiology on a microfluidic platform, but it also introduces shear stresses that can harm cells if they exceed a safe limit. For liver cells, the threshold is typically set below 0.5 Pa to prevent cell detachment or death [18]. Shear stresses on the cells can be reduced by using microwells, microfabricated groves, or specially designed niches [40][10][29]. An alternative approach is to utilize an oxygen carrier such as emulsified fluorocarbon, which can supply sufficient oxygen with a lower flow rate and consequently reduce the exposure to maximum shear stress [18].

The microfluidic chip used, will determine the dimensions of the flow channels and pressure drop and therefore play an important role in the flow rate through the channels. The chip dimensions of the chosen Micronit chip are shown in Appendix **??**.

In the context of this project, maintaining laminar flow is critical to ensure that cells are supplied with a uniform distribution of dissolved oxygen and nutrients. This requires careful consideration of the chip dimensions and flow rate to keep the flow in the laminar regime, as turbulence can disrupt the uniform distribution. By keeping the flow laminar, below 2100 [44], cells can be cultured in a controlled environment, allowing for accurate measurement and analysis of their behavior under various experimental conditions. Some values like the flow rate of 35 μL/min. are chosen according to earlier research by Van Reeuwijk et al. (2021) [51], who used the same Micronit chip.

From equation 1.2 the Reynolds number can be calculated.

The formula for the Reynolds number is:

$$\text{Re} = \frac{\rho \, U \, \zeta}{\mu} \tag{1.2}$$

In the equation, ρ is the density (kg/m^3), U is the flow velocity (m/s), ζ is the characteristic length (m), and μ the dynamic viscosity (Pa·s)

1.5. Diffusion theory

For oxygen mass transfer, it is assumed that the solute oxygen is sufficiently dilute such that it does not affect the motion of the solvent, for instance, the cell medium. The mass transfer of dissolved oxygen, through the cell medium or oxygen-permeable membrane, is the transport of a dilute species described by the convection-diffusion equation in equation 1.3.

$$\frac{\partial c}{\partial t} + \mathbf{u} \cdot \nabla c = D \nabla^2 c + R \tag{1.3}$$

In the equation, c is the concentration (mol/m^3), t is time (s), $\mathbf{u}$ is the velocity field (m/s), D is the diffusion constant (m^2/s), and R is the sink term (mol/m^3/s). The term $\mathbf{u} \cdot \nabla c$ relates to convection, the term $D \nabla^2 c$ relates to diffusion, and the term R relates to a reaction, for instance, cellular oxygen consumption.

For transient diffusion over time (excluding convection), Fick's second law of diffusion for the concentration c in one dimension x is stated in Equation 1.4. Fick's second law can be solved with the complementary error function in Equation 1.5. In this equation, c_s is the saturation concentration (mol/m^3), c_0 is the initial concentration (mol/m^3), x is the diffusion length (m), D is the diffusion constant (m^2/s), and t is the time (s).

$$\frac{\partial c}{\partial t} = D \frac{\partial^2 c}{\partial x^2} \tag{1.4}$$

$$c(x,t) = c_0 + (c_s - c_0) \cdot \text{erfc} \left(\frac{x}{2\sqrt{Dt}} \right) \tag{1.5}$$

1.6. Fs laser fabrication

In this project, a microfluidic gas exchanger will be designed and fabricated to enable the regulation of dissolved oxygen into a culture medium. Glass could be a potential material choice. Several manufacturing possibilities are possible for making channels on a glass substrate. Glass is a relatively brittle material that cracks or burrs easily when exerting too much power due to its thermal properties. Therefore, precise and steady machining is needed. For this purpose, the Lasea Femtosecond Fs laser system has been chosen for laser ablation.

1.6.1. Introduction to Fs laser ablation

Laser ablation is a technique that utilizes a highly focused laser beam to remove material from a solid surface. In the case of glass, this technique offers advantages over traditional machining methods because it minimizes thermal damage to the material. The Lasea fs laser emits ultrashort pulses with a duration in the domain of 10^{-15} seconds. These pulses are extremely brief, allowing for precise material removal without excessively heating the glass, which could otherwise cause it to break or crack.

1.6.2. Fs laser ablation theory

A Fs laser emits a pulse by opening and closing its shutter. The energy per unit area incident to the substrate is called the fluence, F. In this equation, E is the laser energy and A is the area of the laser spot. The laser spot size is 0.025 mm.

$$F = \frac{E}{A} \tag{1.6}$$

Figure 15 shows the difference between a long and short pulse laser. It is visible that a longer laser pulse will result in a loss of quality of the laser result. Femtosecond laser ablation is therefore more promising for good quality demands.
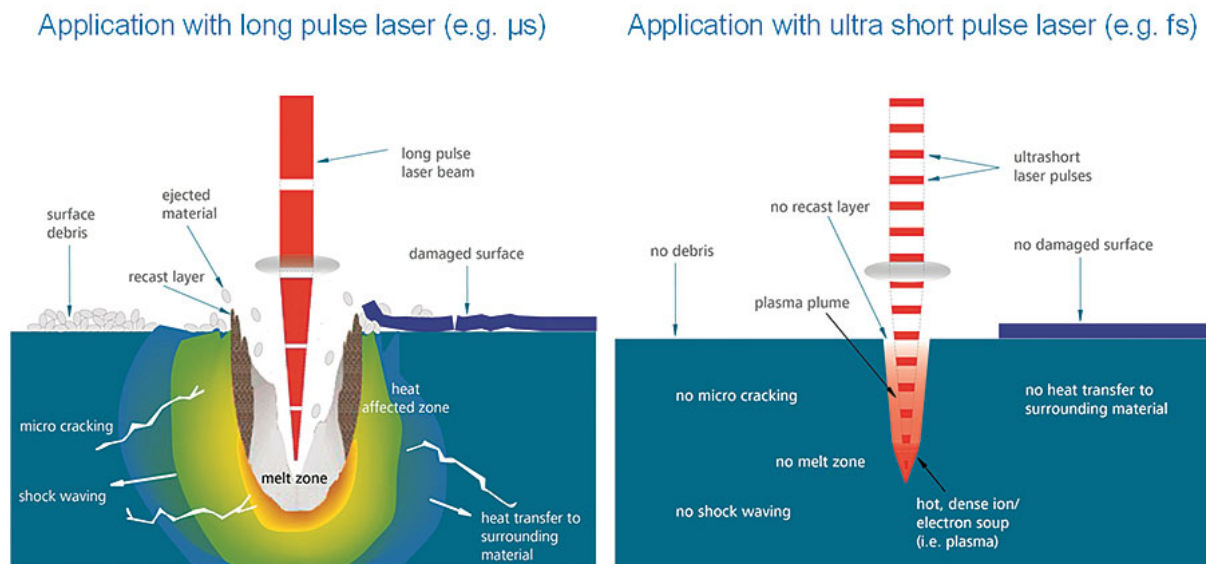

Figure 15.: Difference between long and short pulse laser ablation

1.6.3. Laser system components

The Lasea Fs laser system is comprised of several important components, each playing a crucial role in the laser ablation process. These components include:

- **Aerotech stage:** Provides precise movement control of the stage bed, ensuring accurate positioning for laser ablation.

- **Lens:** Focuses the laser beam to a small spot size on the surface of the glass, enhancing precision and efficiency.

- **Mirrors:** Direct and reflect the laser beam, guiding it along the desired path on the glass substrate.

- **Laser source:** Generates the ultrashort pulses of laser light used for ablation.

- **Camera:** Monitors the ablation process, allowing for real-time feedback and adjustment as needed.

- **Beam Expander:** Adjusts the diameter of the laser beam to suit the application, optimizing processing parameters.

- **Beam Splitter:** Divides the laser beam into multiple paths for simultaneous processing or monitoring.

- **Beam Shutter:** Controls the timing and duration of laser exposure to the workpiece, ensuring precise material removal.

- **Beam Profiler:** Measures the spatial intensity distribution of the laser beam, ensuring uniformity and consistency of processing.

- **Cooling System:** Maintains stable operating temperatures for the laser source and other components, preventing overheating and ensuring long-term reliability.

1.6.4. Important laser parameters

A range of parameters must be tuned to the specific material and goal in laser ablation processes. Initially, a systematical set of parameters was attempted, followed by an analysis of the results. Among these parameters, the most critical ones include:

- **Power % of maximum output power (15 Watts):** This parameter determines the intensity of the laser beam.

- **Speed (in mm/s):** Denotes the moving speed of the stage, influencing the energy delivered to a certain location on the material.

- **Repetitions:** Quantifies the number of times the laser repeats the same pattern.

- **Hatching pitch (in mm):** Describes the distance between two adjacent hatching lines in mm. Hatching involves removing a surface by employing a specific pattern of multiple lines.

- **Outlines and outline pitch (in mm)**: Denotes the number of outlines, lines added to the initial shape, and the distance between two of these lines. In some specific shapes, this can give the same effect as hatching.

- **Layers and layer pitch (in mm)**: Describes the number of layers with a certain offset denoted by the layer pitch.

Fabrication of a glass microfluidic gas exchanger using a femtosecond laser

Jelle Smit[a]

[a]*Delft University of Technology, Department of Precision and Microsystem Engineering*

Abstract

Organ-on-chip (OoC) technology has transformed biomedical research by providing a platform to simulate physiological conditions for drug development and disease modeling. Incubator-free OoC systems offer notable advantages over traditional approaches, including enhanced adaptability and impermeability to gases. Nevertheless, achieving precise oxygen regulation remains a challenge in such systems. This thesis investigates the application of femtosecond (Fs) laser ablation to fabricate a glass microfluidic gas exchange system for accurate oxygen regulation in incubator-free OoCs. Through successful engraving of fluidic channels and integration of an off-the-shelf optical oxygen sensor, this study highlights the efficacy of Fs laser technology in the rapid prototyping of intricate glass microfluidic devices. Despite encountering challenges such as dimensional losses and debris clogging, the study presents a functional gas exchanger prototype. Future research directions include optimization efforts, addressing issues like gas permeation through connectors, and testing under physiological conditions to further advance OoC technology.

Keywords: Microfluidics, Gas exchanger, Miniaturization, Optical oxygen sensing, Fs laser fabrication, Sensor integration, Organ-on-Chip

1. Introduction

In the past two decades, Organ-on-Chip (OoC) technology has significantly advanced biomedical research, particularly in drug development and disease modeling (Driver et al. (2023)), by providing a controlled environment to mimic physiological conditions without the need for human or animal testing Lin, K-C et al. (2022). However, precise oxygen regulation remains an essential yet challenging aspect (Place et al. (2017)). While adept at maintaining temperature and gas composition, traditional incubator-based systems often lack or face challenges in essential fluid flow and real-time imaging Zhang, Yu Shrike et al. (2017). Furthermore, refreshing culture medium within incubators often results in abrupt shifts in temperature, gas concentrations, and cessation of nutrient supply, potentially disrupting cellular environments (Fujiwara et al. (2007)). Incubator-free OoCs hold promise due to their easy adaptability to specific cellular needs and when utilizing glass, impermeability to gases. Yet, achieving precise oxygen regulation in incubator-free OoCs presents a significant challenge. Therefore, the need for an oxygen regulation system, or a gas exchanger as depicted in Figure 1, arises to address this issue. Diffusion is the physical process involved, where a gradient in oxygen concentration between the gas and liquid layers determines the direction of oxygen transport (indicated by the green arrows, which can point toward either direction, but only one direction at a time).To fabricate a miniaturized, glass gas exchanger, femtosecond (Fs) laser engraving offers a novel approach to creating glass microfluidic devices with precision and versatility, eliminating the need for masks and chemical developers, unlike other methods such as photolithography and wet etching Hamed, Hazem et al. (2023).

This thesis leverages Fs laser technology to rapidly prototype a microfluidic gas exchange system, integrated with an off-the-shelf optical oxygen sensor for real-time monitoring. The goal is to demonstrate the efficacy of Fs laser engraving in fabricating gas exchange systems capable of addressing the critical challenge of oxygen regulation in incubator-free OoC platforms.

The central research question driving this study is: *How can Fs laser technology be utilized to rapidly prototype a microfluidic gas exchanger system for accurate oxygen regulation in incubator-free OoCs?*

By elucidating the fabrication process and highlighting the advantages of Fs laser engraving, this thesis aims to contribute to OoC technology, fostering physiologically relevant in vitro models for biomedical research toward the ultimate goal of Human-on-Chip.

2. Materials and Methods

2.1. Materials

Several materials are used for this project. A detailed list including brands and serial numbers can be found in Appendix C

2.2. Methods

Figure 2 provides an overview of the entire system. A microfluidic gas exchanger comprises a liquid channel responsible for transporting the culture medium, which contains vital nutrients for specific organ cells. To manipulate the oxygen concentration within this flow, another pathway is dedicated to gas flow. These two streams are separated by a membrane, which
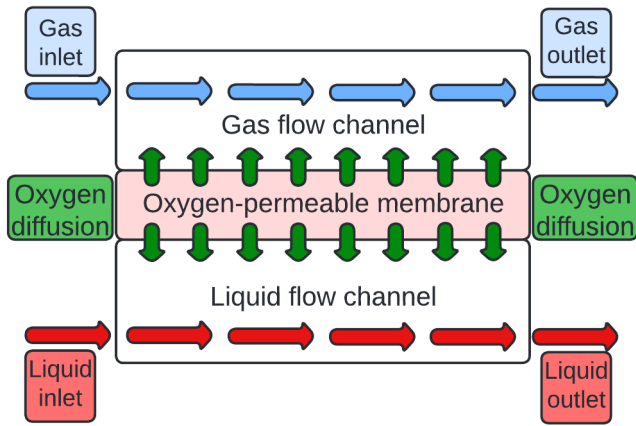
Figure 1: Schematic representation of a gas exchanger with oxygen diffusion, the direction of the green arrows depends on the oxygen concentration gradient between the gas and liquid channels

Figure 2: System overview

selectively allows gases to diffuse through. A gas concentration gradient across this membrane is the driving force for regulating and controlling the concentration levels. The liquid is initially perfused from the syringe pump through the gas exchanger towards the Micronit chip, where the cells can be housed. At the same time, the gas flow begins from the Bronkhorst OEM (Original Equipment Manufacturer) gas supply system, moves through the gas flow reducer into the gas exchanger, and then into the surrounding ambient air. Optical measurements within the microfluidic device enable monitoring of oxygen concentration inside the cell chamber.

2.2.1. Gas Exchanger Subsystem

Central to the overall system is the microfluidic gas exchanger subsystem, representing a pivotal and innovative component. This subsystem is designed to accommodate ports for both liquid and gas inflow and outflow, facilitating the efficient regulation of oxygen concentration within the liquid flow.

Gas Exchanger Design

The design of the microfluidic gas exchanger is grounded in a compact and intricate glass-polydimethylsiloxane (PDMS)-glass sandwich structure, as shown in Figure 3 and Figure 4. This configuration plays a critical role in orchestrating the controlled exchange of gases within the system while preventing undesired gas permeation, given the inherent gas impermeability of glass. Positioned between two glass layers, the PDMS layer functions as a selectively permeable membrane, facilitating the diffusion of gases into the liquid stream while impeding the passage of larger molecules, solids, nutrients, or culture medium. The PDMS membrane layer is sourced from a readily available PDMS sheet.

A standard borosilicate glass microscope slide is selected for its convenience and widespread availability. To mitigate the risk of trapping air or inducing turbulent flow, both the liquid and gas channels feature a filleted perimeter. The gas channel fully overlaps with the liquid channel to optimize diffusion, with slight extensions to 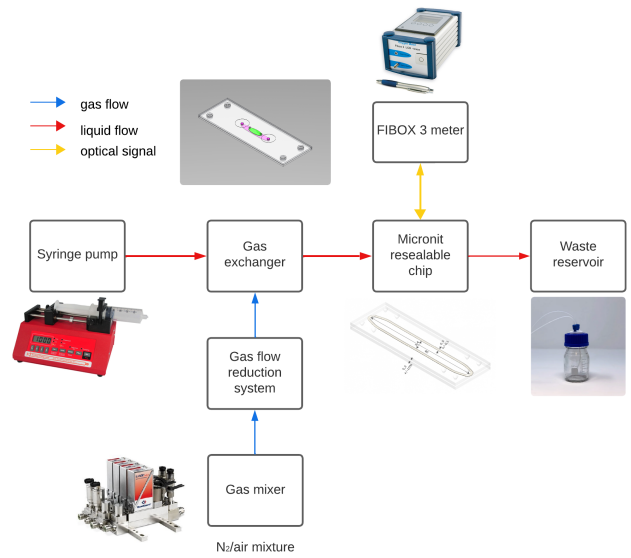ensure unobstructed port access. This top-connect gas exchanger sandwich structure is designed for easy placement on a benchtop, potentially atop a heating plate. Additionally, blind holes are incorporated into the design to aid in accurate alignment of the fluidic ports above the channel apertures.

A custom alignment tool was created through 3D printing to enhance the alignment of the layers in the sandwich structure. This tool was designed to maximize the contact surface area, promoting optimal bonding between layers. Additionally, precise alignment facilitated unobstructed fluid pathways from the ports into the sandwich structure. The alignment tool was printed using PETG (polyethylene terephthalate glycol) filament on the Prusa i3 MK3S+ 3D printer using generic PETG and 15% infill settings. PETG is chosen for its ease of printing, robust mechanical properties, and chemical resistance, which is essential for sterilization before device assembly. The alignment tool comprises a base with four pins spaced at the same intervals as the through holes in the device layers, as shown in Figure 6. These through holes are positioned near the edges of the device layers, allowing for gradual layer placement similar to a hinge, thereby minimizing bubble entrapment during bonding.

Gas exchanger modeling

Detailed SolidWorks models were crafted to enhance the comprehension of the gas exchanger's intricate geometry. Appendix F contains technical drawings with all critical dimensions for each gas exchanger layer and the 3D alignment tool. The liquid channel, with a depth of 300 μm, exhibits an almost oval shape, measuring 4 mm in width at its widest point, and spanning a length of 10 mm. Conversely, the gas channel, slightly more elongated, maintains a depth of 500μ m, also spanning 4 mm in width at its broadest part, and extending to a length of 25.3 mm. Figure 3 offers a visual depiction of the gas exchanger, with the PDMS membrane layer depicted in white for clarity. Figure 4

2

presents an exploded view, highlighting the distinct layers of the structure. Additionally, a sectional view in Figure 5 showcases the complete diffusional contact, with both channels separated by the PDMS membrane layer.
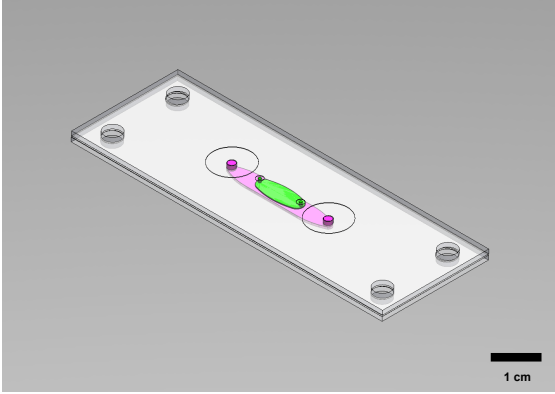

Figure 3: SolidWorks isometric image of the gas exchanger. The liquid body within the liquid channel is represented in green, while the gas body within the gas channel is illustrated in purple.
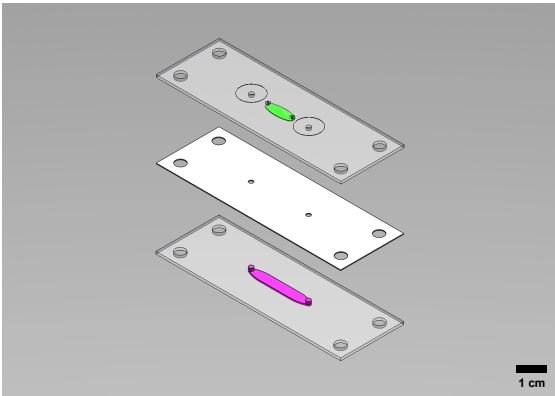

Figure 4: SolidWorks exploded view of the gas exchanger. The liquid body within the liquid channel is represented in green, while the gas body within the gas channel is illustrated in purple.

Diffusion modeling

A comprehensive dimensional analysis using COMSOL Multiphysics software was conducted to evaluate the gas exchanger model's performance, determined by the ability to reach all needed oxygen concentrations specific for each organ.

The model, constructed in three dimensions, uses a simplified rectangular representation of the gas exchanger's geometry and predicts the concentration profile within it. This simplified geometry is shown in Figure 7. In this figure, the top layer is the gas channel, the bottom layer is the liquid channel, and the membrane layer in between. Laminar flow physics is applied to the culture medium and gas domains, while transport of diluted species (TDS) physics is implemented across all domains. The liquid flow will be perfused through the entire system at a predetermined flow rate of 35 μL/min, as specified by van Reeuwijk, Matthijs (2021).

In the analysis, a limit case scenario is considered: the liquid and membrane start fully oxygen-saturated, and nitrogen
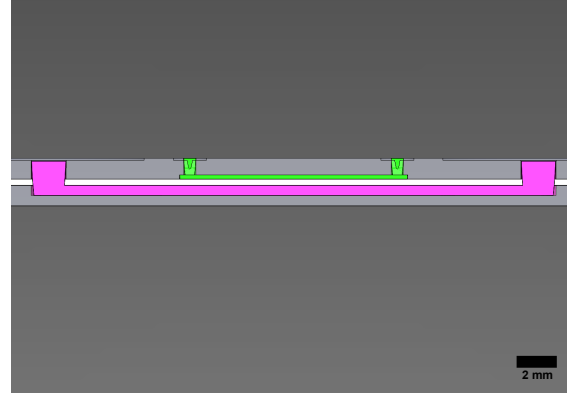

Figure 5: SolidWorks zoomed-in section view of the gas exchanger, with the section made through the center along the long side of the gas exchanger. The liquid body within the liquid channel is represented in green, while the gas body within the gas channel is illustrated in purple.
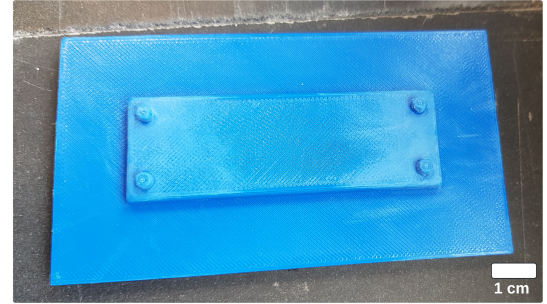

Figure 6: 3D printed alignment tool

is used to withdraw oxygen from the liquid through the membrane into the gas stream. Notably, the time required to transition from c_0=0 mol/m^3 to c_{max} of 0.20 mol/m^3 of oxygen molecules in the liquid is equivalent to the reverse step of reaching c_0=0 mol/m^3 starting with c_{max} in the liquid according to the convection-diffusion equation provided in the background section 1.5.

Key parameters investigated include gas and liquid flow rates, membrane thickness, channel dimensions, length of the gas exchanger, and temperature which can be found in Appendix G.

Insightful results from the COMSOL model reveal the transition of oxygen concentration at the culture medium outlet from an initial fully oxygen-saturated state to a lower limit value over time. Specifically, the oxygen concentration at the liquid outlet, with this geometry, has the lowest oxygen concentration of 12×10^{-6} mol/m^3 of oxygen molecules, which is equivalent to 0.047 mmHg. For practical purposes, this value will be considered as 0 mmHg. This concentration is significantly lower than the desired concentration required for different organ needs, which ranges from 0.0079 to 0.014 mol/m^3 (31 to 56 mmHg) McKeown, SR. (2014). Thus, it can be concluded that there is sufficient capacity to meet the oxygen demands of all organs.

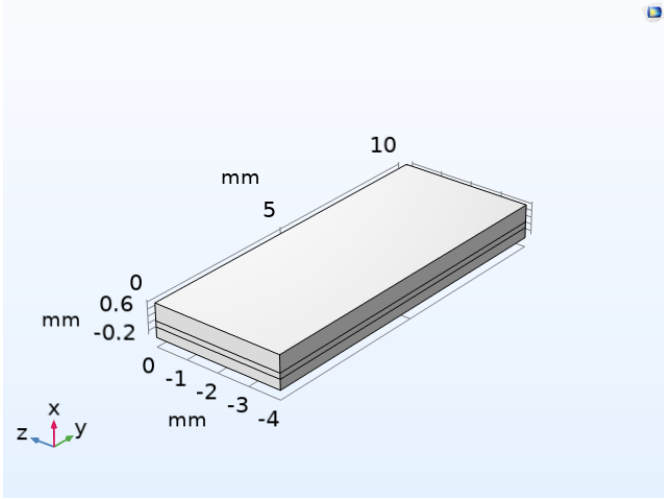Please note that this COMSOL model assumes rectangularly

3

Figure 7: COMSOL gas exchanger geometry, top layer: gas channel, middle layer: membrane layer, bottom layer: liquid channel
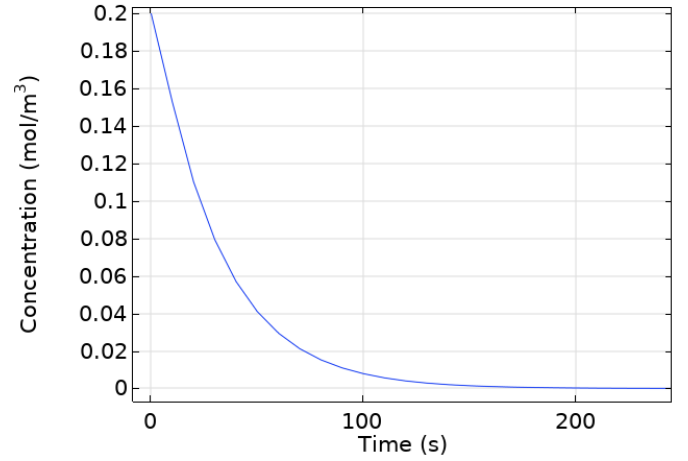

Figure 8: Concentration profile showing the average concentration at the liquid channel's exit over time.
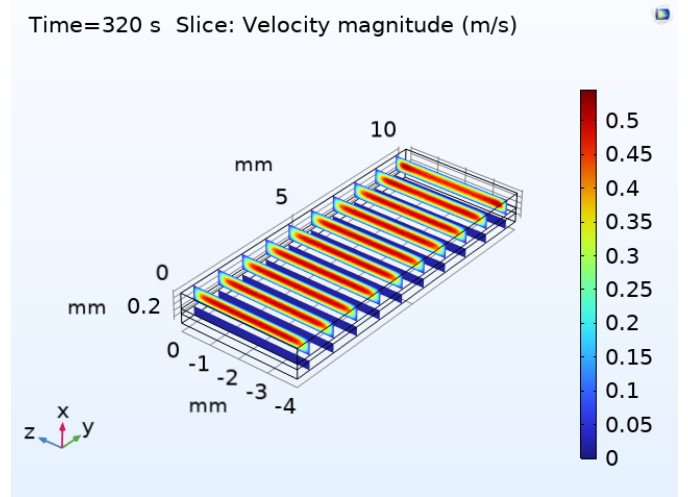

Figure 9: Velocity profile throughout the gas exchanger. The top section represents the gas channel, and the bottom rectangle represents the liquid channel. The heat map colors indicate fluid velocity.

shaped channels instead of the filleted, more ovally-shaped gas exchanger channels. The concentration setting time is approximately 80 seconds to reach within a 10% deviation from the set concentration (c=0.02), and 140 seconds to reach within a 1% deviation from the set value (c=0.002).

The concentration profile is shown in Figure 8. The x-axis represents time in seconds, while the y-axis represents concentration in mol/m^3. The concentration in this plot is the average value of the concentration at the liquid channel's exit, chosen to provide a fair result, as the concentration might vary throughout the liquid outlet.

Additionally, the velocity profile throughout the gas exchanger is depicted in Figure 9. The top section represents the gas channel, while the bottom rectangle represents the liquid channel. The different colors in the heat map denote the fluid velocity throughout the channels. The gas flows at a significantly higher velocity through the channel compared to the liquid. The highest flow velocity is observed at the center of the channel.

Deformation of PDMS membrane

This section provides a comprehensive overview of the modeling process for PDMS membrane deformation, a pivotal aspect in the design of this microfluidic gas exchanger since too large pressure differences across the membrane can result in blockages, tears in the PDMS layer and even leaks and cross-contamination.

Various factors influence membrane deformation, including material properties such as Young's Modulus (E) and geometric considerations like membrane width and thickness. Additionally, factors such as pressure differentials across the membrane play significant roles.

Simulation is carried out using COMSOL Multiphysics software, utilizing Solid Mechanics with plane strain physics. The model geometry adopts a straightforward beam deflection model, wherein the width signifies the actual liquid and gas channel width (4 mm), and thickness (170 μm) reflects the

membrane thickness. A 2D model is selected for computational simplicity, given that deflection in the z-direction remains independent of length due to fixed supports along the borders where no gas or liquid flows. PDMS is added to the simulation having Young's modulus (2.2 MPa) and Poisson ratio (0.499) (Gangwar, Sudhanshu et al. (2024)) (Dogru et al. (2018)). Boundary conditions are applied, with fixed supports to prevent deformation on vertical boundaries. In contrast, the top horizontal boundary receives a distributed load by pressure (ΔP) to reflect uniform absolute pressure in that direction.

It's important to note that the bonding between the PDMS membrane and substrate is assumed to be perfectly tight and strong, eliminating any potential influences on membrane deformation.

From the calculations detailed in Appendix D, it is determined that the expected pressure difference across the membrane is ΔP = 229 Pa. This calculation relies on the Hagen-

Poiseuille equation, as shown in Equation 1, where ΔP represents the pressure drop (in Pa), η denotes the dynamic viscosity (in Pa·s), L represents the characteristic length (in meters), Q signifies the fluid flow rate (in m^3/s), r denotes the channel radius (in meters), w the channel width (in meters), and t the channel height (in meters).

$$\Delta P_{\text{circ}} = \frac{8\eta LQ}{\pi r^4} \quad \text{for circular channel}$$
$$\Delta P_{\text{rect}} = \frac{12\eta LQ}{wt^3} \quad \text{for rectangular channel} \tag{1}$$

The displacement plot, shown in Figure 10a, reveals that with a pressure difference of 229 Pa, the membrane model exhibits the most deformation towards the gas channel side. This is further illustrated by the displacement versus pressure difference graph of the center point with the most overhang, depicted in Figure 10b. Therefore, with a maximum membrane deformation of $\delta = 100\ \mu m$, significantly below the gas channel height of 500 μm, it is disregarded.

(a) Membrane displacement plot under a pressure difference of 229 Pa

(b) Pressure difference vs. displacement of the membrane
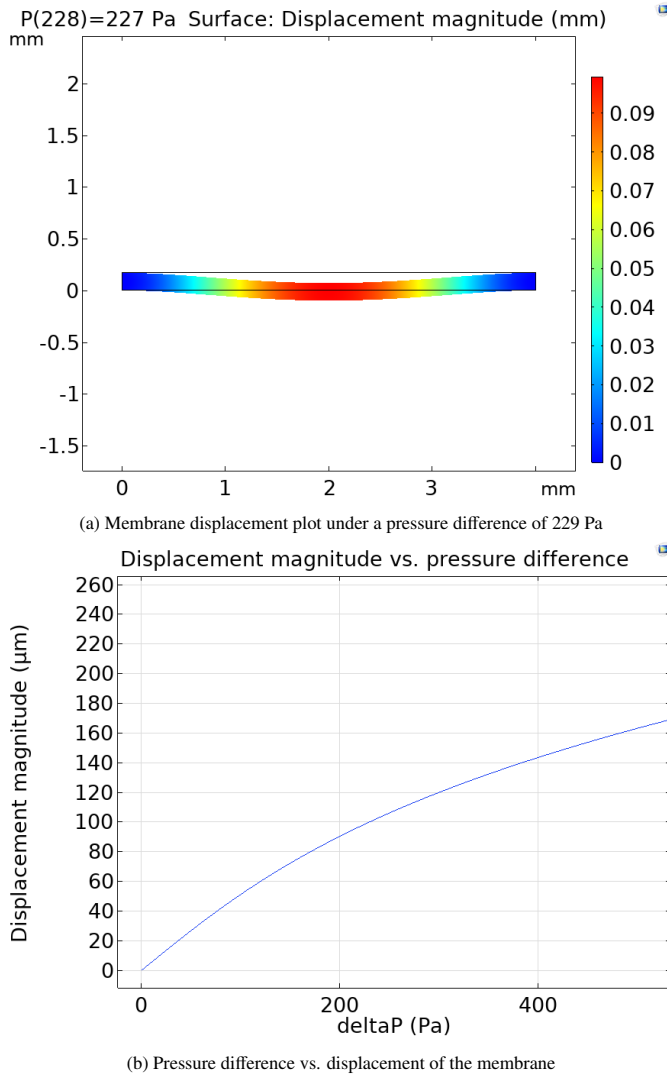
Figure 10: Membrane deformation analysis

2.2.2. Liquid flow system

The gas exchanger is part of the liquid flow system as shown in Figure 2. The other components are the syringe pump, gas-tight syringe, tubings, and connectors as well as the Micronit chip. Poly ether ether ketone (PEEK) connectors and tubing are chosen to minimize unwanted oxygen permeation through the connector material since PEEK has a relatively low diffusion coefficient of $D = 0.473 \times 10^{-12}\ m^2$/s (Monson, Loxie, Sung In Moon, and CW Extrand. (2013)). The inside part of a needle gauge number 32 (Nordson Precision Tips) is used to connect the tubing to the gas exchanger liquid ports, which are made by another piece of PEEK tubing. The procedure for separating the needle gauge inside from its cap is explained in Appendix H.1.

2.2.3. Gas flow system

As visible in Figure 2, the gas system starts with the Bronkhorst OEM gas supply system at Erasmus Medical Center, to provide a free-to-choose gas composition. The system consists of 4 independent GUI (Graphical User Interface)-controlled Mass Flow Controllers (MFCs), all connected to a gas supply tank of nitrogen, air, oxygen, and carbon dioxide. The Bronkhorst system is only operational at a minimum of 40 mL/min. for each gas flow. Appendix L provides the compositions of each gas required to achieve specific concentrations of oxygen and carbon dioxide as well as a picture of the Bronkhorst OEM gas supply system. For some gas mixtures, a total gas flow rate of 200 mL/min. satisfies, but for lower oxygen concentrations, the total gas flow should scale up two-fold to 400 mL/min. The gas flow rate exceeds the capacity of our compact gas exchanger, prompting the design of a simple gas flow reduction system. This setup diverts a significant portion of the gas mixture from the gas exchanger. The setup consists of a gas tube connected to a T-connector. Two outlet tubes extend—one to ambient air and the other to a manual control valve. Adjusting the valve reduces the gas flow rate to a level sustainable by the gas exchanger.

2.2.4. Oxygen sensing subsystem

In this project, small oxygen-sensitive sensor spots play a crucial role in measuring dissolved oxygen levels. Specifically, one sensor spot is strategically positioned before the intended location for cell placement, ensuring accurate measurement of the oxygen concentration at this pivotal point. While the focus of this project is on utilizing the first sensor spot, it's worth noting that other users have the option to integrate a second sensor spot behind the cells to monitor cellular oxygen uptake.

These sensor spots are seamlessly integrated into a commercial Micronit glass microfluidic chip in a zero dead-volume configuration. This integration process involves placing the sensor spots within blind holes fabricated into the glass slide. Subsequently, the sensor spots are securely fitted into the cavities using a force fit method. Once the sensor spots are firmly in place, the Micronit chip can be closed and operated following the manufacturer's instructions.

Figure 11 demonstrates the arrangement of the sensor spots on the Micronit glass slide, depicted by the pink circles. These
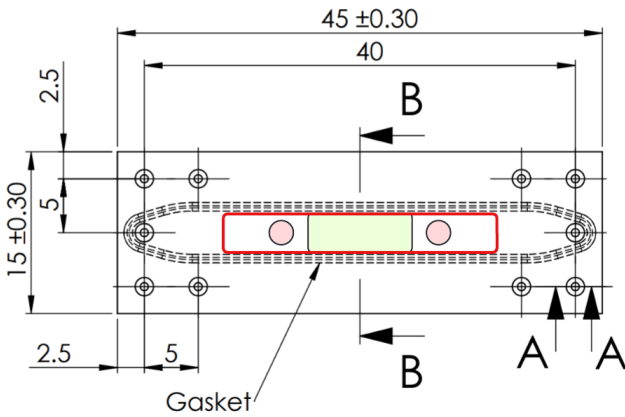
Figure 11: Micronit chip schematic, in yellow the cell placement area, pink the sensor spots, and in red the imaging window

Figure 13: Optimized laser fabrication parameters chart

spots are strategically positioned to enable probing from the top through the imaging window of the Micronit clamp, indicated by the red rectangle. The yellow area denotes the space available for cell placement. The Micronit chip located inside the Micronit Pro Holder clamping device is shown in Appendix B

2.2.5. Fabrication

In this section, we will discuss the fabrication steps for the gas exchanger and sensor spot integration hole. The fabrication process involves multiple parameters that influence the result of the Fs laser job, necessitating optimization to determine optimal settings. Figure 12 illustrates a schematic representation of common etching settings. The Fs laser utilized in this process is the Lasea LS-Lab (50 fs, 515 nm, 15 Watts). For detailed instructions on laser fabrication, please refer to Appendix B.1. Additionally, Appendix I presents a cause-effect (Ishikawa) diagram outlining the determinants that influence the quality of the laser result.
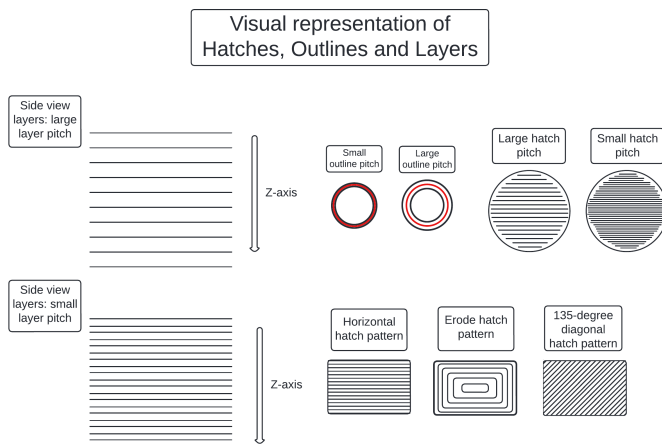
Optimizing laser fabrication parameters

Parametric sweeps are performed to optimize the combination of important parameters in laser ablation processes. In these sweeps, a parameter of choice is varied systematically, while keeping all other settings the same. For example, parameters such as stage moving speed can be varied to explore their effects on the ablation process. First to get a general idea and later for through hole cutting or engraving channels specifically. The varied parameters for each goal are visible in Figure 13. For further insights into the theory and meanings of the parameters, refer to the background section 1.6 of this report.

The speed at which the stage moves, and consequently, the energy applied to the surface, is anticipated to have a significant impact on quality. A high moving speed is likely to expedite certain portions of the trajectory, potentially resulting in shortcuts.

The outline pitch will determine the overlap between layers and therefore highly influence the etching depth, which needs to be of an extremely high aspect ratio to cut entirely through the glass slide.

The number of repetitions can be an interesting parameter to analyze how effective an increased amount of repetitions will be on the etch depth and quality.

For through holes, two approaches are compared. One uses hatching to remove the entire surface where the through hole should be and the other makes a cut around the perimeter so it can be pressed out of the substrate.

Using different hatching pitches and hatching patterns will also be investigated, to inspect their influence on quality.

To streamline the process and save time, various settings will be initially tested on a smaller sample before being implemented in the actual channel fabrication for engravings.

Characterization of quality and roughness

To assess the quality of the result, built-in LS-VIEW camera of the laser cutter provided an initial assessment of the quality of the results. However, this camera can not adjust the magnification, so a different microscope will be used as well.

The Keyence digital microscope provides high-quality imaging with a variety of magnification options, ranging from 20X

Figure 12: Representation of common etching settings

to 2000X. Additionally, it can generate 3D images for inspecting surfaces in 3D and assessing surface roughness. However, special attention and adjustments are essential to achieve optimal results when working with transparent glass. This involves using a marker to highlight the top of the glass slide for better contrast and conducting multiple trials to obtain accurate results without any unwanted spurious peaks.

2.2.6. Assembly plan

After laser fabrication of the gas exchanger layers, all layers were assembled according to the fabrication and assembly protocol detailed in Appendix B.2. The assembly process began with cleaning, which involved using an ultrasonic bath for three minutes on a full cycle, washing with dishwasher soap and warm water, cleaning with isopropanol alcohol (IPA), and drying on lint-free laboratory paper. Surface activation was then performed using a plasma gun (Piezo brush PZ3 from Relyon Plasma GmbH) for 30 seconds on each surface, repeated twice at standard 100%. The layers were aligned using the 3D printed alignment tool, and subsequently placed in an oven (Memmert) at 65°C for five hours, under compression by a nearly 2 kg piece of scrap steel. After these steps, the device layers were neatly bonded, and the ports were glued in the correct locations using super glue (Loctite, Super Glue-3). Safety precautions, such as careful handling of glue to prevent eye or skin contact and wearing appropriate personal protective equipment (PPE), are thoroughly discussed in Appendix B.3.

2.2.7. Experimental plan

Liquid Flow Testing

Liquid flow needs to be tested through each component to check for leakages. Milli-Q water was used in all liquid flow experiments for cost savings compared to a culture medium. First, the liquid will be perfused from the syringe to the Micronit chip without the gas exchanger in between.

During the next experiment, the liquid will be perfused from the syringe through the gas exchanger without the Micronit chip, at flow rates ranging from 35 μL/min to 245 μL/min. This variation in flow rates aims to assess whether different rates still avoid overpressurizing the device and causing leakages. This step allows for the detection of leakages from the sides of the sandwich structure or contamination into the gas channel. Signs of such issues include observing liquid exiting through the gas ports and noting a change in transparency within the gas channel, indicating potential liquid contamination. Laboratory paper towels, commonly used in labs to clean and dry surfaces, are placed around and under the device. By observing these towels and noting any brownish or wet spots, one can quickly identify if the chip is leaking.

Gas Flow Testing

Next, the gas flow without contamination or leakages into the liquid channel or from the sides of the sandwich structure will be tested by submerging the gas exchanger and N_2 gas flowing at 40 mL/min., without the gas flow reduction system connected, for easier bubble-seeing if they are present. hoping to see only bubbles at the gas outlet.

Next, the gas flow reduction system with the manual control valve and T-junction is tested by putting both gas tubes into a separate beaker glass at the same depth with the same amount of water. By turning the manual control valve, we should be able to adjust the bubbling rate and therefore the gas-splitting ratio in both beaker glasses. To lower the gas flow rate from 40 mL/min. to around 5 mL/min. the gas-splitting ratio should be 1:8. The pitch of the control valve that shows a bubbling ratio of 1:8 in the beaker glasses will be chosen for the next experiment where 5 mL/min. is desired.

Next, the reduced gas flow rate of ± 5 mL/min. needs to be tested into the gas exchanger. The manual control valve is kept at the same closing amount corresponding to a 1:8 gas-splitting ratio. A drop of water can be placed with a small syringe on the rim of the gas exchanger gas outlet to determine if gas flow exits through the gas exit, by checking bubbling behavior. Additionally, the liquid ports can be closed to ensure no gas leaks occur through those ways.

Oxygen Tightness Testing Without Gas Exchanger

The next experiments will be conducted to assess the oxygen tightness of the system. The aim is to investigate the limit case of oxygen-free water in an air-saturated ambient environment, as this scenario presents the largest gradient of oxygen concentration and is therefore most critical for evaluating potential oxygen leaks.

To achieve deoxygenated water in a beaker glass, the calibration procedure and materials utilized for achieving 0% of oxygen will be replicated, with the calibration steps and results presented in Appendix J. Milli-Q water will be placed inside a beaker glass, and pure nitrogen gas will purge the Milli-Q water free of oxygen. The gas-tight syringe will be charged with nitrogen gas at a flow rate of 2 L/min to ensure complete displacement of oxygen. Subsequently, the syringe will be emptied into the beaker glass, and water will be slowly drawn into the syringe until filled, ensuring a bulk of near oxygen-free water with minimal impact on liquid oxygen concentration.

For these experiments, the filled syringe will be connected to the syringe pump and tubing leading to the Micronit chip, bypassing the gas exchanger. Oxygen saturation will be continuously measured by the sensor spot while perfusion is initiated using the syringe pump.

Both experiments will adjust the liquid flow rate in increments of 35 μL/min. and will assess the steady state of each flow rate and will also stop perfusion and close the ports of the system to check for unwanted gas permeation through leaks. A laboratory stand with a clamp and hub head will be used to locate the optical fiber tip above the sensor spot for automatic data receiving during these experiments. This setup is shown in Appendix B.

Oxygen Saturation Regulation Testing Using Gas Exchanger

In this section, the testing procedure for the oxygen saturation regulation experiment examining the success of the gas exchanger will be outlined.

The initial steps mirror those used in the previous experiments. N_2 gas is drawn into the syringe, and Milli-Q water is deoxygenated using the established procedure. Subsequently,

the deoxygenated Milli-Q water is loaded into the syringe pump and perfused through the entire system at a rate of 35 μL/min.

After registering a plateau in air saturation by the Presens sensor, a gas flow of 40 mL/min. of N_2 gas is introduced through the gas exchanger to observe its impact on the result. Once a new steady state of air saturation is achieved, the gas flow is adjusted to 40 mL/min. of airflow. Following stabilization at this setting, N_2 gas is again introduced at a flow rate of 40 mL/min. in an attempt to reach the same steady state air saturation value as observed previously. This step aims to demonstrate the absence of hysteresis in the results.

3. Result

3.1. Optimized Fs Laser Fabrication Settings

This section shows a selection of the results of the parametric sweeps and concludes on the optimal settings for each job type. Appendix E shows all additional samples and all used settings.

3.1.1. General Sweeps Results

The images presented below illustrate the outcomes of four circle fabrication tasks conducted at different speeds. As depicted in Figure 14, the initial parametric sweep explored various speed configurations, revealing that speeds surpassing 1350 mm/s lead to a reduction in job precision, causing the circle to become more oval-shaped. At even higher speeds, job accuracy is completely compromised. On the contrary, excessively low speeds, such as 50 mm/s, result in reduced quality due to increased cracking in the glass substrate, as excessive energy is applied to the surface. The specific settings utilized are detailed in Appendix E.1.

(a) Speed: 50 mm/s   (b) Speed: 650 mm/s

(c) Speed: 1350 mm/s   (d) Speed: 1650 mm/s
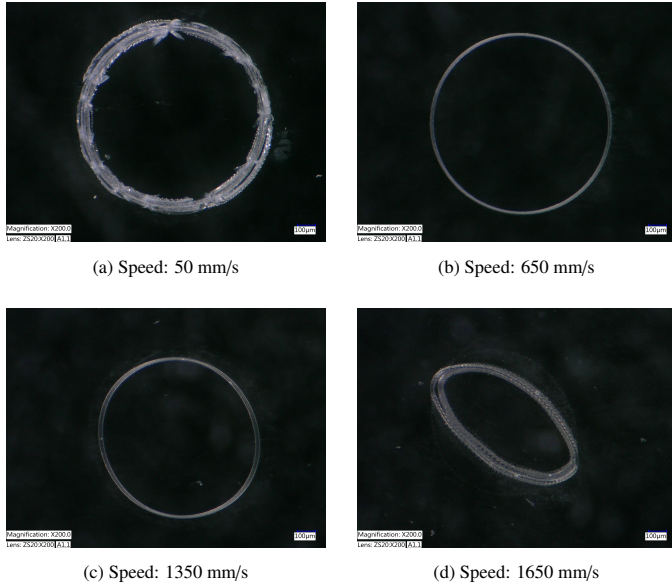
Figure 14: Circle fabrication results at different speeds

Moving forward, stage moving speeds are chosen to remain below 1350 mm/s to maintain dimensional accuracy. When using this specific set of parameters, speeds over 50 mm/s are employed to ensure optimal result quality.

3.1.2. Through Hole Optimization

Next, specific parametric sweeps are conducted for through holes. Initially, through holes are tested using perimeter cutting. Circles with varying outline pitches are examined to investigate substrate penetration during cutting, aiming to reduce processing time while achieving deep penetration. In Figure 15, the top-left of each subfigure presents a 3D heat map illustrating the sample's height distribution. However, this data can be influenced by spurious peaks due to the transparency of the glass, which should be disregarded. The top-right figure indicates the location where a section line is positioned over the groove. The lower subfigure of each panel exhibits the surface profile along the section line from both sides of the groove. Comparing this highlights that smaller outline pitches facilitate effective and deep cutting, except for the sample smaller than 0.025 mm (the laser spot size), whereas larger pitches lead to reduced efficiency due to insufficient overlap between outlines. The sample demonstrating the optimal rectangular channel shape, characterized by superior penetration of approximately 100 μm, surpassing that of the other samples by at least twofold, and minimal dimensional loss, is the second sample, featuring the deepest and narrowest groove. This establishes an optimal outline pitch of 0.025 mm. All utilized settings are detailed in Appendix E.2.

Using the determined optimal outline pitch, we investigate the impact of additional repetitions on the quality and depth of the resulting groove, with detailed settings provided in Appendix E.3. Analysis of the surface profile depicted in the lower portion of each subfigure in Figure 16 reveals that initially, a higher number of repetitions enhances the etching depth. For instance, all samples with 400 or more repetitions exhibit an etch depth exceeding 100 μm, whereas those with fewer repetitions typically range from 70 to 90 μm in depth. However, employing more than 400 repetitions does not notably augment the depth, as most samples maintain a depth close to 100 μm, albeit with slight variations across the groove, evident from the 3D height difference heat maps in the top left of each subfigure. To optimize job efficiency, repetitions are capped at 400 times, as further increases offer minimal improvement in etch depth while prolonging job duration.

Next, through holes were created using two distinct methods: perimeter cutting and area hatching, chosen based on result quality and time constraints. Perimeter cutting employed the previously established optimal outline pitch and number of repetitions. Since the results from the repetition sweep attempts did not achieve full penetration of the 1 mm glass substrate thickness, incremental layering was implemented. This involved the Aerotech stage moving up in defined step increments following specific prompts during the laser job. By adjusting the stage position in increments of 0.1 mm, which corresponded to the observed groove depth from the earlier experiments, the laser maintained focus on the material being removed, thus enhancing cutting efficiency. This stage movement strategy was applied to both cutting methods.
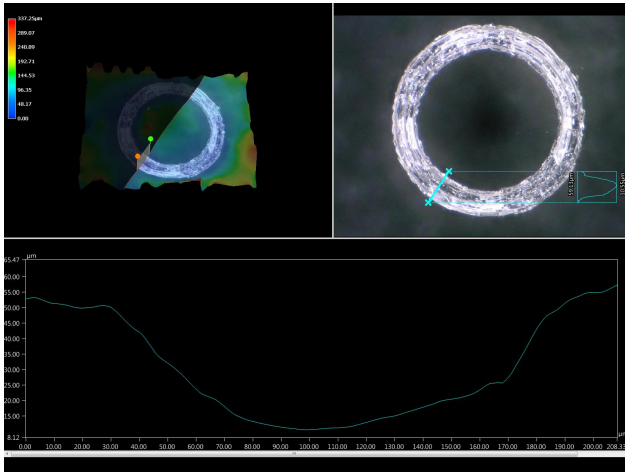
During perimeter cutting, the laser encountered difficulty fully penetrating the substrate due to glass debris accumulating
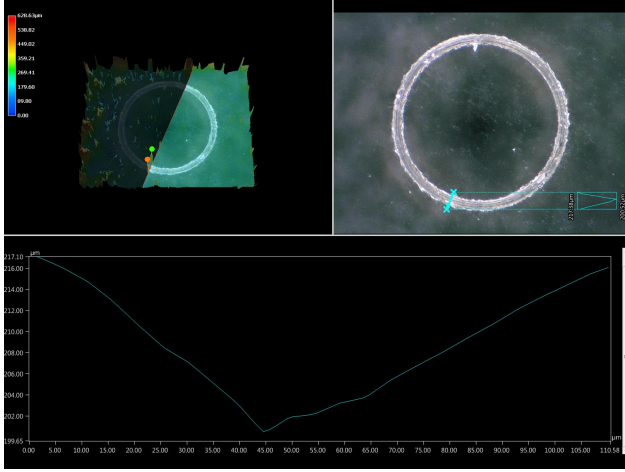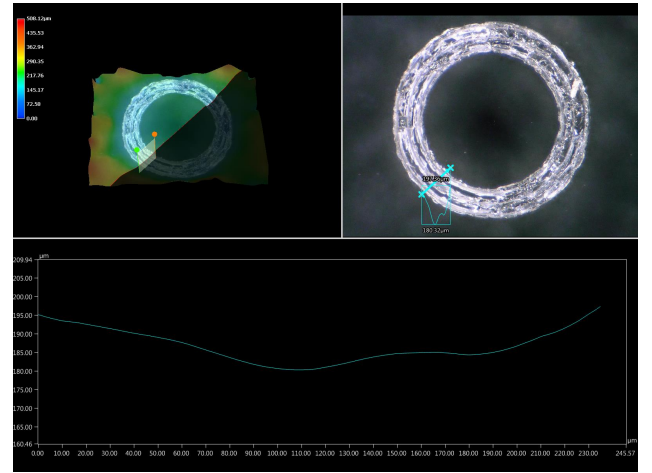
(a) Outline Pitch: 0.025 mm
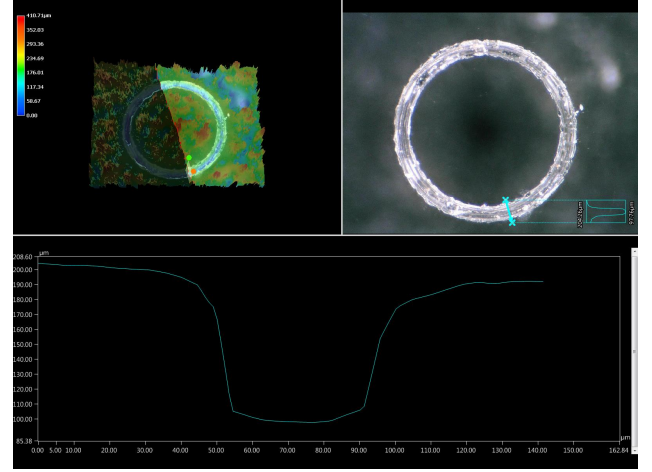
(b) Outline Pitch: 0.0125 mm

(c) Outline Pitch: 0.0625 mm

(d) Outline Pitch: 0.075 mm

Figure 15: Effect of different outline pitches on etch depth and groove quality

(a) Repetitions: 100

(b) Repetitions: 400
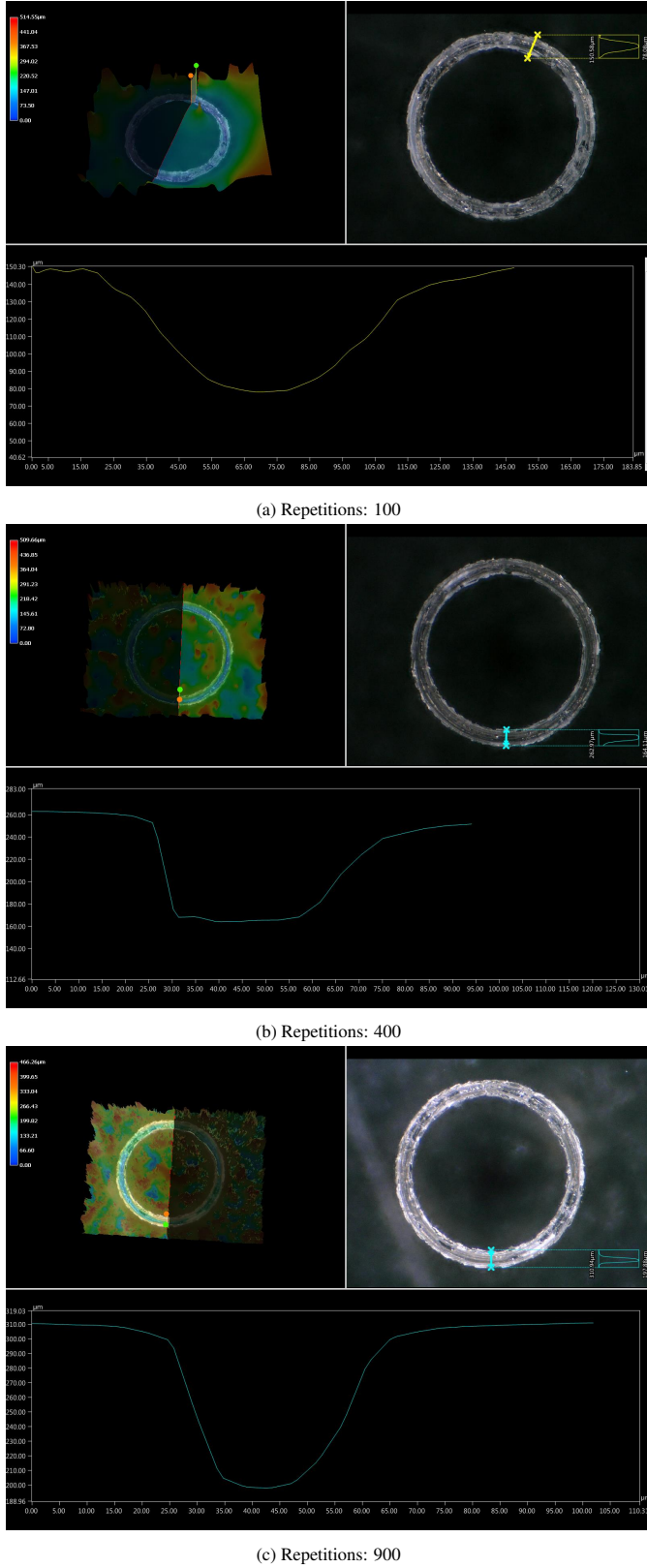

(c) Repetitions: 900

Figure 16: Effect of different number of repetitions on etch depth and groove quality

inside the groove. Despite attempts to remove material layer by layer, the groove became too deep and narrow for effective fume extraction, leading to obstruction by glass debris. Subsequently, the substrate was flipped upside down, and the process was repeated from the backside to achieve complete cutting through. The loose centerpiece could then be removed, typically with tweezers.

The results of both methods are visually presented in Figure 17. Orange and green markers define the analyzed line's beginning and end in the upper left section of both subfigures, with the line viewed from a different angle in the upper right corner. The height profile of each point along this line is displayed below, providing insight into the through hole's dimensional accuracy.

Analysis of these profiles reveals a gradual decrease in height after the hole's edge for both methods, contrary to the anticipated sharper decline. Notably, the through hole created via area hatching displays a spurious peak in the height profile, likely due to imperfections on the microscope bed, which should be disregarded in the assessment.

Further calculations on the slope of the hole wall, detailed in Appendix K, show perimeter cutting with a slope absolute value of 9.36 m/m and area hatching with a slope absolute value of 3.5 m/m. Despite both holes being intended to be 1.8 mm in diameter, they are smaller, with the perimeter cutting hole around 1470 μm and the area hatching hole nearly 1250 μm, as estimated in Appendix K as well.

Comparing the methods, perimeter cutting demonstrates higher quality, dimensional accuracy, and slope value along the hole's wall. It exhibits fewer debris remnants on the side walls and a more pronounced decrease in height after the hole's edge, ensuring a more consistent hole diameter.

Both methods required approximately 30 minutes for 1.8 mm diameter holes, although part of the time for perimeter cutting was allocated to manually flipping and realigning the sample. As hole size increases, preference is given to perimeter cutting to reduce processing time, considering the slight increase in perimeter compared to the quadratic increase in surface area with diameter. However, for smaller holes (¡0.5 mm), area hatching may be preferred to avoid challenges in center part removal without appropriate tools. All utilized settings are documented in Appendix E.4.

3.1.3. Channel Engraving Optimization

Initially, a comprehensive array of rectangles with different settings is generated. The used settings are in Appendix E.6. Notably, the hatch pattern significantly impacts the outcome. As depicted in Figure 18, three distinct hatch patterns, namely horizontal, erode, and 135-degree diagonal, were employed. The erode pattern was deemed unsuitable for this task primarily due to its lack of uniform flatness, whereas the 135-degree diagonal and horizontal hatch patterns demonstrated similar, improved results. Notably, these two patterns exhibited fewer irregularities and a flatter surface profile compared to the erode pattern, which is crucial for a flow channel. Moreover, the horizontal hatch pattern yielded an even flatter surface than the 135-degree diagonal hatch pattern. Additionally, it's worth men-

(a) Perimeter cutting result
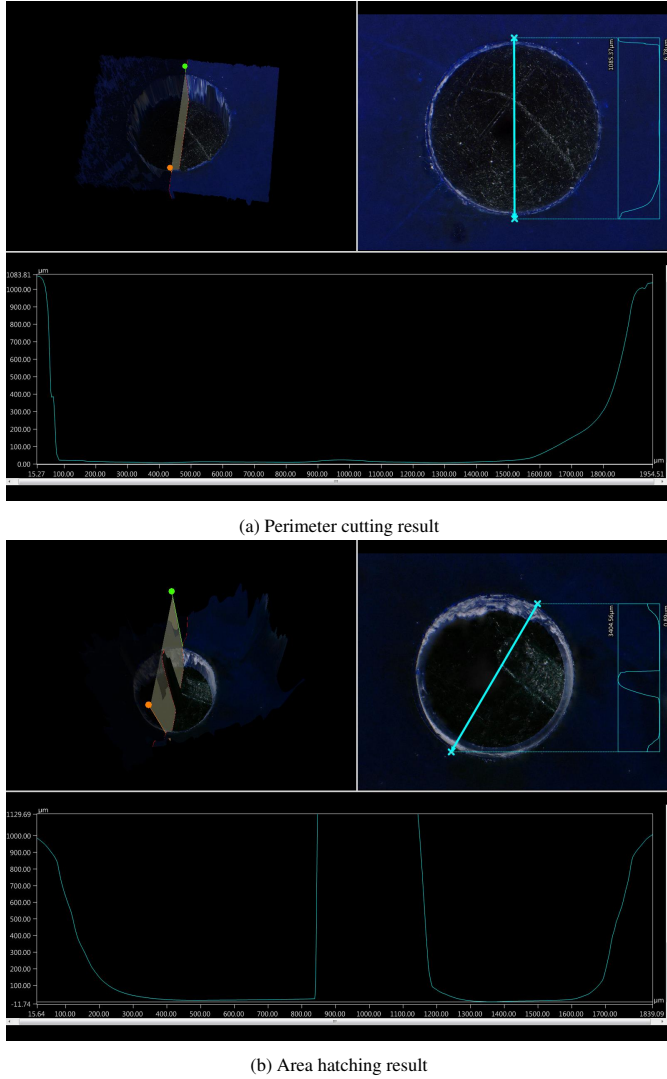

(b) Area hatching result

Figure 17: Results of through hole methods used, comparing area hatching and perimeter cutting

tioning that the depth of the channel varied among the samples, with the horizontal and erode hatch patterns reaching a maximum depth of approximately 200 μm, while the diagonal hatch pattern reached a maximum depth of around 150 μm. From this point forward, the horizontal hatch pattern will be employed.

Within the remaining set of rectangles, configurations featuring low power settings exhibited notably smoother channel prospects. As depicted in Figure 19, two rectangles sharing identical settings except for power are compared. It is observed that a decrease in power results in a rapid reduction in channel etch depth. Specifically, the sample with power=0.15 Watts, the minimal value possible, achieves a depth of only around 100 μm, whereas the job with power=0.45 Watts yields a depth of approximately 250 μm. Nevertheless, the fabrication of these channels took several hours due to the slow stage moving speed, small hatch pitch, and large number of repetitions, rendering them impractical for real gas and liquid channels.

To find a more time-efficient combination of settings suitable, with again a relation between etch depth and laser settings, circles were fabricated. The used settings for these circles are in Appendix E.9. The outcomes of these experiments are depicted in Figure 20, showcasing channels of different depths tailored for specific applications. Specifically, Figure 20a exhibits a channel with a depth of nearly 300 μm, well-suited for the liquid channel. Conversely, Figure 20b portrays a channel with a depth of approximately 500 μm, having the desired depth for the gas channel.

To explore the impact of hatching pitch variations and the use of fume extraction on channel quality, three miniature versions of the liquid channel design are fabricated, each with distinct configurations.

Firstly, sample K1 is created using previously optimized engraving settings but with fume extraction from only one direction. Subsequently, sample K2 incorporates fume extraction from two different directions, albeit with a different parameter set while maintaining the same total energy, as per Equation 2. In this equation, Energy (E) represents the amount of energy, power (P) denotes the rate of energy transfer, the number of repetitions (N) refers to the count, speed (V) signifies the velocity and hatch pitch (Hp) represents the distance between successive passes. Lastly, sample K3 is fabricated using the optimal settings with fume extraction from two directions. For sample K3, the optimal settings are applied alongside fume extraction from two directions.

For the samples where the fume extraction is changed, the sample itself is turned 180 degrees, since the fume extraction hose is not long enough to move into a much different angle. Since the Aerotech stage cannot rotate, the samples were manually turned, and using the same orientation point on the glass slide, the starting point of the job could be retrieved. Figure 21 shows the setup with the fume extraction on, and a sample being processed in the middle.

Figure 22 showcases the resulting 3D images and channel profiles. Sample K1 exhibits an inclined channel bottom instead of the desired flat bottom. Conversely, sample K2 displays a uniform flat-bottomed channel. Sample K3, however, exhibits significant roughness, resulting in a non-uniform channel shape
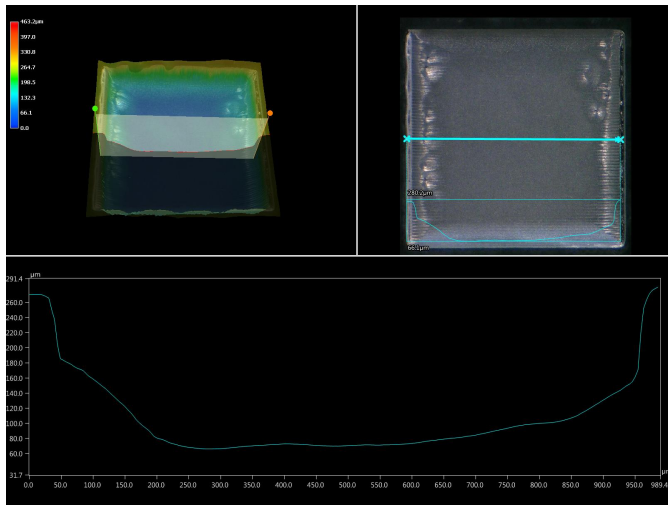
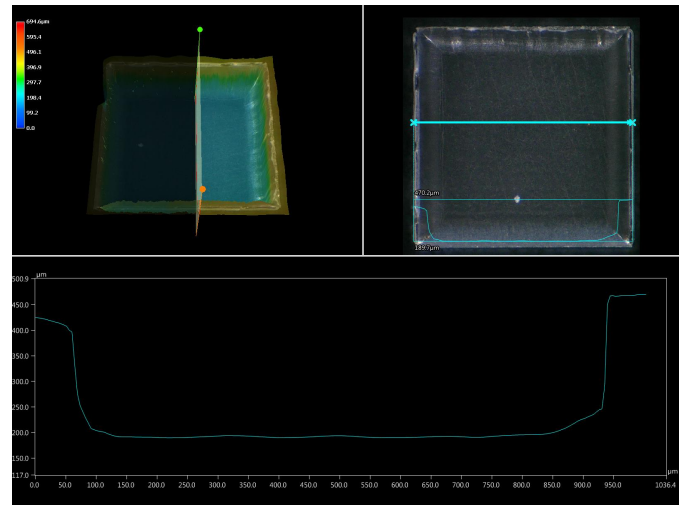(a) Horizontal hatching pattern on sample Square 6
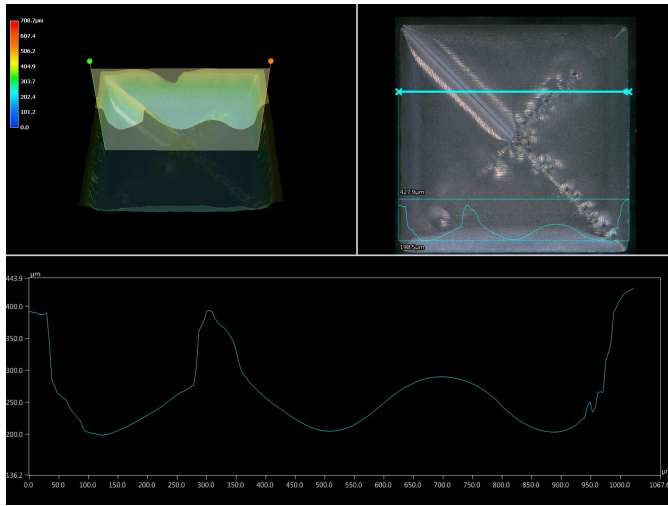
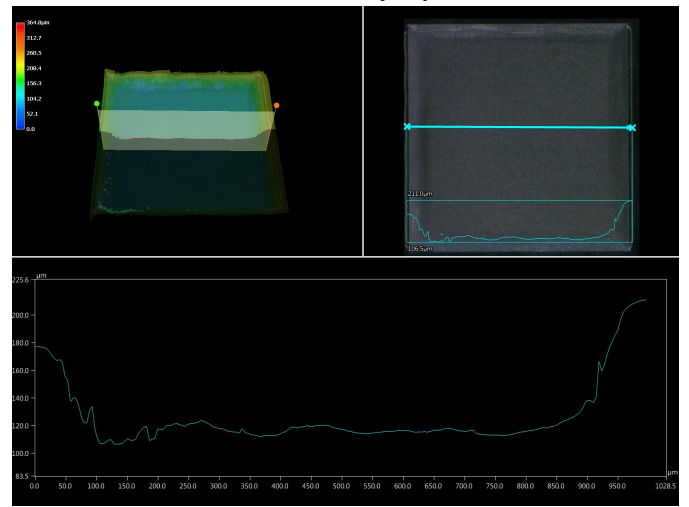(b) Erode hatching pattern on sample Square 7
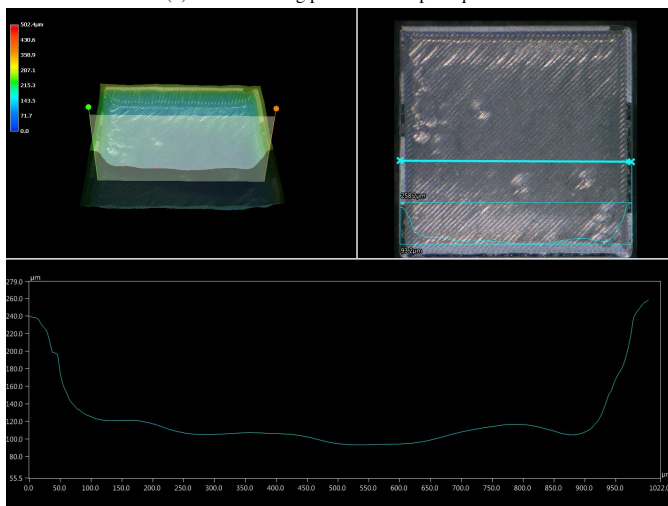
(c) 135-degree diagonal hatching pattern on sample Square 8
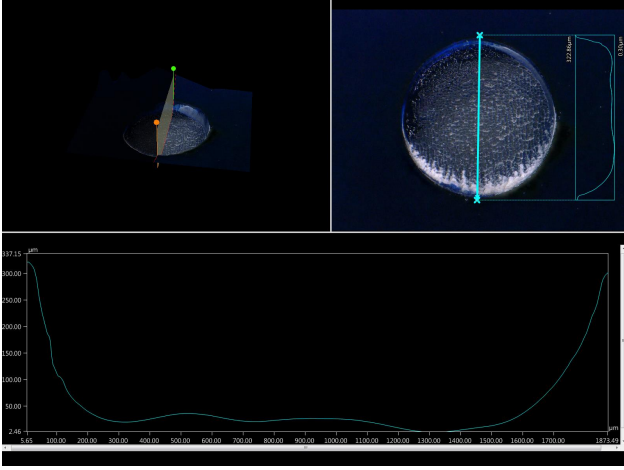
Figure 18: Different hatching patterns

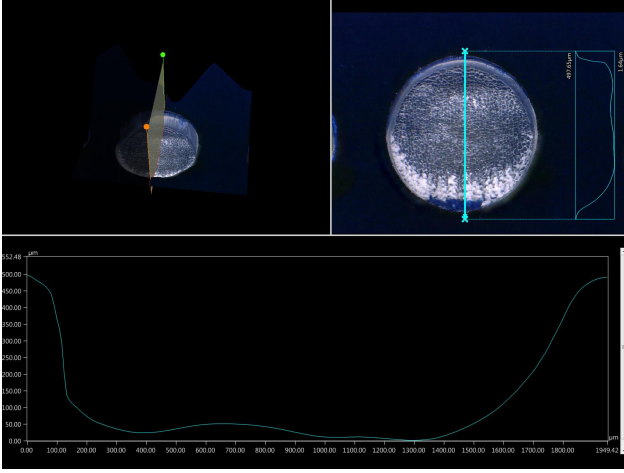(a) 0.15 Watts on sample Square 9

(b) 0.45 Watts on sample Square 10

Figure 19: Two low power hatching channels

(a) Channel sample J

(b) Channel sample F

Figure 20: Overview and surface profile of circular channel samples

lacking a flat bottom.

The surface roughness analysis of samples K2 and K3 is evaluated for their potential as fluidic channels with a flat-bottomed shape. S_a and S_z values are determined by equations 3 and 4, respectively, focusing on surface roughness at the center of the channel. In this roughness analysis,

S_a is the arithmetic average roughness, A is the area of the surface being measured, $z(x, y)$ is the height of the surface profile at position (x, y), and S_z represents the maximum peak-to-valley height, where S_p is the maximum peak height within the evaluation area, and S_v is the minimum valley depth within the evaluation area. Both S_a and S_z are wished to be as low as possible for our application as a smooth microfluidic channel.

From the surface roughness determination in Appendix B, sample K2 demonstrates lower roughness values (S_a= 12.2 μm, S_z= 117.5μm) compared to sample K3 (S_a= 60.2 μm, S_z= 334.5μm), indicating superior flat-bottomed uniform channel quality.

In conclusion, altering the fume extraction direction and employing a lower hatch pitch result in enhanced microfluidic channel quality.
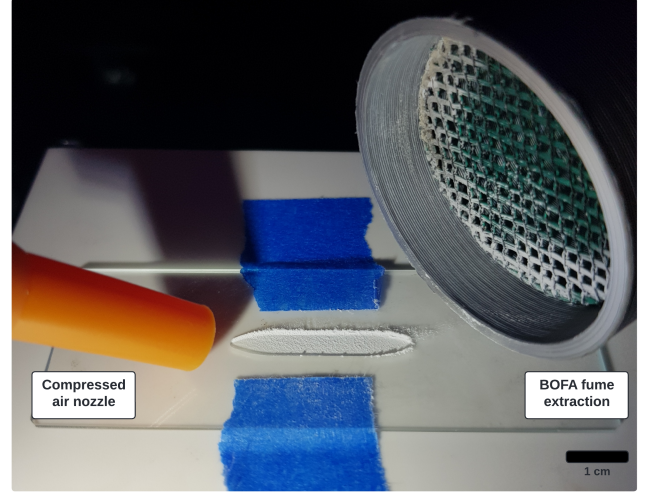
Figure 21: Fume extraction in action during laser fabrication. The orange nozzle emits compressed air, while the adjacent fume extraction system on the right draws in the air

$$E \propto \frac{P * N}{U * Hp} \tag{2}$$

$$S_a = \frac{1}{A} \iint_A |z(x, y)| \, dx \, dy \tag{3}$$

$$S_z = S_p + S_v \tag{4}$$

3.1.4. Gas Exchanger Fabrication and Assembly

With the optimal parameters identified, we can now proceed with the actual device fabrication. Figure 23 shows all subsequent fabrication and assembly steps. Colored boxes denote which sandwich structure layer is involved in that particular step. The assembled chip is shown in figure 25. The used settings for the real device are shown in Figure 24a and Figure 24b. Appendix A shows images of the assembly process.

3.1.5. Sensor Hole Fabrication and Sensor Integration

Before sensor hole fabrication, the sensor spot is measured. Appendix L shows the sensor spot top view, including the radius measurement. The radius is estimated to be 985 μm. The height of the sensor spot is measured to be 220.9 μm, also visible in Appendix L. The sensor hole fabrication settings are shown in Figure 24c. A circle with a diameter of 2.14 mm is used as shape input. This wider and deeper sensor hole job is used to compensate for dimensional losses and debris clogging the sensor hole side walls and bottom during Fs laser fabrication. A 3D surface representation from two angles and the hole surface profile is visible in figure 26. The sensor hole has debris influence on the bottom of the hole. The hole is nearly 1800 μm wide, and the top part of the hole without debris is still around 400 μm deep. Due to the slightly smaller diameter of the hole compared to the sensor spot, the sensor spot can be

13
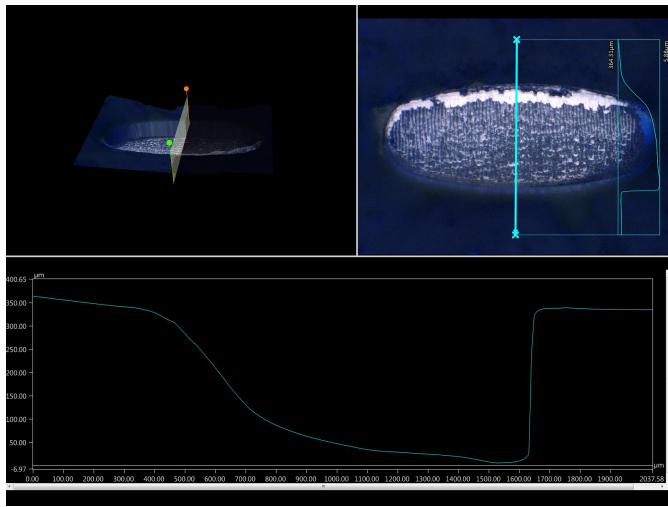
(a) An inclined channel shape, sample K1
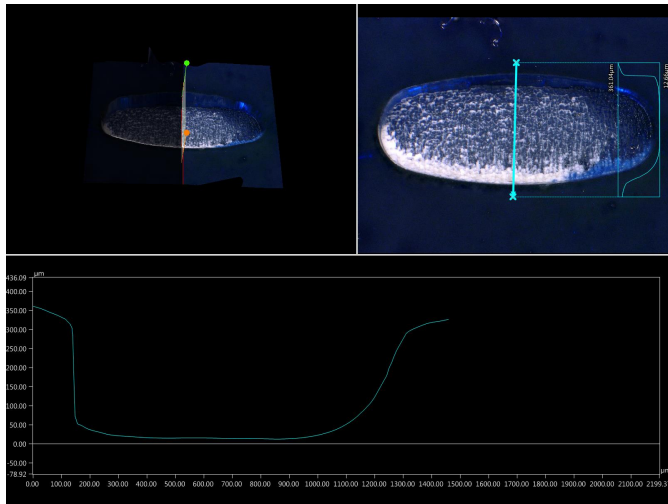
(b) A smooth flat-bottomed channel shape, sample K2
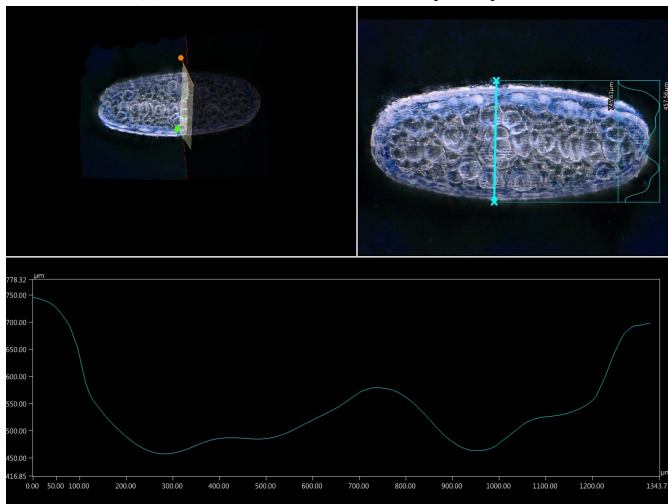
(c) A rough channel shape with larger irregularities, sample K3

Figure 22: Miniaturized liquid channel samples employing different hatch pitches, with some utilizing fume extraction while others do not
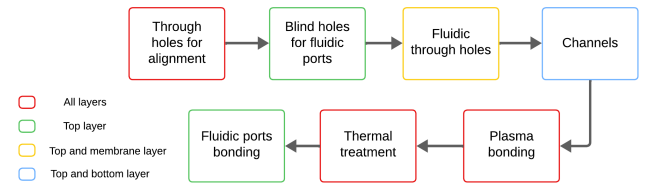

Figure 23: Fabrication and assembly steps

Sample	Power(%)	Speed(mm/s)	Repetitions(N)	Outline pitch(mm)	Outlines	Layers(N)	Layer pitch(mm)	Hatch pitch(mm)	Hatch pattern	Note
Through holes alignment	40	100	300	0.025	3	10	0.1	N/A	N/A	Flip over and repeat, diameter=2 mm
Gas through hole	40	100	300	0.025	3	10	0.1	N/A	N/A	Flip over and repeat, diameter=1.7 mm
Liquid through hole	15	150	10	N/A	N/A	10	0.1	0.0015	horizontal	Diameter=0.3 mm

(a) Gas exchanger through hole settings

Sample	Power(%)	Speed(mm/s)	Repetitions(N)	Layers(N)	Layer pitch(mm)	Hatch pitch(mm)	Hatch pattern	Note
Liquid channel	10	100	4	4	0.075	0.0015	horizontal	Turn sample 180-degree after 2nd layer
Gas channel	10	100	4	6	0.075	0.0015	horizontal	Turn sample 180-degree after 3rd layer

(b) Gas exchanger channel settings

Sample	Power(%)	Speed(mm/s)	Repetitions(N)	Hatch pitch(mm)	Hatch pattern	Layers(N)	Layer pitch(mm)	Note
Sensor hole	15	150	5	0.0015	horizontal	10	0.05	2.14 mm diameter; 10 times lowered by layer pitch

(c) Sensor integration hole settings

Figure 24: Gas exchanger and sensor integration settings
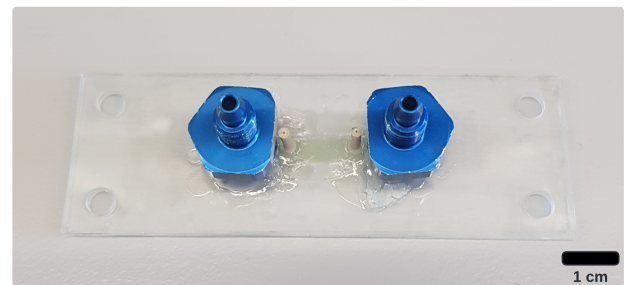
Figure 25: The assembled gas exchanger, the blue ports for gas flow, and the brownish ports for liquid flow

tightly inserted into the hole without the need for glue, by applying a slight amount of pressure. The sensor integrated into the Micronit chip is visible in figure 27.

3.2. Experimental results

This section briefly describes and shows the key results from the experiments.

Liquid flow happened without leaks from the syringe pump through the Micronit chip without the gas exchanger firstly with 35 μL/min, which is the actual liquid flow rate in the oxygen regulation experiment.

In the initial stages of the second liquid flow experiment, utilizing liquid flow at a rate of Q=35 μL/min. without concurrent gas flow from the syringe pump through the gas exchanger to the Micronit chip, liquid leakage occurred through the tube-port connection of the gas exchanger, because of some clearance in the connection. To address this issue, the connection was carefully adjusted by gluing the needle gauge into the tubing with super glue. A microscope image of this procedure is shown in Appendix H.2. Following this adjustment, the experiment was repeated, and it demonstrated successful liquid flow through the gas exchanger's liquid channel at all used liquid flow rates ranging from 35 μL/min to 245 μL/min, without any leakage or contamination into the gas segment. Additionally, there were no observed leakages on the sides of the sandwich structure or the laboratory paper towel. This successful perfusion through the system confirms its operational integrity.

Next, in the first gas flow experiment as described in section 2.2.7, the gas exchanger is submerged and N_2 gas with the minimal gas flow rate of 40 mL/min. is pushed into the gas exchanger inlet, without any bubbles coming out of the liquid inlet or outlet or the sides of the sandwich structure, but only from the gas outlet. This shows the successful gas flow from the inlet to the outlet.

The second gas experiment where the gas-splitting is tested showed the ability to successfully change the bubbling rate and therefore the gas flow rate ratio between both streams. A video of this experiment is visible on YouTube, the link can be found in Appendix P. The control valve pitch corresponding to a nearly 1:8 ratio is set accordingly.

In the third gas flow experiment, a N_2 gas flow of nearly 5 mL/min. is tried to be perfused into the gas exchanger's gas channel. However, when placing a small water drop on the gas exchanger's gas exit, no signs of gas flow/bubbling are visible. The drop stays in place on the rim of the gas outlet. The placement of the water drop is shown in Appendix B. Just to be sure the liquid ports are not the reason for the leaking gas, the liquid ports are blocked. When placing a water drop on the gas tube on the other part of the T-junction bubbling is visible. From this, we can conclude that the gas flow reduction system is not operating properly because the gas exchanger introduces a large hydraulic resistance, making all the gas leave the system in the way of least resistance. Since we can not generate smaller flow rates than 40 mL/min. per gas type with the Bronkhorst system, we continue with this flow rate instead of 5 mL/min. Therefore, we can only use the gases available without mixing them since we do not want to increase the total gas flow rate even more.

The sensor data from the oxygen tightness experiments is plotted in Figure 28 and Figure 29. The x-axis represents the measurement time step in minutes, while the y-axis displays the percentage of air saturation. Different colors denote varying flow rates supplied by the syringe pump. The colors for each flow rate and the graph's x and y limits are identical.

A comparison of the results reveals that the second experiment resulted in better deoxygenation within the Micronit chip since this experiment reached a lower air saturation value (1% at 175 μL/min. in Experiment 2) versus (8.5% at 175 μL/min. in Experiment 1). Halting the flow while blocking the liquid outlet tube of the Micronit chip demonstrated significant diffusion back into the chip in both experiments, indicating a lack of oxygen tightness in the system. Additionally, the highest flow rate of 175 μL/min. appeared to reach near equilibrium (0.0099 %/min. in Experiment 1 and 0.0173%/min. in Experiment 2) with the undesired oxygen permeation into the Micronit chip in both experiments. This near-equilibrium determination is shown in Appendix M.

Next, the last experiment with the gas exchanger introduced into the system is performed. The experimental setup is visible in Figure 30. Different gases are introduced to determine the response and validate the successful working of the gas exchanger for oxygen regulation inside the Micronit chip. Initially, the liquid is perfused at a flow rate of 35 μL/min. for the entire experiment. The resulting plot is visible in Figure 31. Again, the x-axis and y-axis feature the same quantities as the preceding plots. Different colors distinguish different input gases into the gas exchanger system. In this experiment, only the limit cases of air and pure N_2 gas are introduced, because a combination of both gases would further increase the total input gas flow rate, due to the minimal gas flow rate of 40 mL/min. of each MFC. A few data points show inaccurate results, mainly around t=120min. where the user unintentionally bumped the probe, causing the probe to be misaligned with the sensor spot resulting in some inaccuracies. The gas exchanger works partially since introducing different gases leads to different air saturations in the Micronit as expected. Appendix D.3 shows the MATLAB files for visualization of the oxygen sensor data, used to create Figures 28,29,31.

4. Discussion

The forthcoming discussion section explores the outcomes of the microfluidic gas exchanger fabricated in glass using an Fs laser.

4.1. Interpretation of Findings

From the fabrication, through holes seem to be very difficult to make using a perimeter cut without flipping the device over and cutting from the bottom side as well, because debris hinders the etch depth with such a high aspect ratio. For smaller holes, hatching seems a good option, but compromises a bit on the result. Channels with relatively low surface roughnesses of $\pm(S_a= 12.2\ \mu m$ and $S_z= 117.5\mu m)$, can be fabricated successfully with reasonable dimensional accuracy. However, compared to smooth surfaces like standard borosilicate glass slides,
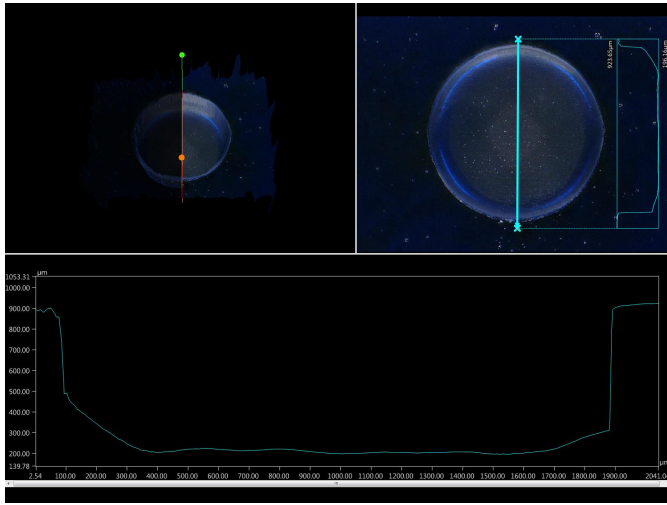
Figure 26: Sensor spot hole characterization

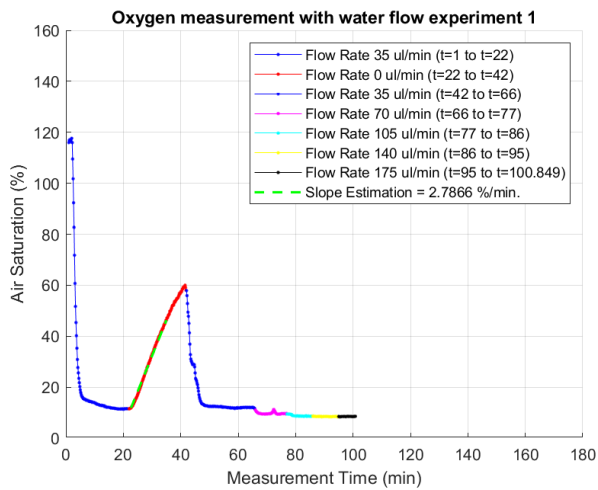Figure 27: Sensor spot integrated into the Micronit chip

Figure 28: Air saturation over measurement time graph for the first experiment conducted without the gas exchanger integrated into the system. This graph illustrates the variation in air saturation levels throughout the measurement period, providing insight into the dynamics of air saturation in the absence of the gas exchanger.
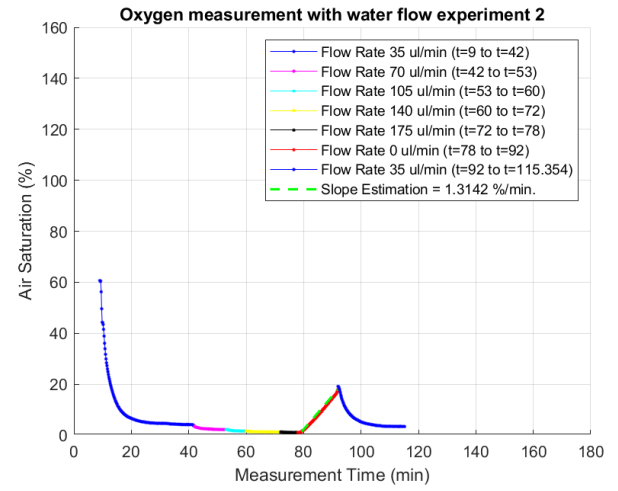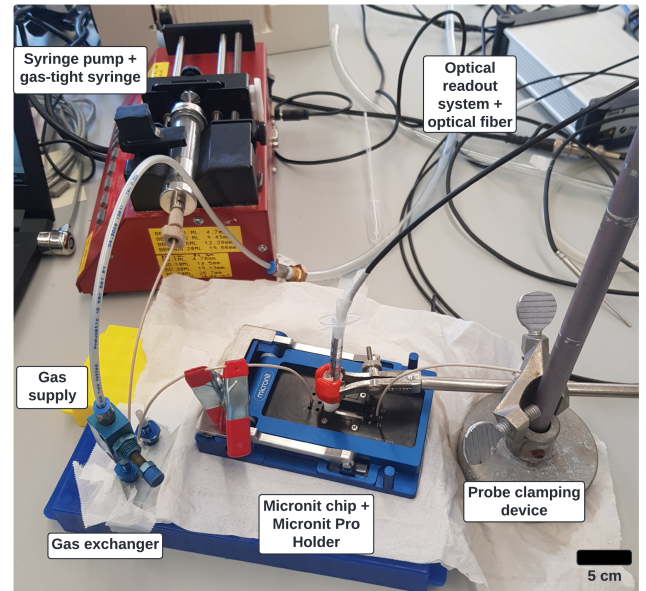

Figure 29: Air saturation over measurement time graph for the second experiment conducted without the gas exchanger integrated into the system. This graph illustrates the variation in air saturation levels throughout the measurement period, providing insight into the dynamics of air saturation in the absence of the gas exchanger.

Figure 30: The experimental setup for the oxygen regulation experiment
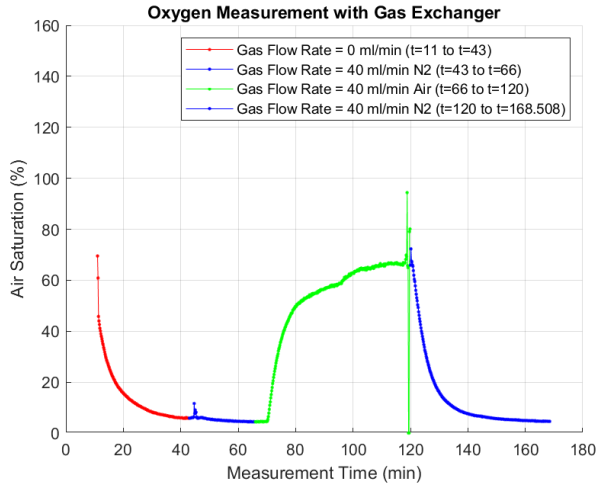
Figure 31: Experiment 3: Oxygen regulation with gas exchanger. This graph displays the fluctuations in air saturation levels throughout the measurement period with the gas exchanger integrated into the system.

which often exhibit surface roughnesses of less than several nanometers (Preedy, Emily et al. (2014)), the surface roughness of the fabricated channels remains relatively high. On a positive note, sensor integration appears to be successful.

From the experiments, the system is sensitive to unwanted gas permeation. The gas exchanger system seems to be working and responds quickly to a change in input gas through the gas channel. Liquid and gas flow are both feasible through the entire system, albeit the gas flow at a higher flow rate, since the gas reduction system did not work. The sensor spot integration seems successful and does not hinder the liquid flow in the Micronit chip, but brings back the signal amplitude in the current fiber holder system causing a small loss of accuracy of the air saturation values.

4.2. Comparison with Expectations

After analyzing the results, the results are compared to the expectations.

Channel engraving and through hole fabrication:
Initially, using Fs laser ablation for micromachining delicate structures in a glass substrate was anticipated to yield high dimensional accuracy and efficient removal of precise parts of the glass substrate. However, despite the integration of a fume extraction system by the technical staff, debris clogging emerged as a significant issue, undermining these expectations. The feasibility of through-hole fabrication through perimeter cutting from the top side alone was also anticipated, but it proved unfeasible due to debris clogging. Moreover, dimensional accuracy was compromised, with all samples exhibiting smaller dimensions than desired.

A slower response compared to the COMSOL model:
In the oxygen regulation experiment, the concentration adjustment takes a lot longer compared to the COMSOL model. Where in the COMSOL model t=360 seconds to reach a steady state, in the real system around 30 minutes or t=1800 seconds is needed to change a concentration and reach a steady state.

This can be partially explained by the distance the liquid needs to travel from the gas exchanger to the Micronit chip, where the concentration is measured. This introduces a delay in the response, which is not taken into account in the COMSOL model. But this is calculated to be a little less than 1.5 minutes according to calculations in Appendix D. Besides that, the COMSOL model uses smooth surfaces and perfect laminar flow, whereas the real channel has a certain roughness and potential turbulence due to the not ultra-smooth shape of the channels. This could hinder optimal mass transfer rates. Besides, both the liquid flow rate and the gas flow rate are not quantitatively monitored, so this could potentially be faulty since back pressure on the gas supply and the syringe could result in a lower actual flow rate into the system. A lowered gas flow rate is modeled in Appendix G but does not show sensitivity at least at 8-fold smaller gas flows.

The gas exchanger system was unable to achieve full saturation range:
This can not be explained by the not gas-tight behavior of the system, because when adding air through the gas exchanger into the system the leakages would only further improve oxygen introduction into the liquid as long as there is a gradient. Since the curve reaches a steady state at around 66% of oxygen saturation, the gas exchanging through the membrane into the liquid flow and the oxygen leakages are in balance with the initially oxygen-free liquid from the syringe. This concludes that the diffusion is not happening efficiently enough in the gas exchanger, which contradicts the COMSOL model. One difference between the COMSOL model and the real system is the gas flow rate, which is increased 8-fold to 40 mL/min. in the oxygen regulation experiment as discussed in Chapter 3.2, but this would only introduce more oxygen into the gas exchanger. The increased gas flow in combination with the relatively rough surface could introduce turbulence in the gas channel, causing a larger pressure drop in this channel. This could cause a larger pressure difference over the membrane, stretching the PDMS layer more than expected which narrows the liquid channel. This could increase the liquid flow velocity through the gas exchanger, limiting the time for oxygen diffusion. Sensitivity showed the gas exchanger is not sensitive to flow velocity changes in this domain. On the other hand, this blocking decreases the diffusion distance, which could contribute to better diffusion. However, sensitivity analysis using a deformed model does not show the system to be influenced within these ranges. These sensitivity analyses are detailed in Appendix G.

Difference between both the same experiments without gas exchanger:
From Chapter 3.2 both experiments without the gas exchanger show oxygen leakage after liquid flow stopping, but both have a different slope of the curve after stopping the flow. This slope is estimated and shown in green in both figures. A different slope is expected since the air saturation when stopping the flow has a lower value in the second experiment and thus a larger diffusion gradient with the ambient air. To compare the slopes reasonably, the same time difference between the estimation slope line begin and endpoints is used to check for differences in slope. This estimation slope shows a lower slope value for Experiment

2, But based on the diffusion theory, the slope of this experiment should be larger than Experiment 1. This suggests some unexpected variational influence between experiments, most likely in the operator's contribution to connecting the tubing to each part of the system. This could be in only a few places namely, the syringe and the tubing, the tubing inside the ferrule, and the Micronit chip at both the inlet and outlet. To conclude, in Experiment 1 more leaks are present, and therefore steady state is reached at a relatively high air saturation compared to Experiment 2. When stopping the flow, these leaks cause Experiment 1 to oxygenate quicker, even though having a lower oxygen gradient than Experiment 2. The impact of these leaks is unmistakable and has the potential to disrupt the entire system effortlessly.

4.3. Implications and Insights

This project underscores the feasibility of fabricating a microfluidic gas exchanger using an Fs laser, enabling the seamless flow of both gas and liquid through channels without experiencing leakages or cross-contamination. It demonstrates the potential for producing intricate structures for similar microfluidic applications, presenting advantages over other methods involving hazardous fabrication steps like Hydrofluoric Acid (HF) wet etching. However, challenges encountered, such as debris clogging leading to imperfect channel shapes and difficulty achieving total penetration, highlight the limitations of this fabrication method, particularly in contexts requiring high accuracy and dimensional correctness. These insights point to areas for improvement and suggest potential research avenues, such as investigating enhanced fume extraction methods to effectively remove glass debris and address challenges in future fabrication processes.

The use of glass slides for microfluidics is an interesting direction since glass slides are cost-effective and widely available. However, glass slide used in the fabrication process possesses dimensional tolerances that can significantly impact the accuracy and alignment of the fabricated microstructures. Identifying the corner or reference point on the glass slide before commencing fabrication is imperative to mitigate potential misalignments and ensure the precise positioning of microfluidic channels or other structures. This precaution becomes particularly crucial when aligning fluidic ports, where even minor misalignments can compromise device functionality or performance. By addressing these dimensional tolerances and implementing strategies to locate the starting point for fabrication accurately, researchers can enhance the reproducibility and reliability of microfluidic devices produced via Fs laser fabrication methods.

The Fs laser fabricated structures take very long fabrication times, for instance, the gas channel took over 5 hours of fabrication and for better results, the channel was manually brushed to remove glass debris each time the stage was moved to a different height. This increased operation time and was not very efficient for the operator. An Fs laser is not a perfect fabrication method for larger structures needing similar quality. The same goes for mass production using an Fs laser, the focus area is relatively small, and moving the stage takes additional time. Besides dimensional tolerances, it is challenging to fabricate multiple devices simultaneously with good similarity, especially since they can differ in the amount of fume extraction since the airflow is fixed and the stage has no full moving freedom. Smaller and only three alignment holes should guarantee the same optimal alignment and still constrain the position and orientation of the layers, but lower fabrication time, note that one of the current through holes took over half an hour.

This project's accomplishment of zero dead-volume integration of sensors into glass substrates represents a significant breakthrough, offering a promising avenue for a wide range of research endeavors where sensor integration into glass is imperative.

This project gives insights into the prototype working of the miniaturized microfluidic oxygen regulation system, but gas permeation leakages need to be addressed better and mitigated a lot more in future research. One potential avenue for improvement is to merge components to reduce separate elements and integrate them into a single device. This could help minimize the number of connectors, thereby enhancing oxygen tightness and reducing the risk of leaks. Additionally, streamlining the design in this manner could simplify assembly and operation, ultimately leading to a more reliable and efficient system.

Another notable improvement could involve creating more distance between the liquid and gas ports to facilitate connecting the gas exchanger's liquid port to the peripheral tubing. Currently, a design flaw limits the space available, making it challenging to fit a microfluidic union between the liquid port and additional tubing due to the wide hexagonal shape of the gas port. To address this issue, using a larger piece of tubing for the liquid channel could provide the necessary space for the microfluidic union installation without hindrance from the gas port. This adjustment would eliminate the reliance on a fragile needle gauge glued between the tubing and the liquid port for the tube-port connection.

In this project, nitrogen sparging was employed for oxygen removal through bubbling. However, it's worth noting that this method may pose practical challenges when dealing with a culture medium. Agitation during nitrogen sparging could induce foaming and denaturation within the medium, potentially affecting experimental outcomes. It's important to acknowledge that while a desiccator would have been a preferable alternative for oxygen removal from the culture medium, its absence in our lab hindered its implementation. Therefore, for future research endeavors, exploring alternative approaches or acquiring necessary equipment like a desiccator could be beneficial.

The use of glue to connect the fluidic ports brought up a lot of chances of failure by accidental glue entering and blocking the fluidic channels. As well as difficult assembly with very small parts and impractical handling especially with the liquid port, a small 0.5 cm piece of PEEK tubing. This is very unstable and easily placed incorrectly on the glue, especially by manual placement and straight holding. Therefore, a better tube-chip connection should be thought of like the Micronit clamping system, where tubing can be pushed into the glass chip by deforming a ferrule to seal the connection effectively. This also allows for disconnecting the tubing easily from the

microfluidic device. This can be more practical when moving the system and for the use of different tubing lengths. This Micronit chip resealable system also allows for replacing for instance the membrane layer once it is clogged with for instance proteins present in the culture medium.

Since the system was not able to be tested at different gas compositions, a different gas mixing system with MFCs with a lower minimal gas flow rate should be introduced.

Additionally, it would have been preferable to utilize a COMSOL model that integrates membrane deformation directly into the diffusion model, rather than handling it as a separate aspect. Integrating membrane deformation into the model would allow for a more straightforward consideration of its effects on flow velocities in the channels, diffusion, and the outcomes of flow rate adjustments. This approach could also reduce computational time for large sensitivity analyses, as the current diffusion model alone requires nearly 2 hours to compute.

4.4. Validity and Reliability

The system has valid research and was able to measure air saturation in the liquid, but it did not happen on a reliable, consistent base. Because of too much variability in oxygen leaks as visible in results from Experiment 1 and Experiment 2.

The integration of the sensor spot into the gas exchanger lacks separate calibration, relying instead on the calibration of a 5 mm sensor spot from the same company with identical calibration parameters. While this approach may compromise the reliability of the sensor data, the primary focus of this prototype is on understanding the general kinetics of the gas exchanger response rather than achieving pinpoint accuracy. Moreover, the decision to use a 2 mm sensor spot presents challenges in obtaining adequate signal amplitudes, as the smaller size increases the likelihood of misalignment or displacement of the optical fiber, which also has a 2 mm tip. In contrast, the 5 mm sensor spot consistently yields higher signal amplitudes during calibration and deoxygenation in the beaker glass, meeting the threshold for reliable results set by Presens Precision Sensing GmbH. This highlights the importance of signal amplitude and underscores the need for careful consideration when selecting sensor spot sizes to ensure reliable and accurate data collection.

Besides that, the temperature is not measured in the system, while the sensor data is linked to a specific set temperature which is chosen by the operator based on an average of the temperature from the temperature probe just before filling the syringe and the temperature value on a thermometer in the lab, which shows fluctuating values over time. Besides, the gas flow from the gas tank could influence the temperature as well in the gas exchanger. This temperature incorrectness is likely to cause some errors in the data.

The syringe is flangeless, meaning it is challenging to fit the syringe tightly in the syringe pump, therefore the flange on the end of the plunger is used to somewhat clamp it to the syringe pump's moving part. Therefore the constant movement of the stepper motor might not be as constant as the movement of the plunger, because the plunger could slip loose, potentially causing fluctuations or variations in the flow rate. Luckily, the liquid

exiting the system can be monitored and continuously checked if no flow is happening. It would be beneficial to use a flanged syringe and add a flow meter after the Micronit chip to guarantee flow stability in the system. A flow meter measuring the gas flow rate would also be beneficial since the hydraulic resistance of the gas exchanger may have caused back pressure on the gas supply and influenced gas flow stability.

Besides that, the gas exchanger oxygen regulation experiment is only performed once due to time constraints. This gives a lack of reliability of the results and the gas exchanger working. The other results are also only performed once or twice maximal. This is not enough to draw strong conclusions, nor to compare it quantitatively to the COMSOL simulation.

The fabrication process is susceptible to human error and operational inconsistencies, particularly when utilizing the laser system. Additionally, the effectiveness of the BOFA fume extraction system significantly impacts the fabrication outcomes. Despite efforts to optimize the Keyence microscope for 3D surface characterization, challenges persist due to the inherent reflectivity and transparency of the glass substrate. Despite fine-tuning and attempts to enhance contrast through marking, achieving satisfactory results remains elusive. Moreover, irregularities in the Keyence microscope bed, such as scratches, contribute to the generation of spurious peaks and interfere with the accuracy of the results. Addressing these issues by employing an ultra-smooth, flat, and opaque stage bed could improve outcomes and enhance the reliability of the characterization process. Additionally, applying a thin layer of gold sputtering to the top side of the glass substrate could enhance contrast, further improving the characterization process. Additionally, it is essential to analyze the surface profile and surface roughness of the samples at multiple locations to draw robust conclusions and avoid basing assessments solely on a small, localized area of the channel.

5. Conclusions

In this project, a glass microfluidic chip fabrication method is established using Fs laser ablation. With this fabrication technique, this study explored three key avenues: sensor integration, gas exchanger fabrication, and testing. Our investigation into Fs laser ablation for micromachining a microfluidic gas exchanger unveiled promising prospects. Following parameter optimization, valuable insights are gained, paving the way for further research on Fs laser fabrication. This method demonstrated the feasibility of creating intricate structures and channels with $\pm(S_a= 12.2\,\mu m$ and $S_z=117.5\mu m$, along with through holes suitable for fluidic ports, with perimeter cutting being the preferred method. Furthermore, our successful sensor integration further underscores the potential of this fabrication technique.

However, it is essential to note that dimensions need to be increased by 10-20% to account for dimensional losses incurred during Fs laser fabrication. Despite the promising aspects, our endeavors have also encountered challenges, including time-consuming fabrication processes and obstacles caused by debris clogging.

Overall, while Fs laser ablation holds significant promise for microfluidic applications, our findings highlight the need for further optimization and refinement to overcome existing challenges and fully leverage its potential in this field.

Conclusively, our fabrication and assembly approach successfully yielded a functional gas exchanger prototype capable of facilitating gas and liquid flow without leakages or cross-contamination. However, the issue of unwanted gas permeation through connectors significantly impacted the reliability of our results, highlighting the need for tighter fittings.

Moreover, our study achieved successful sensor integration in a minimally invasive manner using Fs laser technology, underscoring its potential for broader research applications.

Looking forward, there is a clear need for further investigation into the application of Fs laser fabrication in microfluidics, tackling issues surrounding undesired gas permeation through connectors, and advancing the progress of microfluidic gas exchanger systems for OoC applications. Additional experiments are imperative to bolster the validity of our findings and ensure the reliability of the results.

Future research endeavors should include testing the system under conditions mimicking physiological settings, such as at 37°C without bubbles, and with the integration of cells into a genuine OoC system. These experiments offer an opportunity to refine connector designs to minimize gas permeation, undertake comparative analyses with alternative fabrication techniques, and explore innovative approaches for gas exchanger design and integration.

References

Driver, Rishab and Mishra, and Shweta, "Organ-on-a-chip technology: an in-depth review of recent advancements and future of whole body-on-chip," *BioChip Journal*, vol. 17, pp. 1–23, 2023.

Sedat Dogru, Bekir Aksoy, Halil Bayraktar, and B. Erdem Alaca, "Poisson's ratio of PDMS thin films," *Polymer Testing*, vol. 69, pp. 375–384, 2018.

Place, Trenton L and Domann, Frederick E and Case, Adam J, "Limitations of oxygen delivery to cells in culture: An underappreciated problem in basic and translational research", *Free Radical Biology and Medicine*, vol. 113, pp. 311–322, 2017.

Fujiwara, Mutsuko, Kentaro Takahashi, Mika Izuno, Ya Ru Duan, Maya Kazono, Fuminori Kimura, and Yoichi Noda, "Effect of micro-environment maintenance on embryo culture after in-vitro fertilization: comparison of top-load mini incubator and conventional front-load incubator," *Journal of assisted reproduction and genetics*, vol. 24, pp. 5–9, 2007.

Monson, Loxie, Sung In Moon, and CW Extrand, "Permeation resistance of poly (ether ether ketone) to hydrogen, nitrogen, and oxygen gases." *Journal of applied polymer science* 127.3 2013, 1637-1642.

McKeown, SR, "Defining normoxia, physoxia and hypoxia in tumours—implications for treatment response." *The British journal of radiology*, vol. 87, no. 1035, pp. 20130676, 2014.

Gangwar, Sudhanshu et al. "Quality analysis of material jetted silicone material for soft robotics application." *Materials Letters*, vol. 355, p 135566, 2024.

van Reeuwijk, Matthijs "Design of a miniature gas exchanger for oxygen control in microfluids: Design, integration, fabrication and validation of a miniature cell medium gas exchanger to control (sub) physiological oxygen concentrations on a liver chip" 2021).

Preedy, Emily et al. "Surface roughness mediated adhesion forces between borosilicate glass and gram-positive bacteria" *Langmuir*, vol. 30, nr. 31, p 9466-9476, 2014.

Zhang, Yu Shrike et al. "Multisensor-integrated organs-on-chips platform for automated and continual in situ monitoring of organoid behaviors" *Proceedings of the National Academy of Sciences*, vol. 114, nr. 12, p E2293–E2302, 2017.

Lin, K-C et al. "Airborne toxicological assessment: The potential of lung-on-a-chip as an alternative to animal testing" *Materials Today Advances*, vol. 14, p 100216, 2022.

Hamed, Hazem et al. "Applications, materials, and fabrication of micro glass parts and devices: An overview" *Materials Today*, 2023.

2. Self-reflection

Throughout this project, I have undergone significant growth and learning. Improving my communication skills, particularly in navigating the different goals of TUD, EMC, and Bronkhorst High Tech B.V., was a key aspect. While it took some time to understand everyone's needs, weekly meetings with my supervisors were invaluable in this process. Exploring various labs and using advanced equipment like the Lasea Laser system was also a highlight, providing hands-on learning experiences that were both challenging and rewarding.

The Fs laser fabrication part of the project took over half a year and it was challenging to get to know to ins and outs of this machine, especially since there were no recipes or earlier contributions from others that I could rely on. Discovering unforeseen factors such as the impact of fume extraction and fan blowing angles on the substrate, along with certain user interface issues highly susceptible to errors, such as the stage bed moving gradually with a slightly prolonged left-click rather than a single strong click to move it by a user-set increment. These hurdles often resulted in incomplete or inconclusive samples, necessitating additional time and effort to rectify and refine.

The laser was also very busily booked by others, and unfortunately only operational during office hours and not overnight, unlike a 3D printer. Maintenance periods in the building often restricted access to the laser lab. Additionally, while the laser typically operated at a 550 nm wavelength, some users required an 1100 nm wavelength, necessitating a change in laser optics for a few days before reverting to the regular setup. These factors significantly impeded progress, especially since the laser jobs could take several hours, even up to 6 hours, for high-quality centimeter-scale jobs.

These obstacles left me feeling frustrated and stressed. Handling this stress proved challenging, and at times, it overshadowed progress on my thesis. Stress took over my thesis on a lot of occasions. To cope better, I recognized the importance of sticking to a plan, prioritizing tasks, focusing on one thing at a time, and celebrating intermediate achievements. However, as patience isn't my strongest suit, I acknowledged the need to grow it.

Establishing and achieving tangible milestones distributed throughout the project timeline would help immensely. Unfortunately, progress often felt elusive, especially when the final month became a make-or-break scenario, and it took over a year to know if the gas exchanger worked or not. This hindered my motivation, but this has been a great proof of my perseverance and tested my patience a lot.

Moreover, numerous potential failures, such as device breakage, cracking during assembly, glue seepage, and operator errors, heightened my stress levels. The prospect of starting over if a failure occurred weighed heavily on me, contributing to a constant state of stress.

Reflecting on the project, I recognize the need for a balance between quality and efficiency to facilitate multiple iterations of the device. This would require adjustments in approach and a willingness to accept trade-offs to achieve greater overall progress.

Looking back, I realize I may have been overly ambitious in my approach. When I decided to develop a microfluidic system focusing mainly on the gas exchanger for oxygen regulation, I also aimed to conduct a real cell experiment at EMC. While conducting research into the biological background was beneficial, I should have prioritized starting with the gas exchanger and then assessed whether integrating the cell experiment aligned with my project timeline (which it ultimately did not).

I conducted extensive research and literature reviews, and my plans were too expansive, making them unfeasible, especially given the lengthy process of Fs laser fabrication. This lofty ambition compromised the thoroughness of testing and the ability to draw meaningful conclusions. In hindsight, I would have preferred to delve deeper into a smaller topic and conduct more thorough research. Additionally, I should have sought more assistance on this throughout the project's duration.

Looking back, I realize I have been a bit sloppy in my work. I could have been more organized and kept better records instead of just scribbling things down in my notebook. One example of this was when I was trying to optimize the settings for the Fs laser. I also forgot to check the real device under the Keyence microscope, which was a mistake because it meant I couldn't include accurate measurements and surface details in my report. This sloppiness also made writing my thesis harder because everything was scattered and hard to find in my notes and documents. In the future, I will make sure to be more organized from the start to avoid these kinds of mistakes. Early on, I only used a regular microscope and the LS-VIEW camera to check my results. I tried using SEM and WLI for better analysis, but they were not very practical. For example, the SEM was time-consuming and the sample had to be sacrificed, while WLI had trouble with characterizing narrow, deep cuts in the sample. Luckily, I found the Keyence digital microscope, which was much easier to use. But there were still challenges, like getting accurate results. Looking back, I should have taken more time to choose the best method and talked it over with my supervisors. Next time, I'll be sure to think more carefully about which methods to use and get advice from my supervisors.

In addition to the project, I initially served on the Taylor Board, the board of our study association. This commitment demanded approximately three days a week, posing challenges in balancing with my thesis. However, it proved to be a valuable lesson in time management. Furthermore, personal circumstances occasionally diverted my attention, as I was unexpectedly diagnosed with Obstructive Sleep Apnea Syndrome

(OSAS), which was emotionally unsettling. I have had trouble with sleep problems for my whole life, like sleepwalking, which made this diagnosis even harder on my mental health. Managing OSAS required treatment, including surgery and numerous hospital appointments, but fortunately, the condition has since been resolved. Such experiences occasionally hindered my ability to concentrate on my thesis.

I hope my contribution to the field helps, even though a small step, in the development of incubator-free OOCs and I sincerely hope the end goal of Human-on-chip will be reached.

I would like to express my sincere gratitude to my supervisors for their guidance and support throughout the project. I also appreciate the technical team for training me on equipment usage and providing assistance when needed.

A. Assembly images

This appendix provides images of the fabrication process.

Figure 16.: All chip layers in the ultrasonic bath
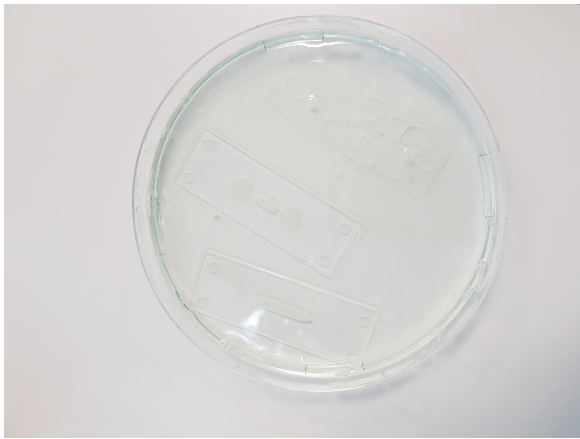
(a) Cleaning all chip layers with dishwasher soap and water
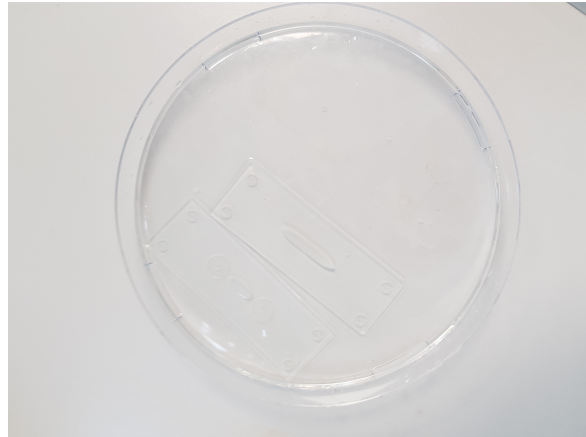
(b) Cleaning all chip layers with IPA

Figure 17.: Cleaning steps
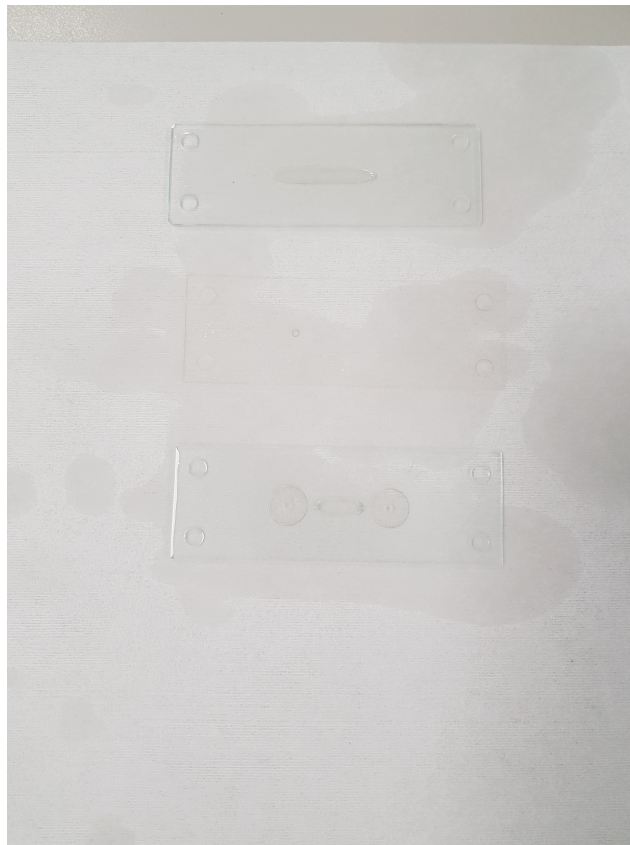
Figure 18.: Drying of all chip layers after cleaning
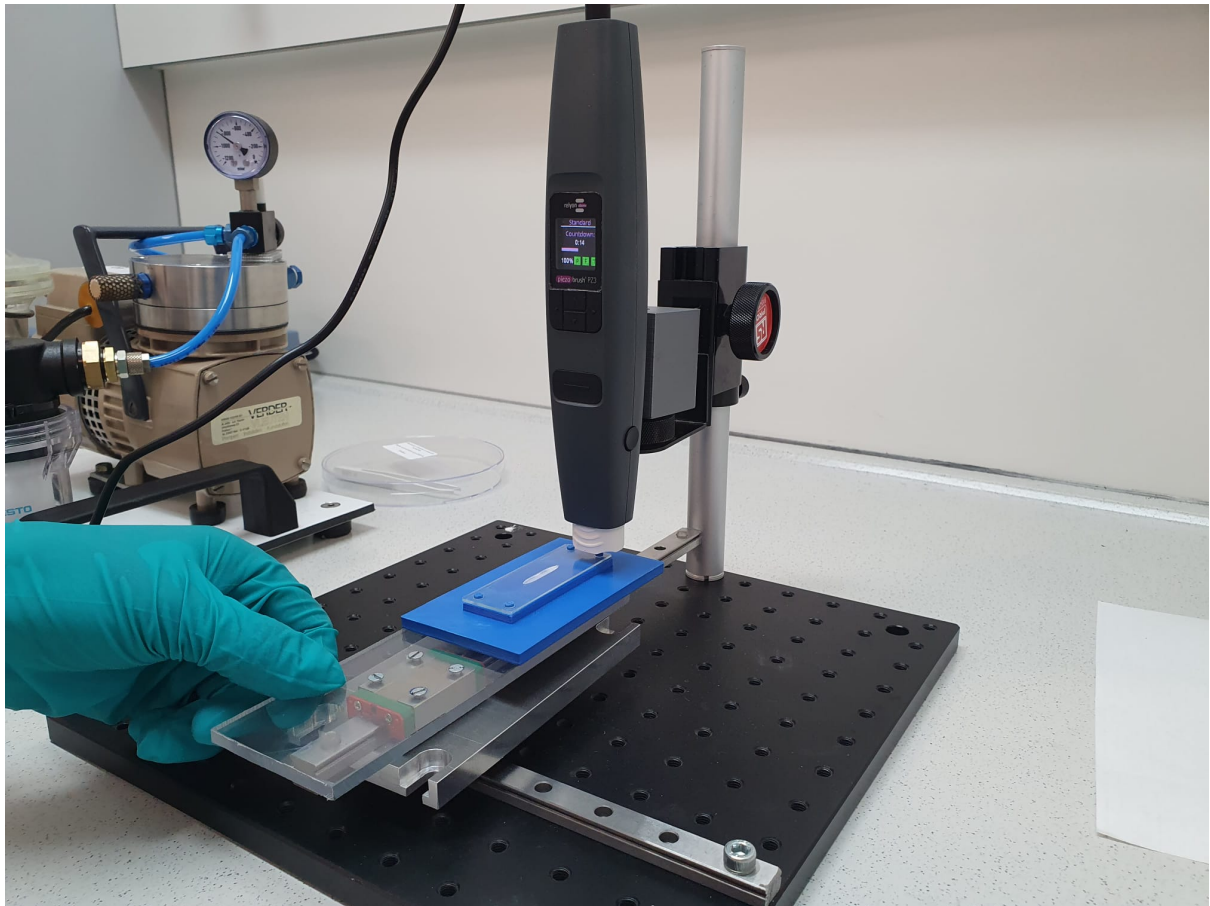
Figure 19.: Plasma treating of the microfluidic chip

Figure 20.: Heat treatment during compression

B. Additional images

This section shows some additional images for understanding some of the experimental arrangements.
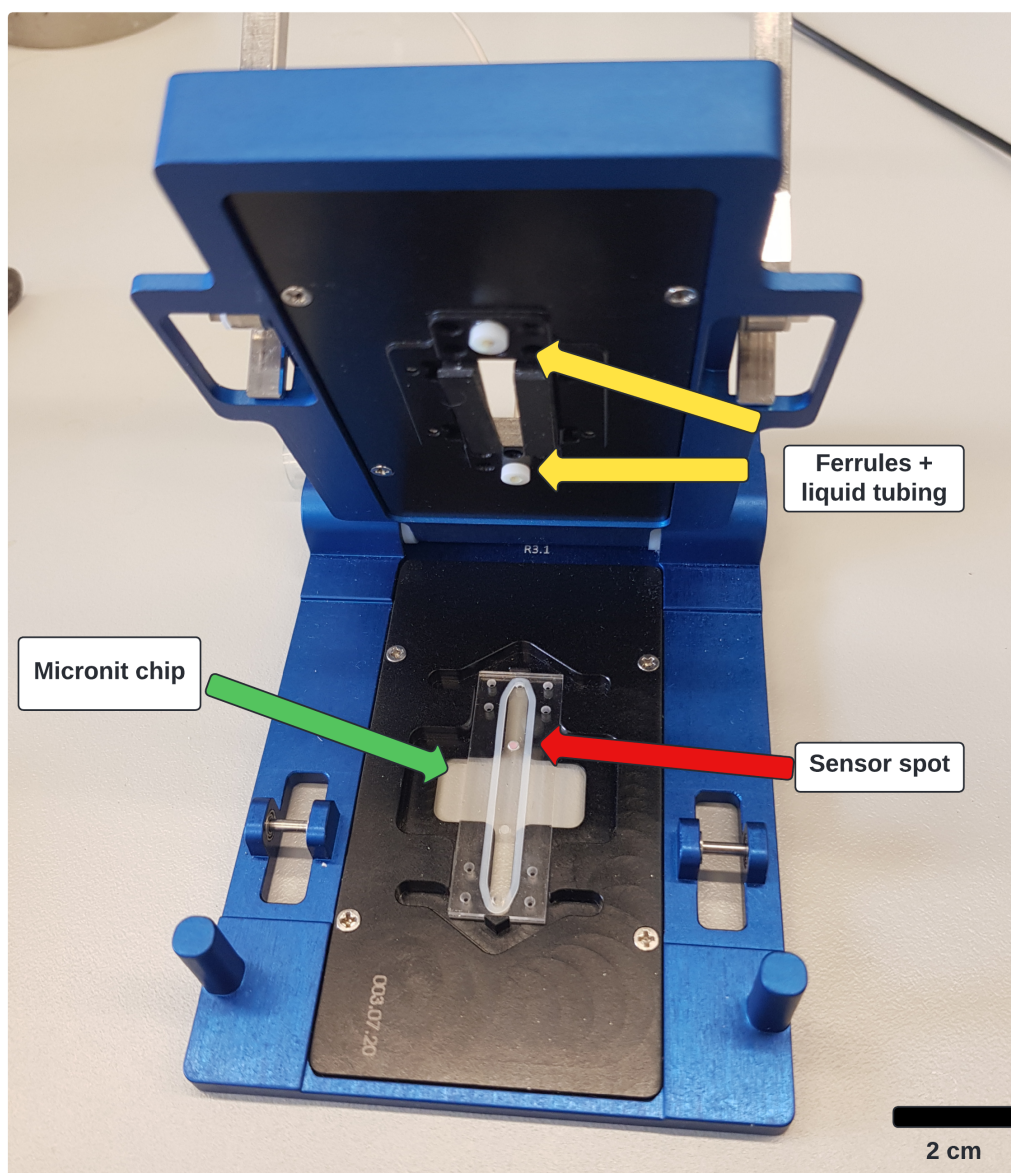
Figure 21.: Micronit Pro Holder clamp with Micronit chip and sesnor spot
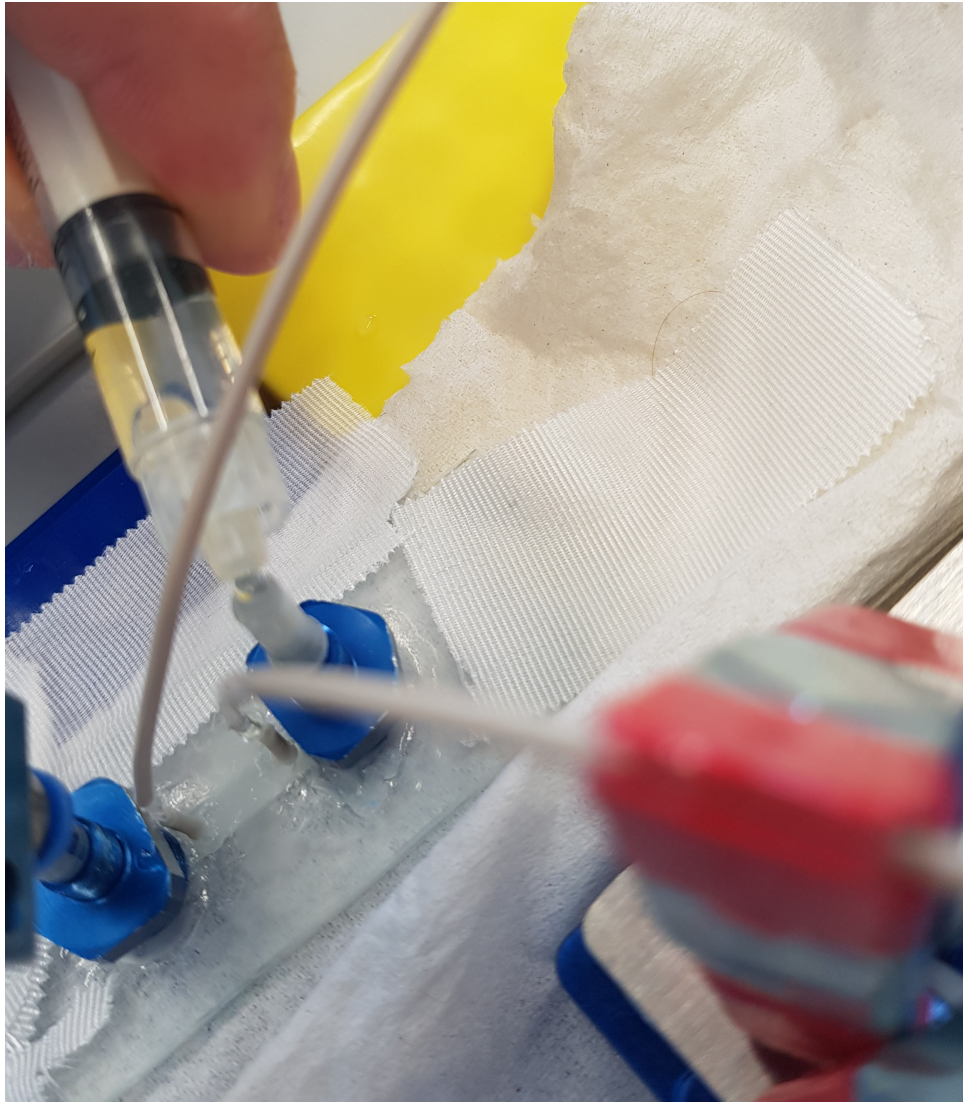
Figure 22.: Water drop placement for gas flow checking
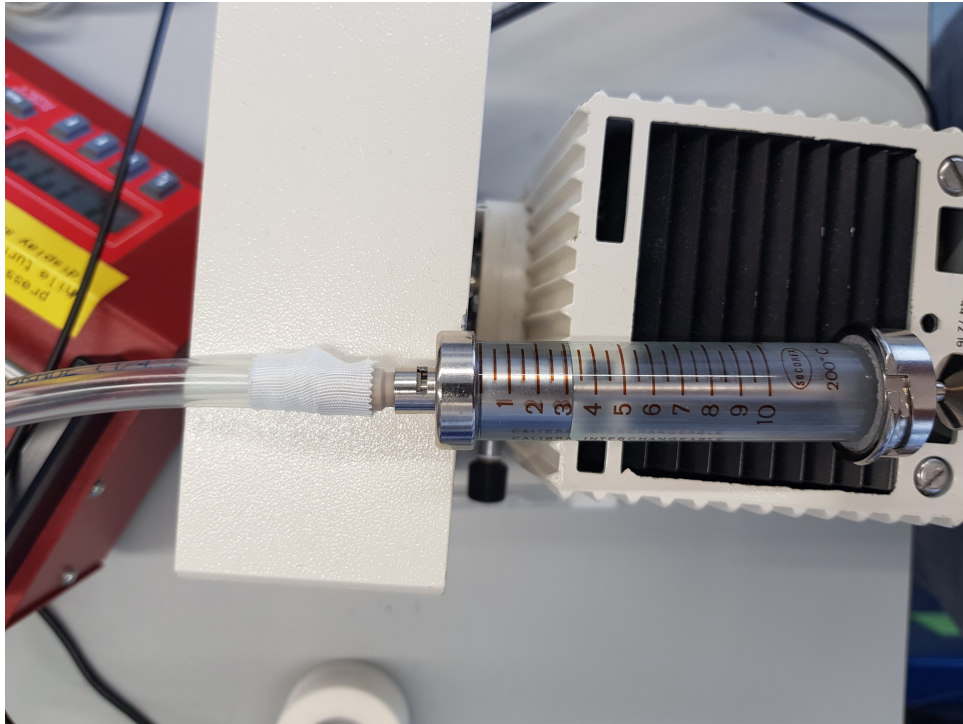
Figure 23.: N$_2$ filling of the gas-tight syringe by taping the syringe to the gas input tubing
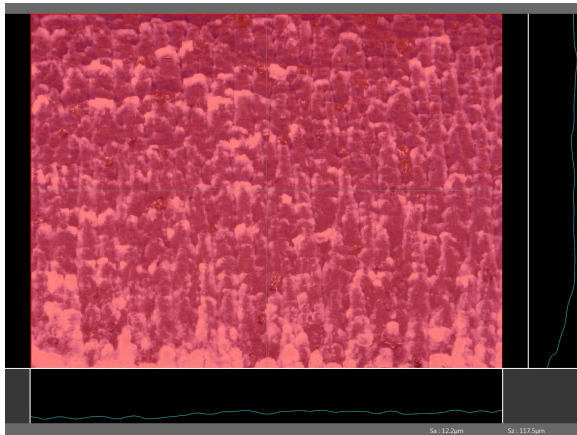
(a) Surface roughness of sample K2
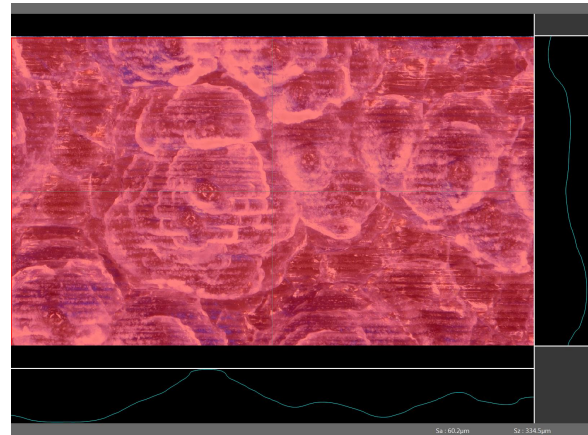
(b) Surface roughness of sample K3

Figure 25.: Surface roughness comparison
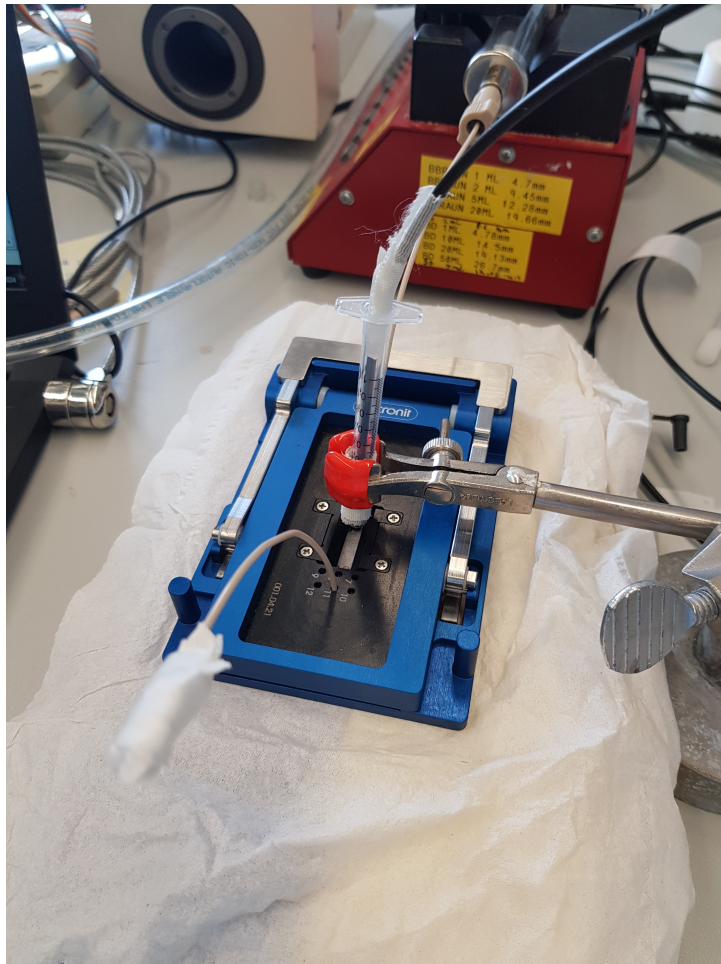
Figure 24.: Laboratory clamping system designed for aligning optical fibers to sensors during automated probing

C. Fabrication protocol

C.1. Standard laser fabrication steps

This appendix will demonstrate a step-by-step protocol for the operation of the laser system.

1. Clean the glass slide with IPA and dry it with paper.

2. Tape the glass slide onto the alumina plate.

3. Put the prepared slide into the laser system box.

4. Turn the suction on to keep the alumina plate in place.

5. Align the glass slide.

6. Find the top left corner for the origin setting by moving the x and y axes.

7. Focus on small carves/dust particles on the alumina plate.

8. Move the z-direction up with $z =$ height of the glass slide (1mm), so the focal point lies on the top of the glass slide.

9. Move to the location of interest on the glass slide (preferably the center of your drawing) and set this as the focus position for the laser system.

10. Add a manual drawing using the Kyla software or upload a DXF(Drawing Exchange Format) file into the software.

11. Set settings like power, repetitions, speed, hatching pattern, and hatch pitch accordingly.

12. Start the job.

13. After completion, brush off excess glass dust.

C.2. Assembly Steps

After all parts are fabricated accordingly, the assembly is the next part. This project made a sandwich stack assembly and glued connectors afterward, before connecting the right tubing to the right connection port

1. Clean all parts with dishwasher soap and warm water

2. Clean all parts in the ultrasonic bath (full-cycle, 3 minutes)

3. Clean all parts with IPA and dry them with paper

4. Put bottom glass slide on plasma gun stage, move stage height to ca. 0.5 cm distance between the glass slide and plasma gun tip, and turn on the plasma gun for 2x30sec. Move the stage so that the entire top surface of the glass slide gets exposed evenly

5. Move the bottom glass slide into the 3D-printed alignment tool

6. Repeat the plasma activation step for the PDMS sheet and carefully place this on top of the just activated bottom glass slide(NOTE: use tweezers to gradually drape the membrane starting from one side and placing it handy to remove all possible bubbles trapped between the layers, ensure bubble-free!!)

7. Put the 3D printed alignment tool with 2/3 layers stacked together under the plasma gun and repeat the plasma activation step for the other side of the PDMS membrane and the top glass slide and put the top glass slide on top of the other layers using the alignment tool.

8. Place the 3D alignment tool including the complete stack between two scrap metal blocks, but place something soft in between to prevent excessive pressure and scratches on the glass device

9. Place the system in the oven at 65 degrees Celcius for 5 hours

10. Use oven mitts to carefully take out the system and let it cool off

11. Place a connector in the right alignment hole and carefully but generously glue around the connector, making sure not to block any channels with glue

12. Keep holding the connector until the glue has cured enough to stand on its own, do not touch it for 2 hours to let it fully cure

13. repeat for the other connectors

14. Glue the needle gauge's interior into the microfluidic tubing and connect the right tubing to the right connection port

C.3. Safety Precautions

When conducting the fabrication process for microfluidic devices, it is essential to prioritize safety at all times. The following safety precautions should be observed:

- Wear appropriate personal protective equipment (PPE), including safety goggles, gloves, and laboratory coats, at all times to protect against potential hazards.

- Use gloves and goggles when handling superglue to prevent skin contact and eye irritation.

- Use isopropanol alcohol (IPA) in a well-ventilated area or under a fume hood to minimize inhalation exposure and avoid direct skin contact.

- When operating the plasma gun, ensure proper ventilation by using a fume hood to extract hazardous fumes, such as ozone, away from the work area.

- Avoid plasma exposure close to electrically conductive materials, like screws in the stage bed, since this can lead to electric discharge

- Familiarize yourself with the safety guidelines and operating procedures for all equipment and materials used in the fabrication process.

- Exercise caution when handling sharp objects or working with high-temperature equipment, such as plasma guns or ovens.

- Avoid direct exposure to laser beams and follow all safety protocols provided by the laser system manufacturer.

- In case of emergencies, such as chemical spills or equipment malfunction, know the location of emergency exits, eyewash stations, and fire extinguishers, and follow established emergency procedures.

- Regularly inspect equipment for any signs of damage or wear and report any concerns to the appropriate personnel.

- Educate yourself and others involved in the fabrication process on potential hazards and safe practices to minimize the risk of accidents or injuries.

C.4. Cleaning protocol before quality inspection

Before the quality inspection, the same cleaning steps are used as the first three steps in the assembly protocol.

1. Clean all parts with dishwasher soap and warm water

2. Clean all parts in the ultrasonic bath (full-cycle, 3 minutes)

3. Clean all parts with IPA and dry them with paper

D. List of Materials

List of functional components in the system

- Syringe pump, World Precision Instruments AL-1000

- Glass gas-tight syringe, Socorex, 10mL

- Microscope slides with ground edges Pack of 50x, VWR, HECH42401010

- PEEK microfluidic tubing 0.25 mm ID and 1/16 " OD, Micronit B.V.

- Aluminium reducing nipple, FESTO

- Pneumatic manual control valve, FESTO

- General Purpose Dispense Tips Yellow 32G, Nordson Precision Tips

- Sensor spot 5 mm and 2 mm, PreSens Precision Sensing GmbH, PSP-PSt3-NAU-D5-YOP and PSP-PSt3-NAU-D2-YOP respectively.

- Fibox 3, PreSens Precision Sensing GmbH

- Polymer optical fiber with SMA connector, PreSens Precision Sensing GmbH

- Temperature sensor Pt100, PreSens Precision Sensing GmbH

- Resealable flow cell straight shape - topconnect (pack of 6), Micronit B.V.

- Chip holder fluidic connect pro – topconnect (subtype: resealable), Micronit B.V.

- PDMS sheet 170 μm thickness, unknown source, provided by supervisor

- Syringe to tube connection kit, Micronit B.V.

- Fluidic Connect Pro PEEK connection kit, Micronit B.V.

- Silicone glue, Wacker Elastosil E43

- Keyence digital microscope VHX-6000

- Lasea LS-Lab

- Piezo brush PZ3, Relyon Plasma GmbH

- Super Glue 3, Loctite

E. MATLAB

E.1. Flow and membrane deformation calculations

The Hagen-Poiseuille equation is utilized for determining pressure drop over a laminar flow channel. Given that the entire flow system operates under laminar conditions, this equation is deemed applicable. It facilitates the calculation of absolute pressure at any point in the system.

By applying this equation to both the gas and liquid channels of the gas exchanger, located on either side of the membrane, the absolute pressure difference across the membrane is computed.

The liquid system, starting from the gas exchanger liquid channel onward, comprises the liquid channel, needle gauge, tubing, Micronit channel, and additional tubing. By summing their pressure drops, along with atmospheric pressure from the open outlet, the pressure drop over the gas exchanger liquid channel is calculated. Accounting for minor losses from sudden contractions and expansions in the flow path, particularly at the gas exchanger-to-tubing connection made by a needle gauge with a smaller inner diameter, ensures a comprehensive assessment.

Similarly, the gas system includes the gas exchanger gas channel, gas tubing, and atmospheric pressure from the open end. For the membrane deformation, three scenarios are compared: both gas and liquid flow into the gas exchanger, only liquid flow, and only gas flow. The Hagen-Poussuielle equation is:

$$\Delta P_{\text{circ}} = \frac{8\eta L Q}{\pi r^4} \quad \text{for circular channel}$$
$$\Delta P_{\text{rect}} = \frac{12\eta L Q}{wt^3} \quad \text{for rectangular channel}$$

(E.1)

Where ΔP represents the pressure drop (in Pa), η denotes the dynamic viscosity (in Pa·s), L represents the characteristic length (in meters), Q signifies the fluid flow rate (in m^3/s), r denotes the channel radius (in meters), w the channel width (in meters), and t the channel height (in meters).

Minor losses using K-values are used for the sudden expansion and the sudden contraction between the tubing and the needle gauge's interior metal tubing. K-values were retrieved from [21].

Atmospheric pressure of 10^5 Pa is used as exit pressure at both the gas and the liquid exit. The largest pressure drop over the membrane = 229 Pa during gas and liquid flow and only liquid flow.

The calculations can be found in the following MATLAB script.

```
%%
%Pressure difference across membrane
%Parameters
eta_l=1.002e-3; % Dynamic viscosity liquid at 20degC [Pa*s]
eta_g=18.37e-6 ;% Dynamic viscosity gas at 20degC [Pa*s]
Q_g=5e-6/60; % Gas flow rate [m^3/s]
Q_l=35e-9/(60); %Liquid flow rate provided by syringe pump [m^3/s]
rho_l=1091; % Density of medium/water at 20degC [kg/m^3]
rho_g=1.314; % Density of (nitrogen/oxygen) gas at 20 degC [kg/m^3]
D_o2=2.0e-9 ; % Diffusion coefficient oxygen in water at 20 degC [m
    ^2/s]


%Dimensions
x_l=300e-6;% liquid channel height [m]
b_l=4e-3;% liquid channel width [m]
b_g=4e-3;% Gas channel width [m]
x_g=500e-6;% Gas channel height [m]
L_l=1e-2; %Length liquid channel [m]
L_g=2.53e-2; %Length gas channel [m]
L_m=40e-3; % Micronit chip length [m]
x_m=0.3e-3;% Micronit chip height [m]
b_m=3.4e-3; %Micronit chip width [m]
L_t=0.2 ; %tubing length from GE to Micronit chip + from Micronit
    chip to waste [m]
L_gt=0.1; %tubing from gas exchanger to ambient air
L_needlegauge=1e-2; %Needle gauge length [m]
D_t=0.25e-3;% liquid tubing inner diameter [m]
D_s=0.1e-3; % needle gauge inner diameter [m]
D_gt=3e-3;% %gas tubing inner diameter [m]
D_l=(2*x_l*b_l/(x_l+b_l)); %hydraulic diameter liquid channel [m]
D_g=(2*x_g*b_g/(x_g+b_g)); %hydraulic diameter gas channel [m]
%Others:
v_l=Q_l/(b_l*x_l); % flow velocity in gas exchanger liquid channel [
    m/s]
v_g=Q_g/(b_g*x_g); % flow velocity in gas exchanger gas channel [m/
    s]
V_needlegauge=Q_l/(0.25*pi*D_s^2); % flow velocity in needle gauge [
    m/s]
V_t=Q_l/(0.25*pi*D_t^2); % flow velocity in liquid tubing [m/s]
V_gt=Q_g/(0.25*pi*D_gt^2); % flow velocity in gas tubing [m/s]
%Dimensionless numbers in gas exchanger channels
Pe_l=v_l*x_l/D_o2 ; %Peclet number liquid in gas exchanger
```

```
Re_l=(v_l*rho_l*D_l)/(eta_l); %Reynolds number in liquid channel
Re_g=(v_g*rho_g*D_g)/(eta_g); %Reynolds number in gas channel

%Hydraulic resistances:
Rh_l=(12*eta_l*L_l)/(x_l^3*b_l)/(1-0.63*(x_l/b_l)); %gas exchanger
    liquid channel hydraulic resistance
Rh_g=(12*eta_g*L_g)/(x_g^3*b_g)/(1-0.63*(x_g/b_g)); % gas exchanger
    gas channel hydraulic resistanceDf

%Minor losses K-values
K_exp=1-(D_s^2/D_t^2);% Sudden expansion K-value minor losses
K_con=0.42*(1-(D_s^2/D_t^2)); % Sudden contraction K-value according
    to https://engineerexcel.com/loss-coefficient-for-sudden-
    contraction/

% Pressure drops
DeltaPliqchannel=12*Q_l*eta_l*L_l/(x_l^3*b_l); %liq channel deltaP
DeltaPgaschannel=12*Q_g*eta_g*L_g/(x_g^3*b_g); %gas channel deltaP
DeltaPmicronit=12*eta_l*Q_l*(L_m)/(x_m^3*b_m); %Pressure drop over
    liquid channel Micronitchip [Pa]
DeltaPneedlegauge=8*eta_l*Q_l*(L_needlegauge)/(pi*D_s^4); %Pressure
    drop over needle gauge [Pa]
DeltaPneedlegaugeedge1=rho_l*(K_con)*V_needlegauge^2/2; %Pressure
    drop over needle gauge contraction with K-value according to
    https://engineerexcel.com/loss-coefficient-for-sudden-contraction
    /
DeltaPneedlegaugeedge2=rho_l*(K_exp)*V_t^2/2; %Pressure drop over
    needle gauge expansion with K-value according to https://
    engineerexcel.com/loss-coefficient-for-sudden-contraction/
DeltaPtubingafterGE=8*eta_l*Q_l*(L_t)/(pi*D_t^4); %Pressure drop
    over liquid tubing [Pa]
DeltaPgastubingafterGE=8*eta_l*Q_g*(L_gt)/(pi*D_gt^4);%Pressure drop
    over gas tubing [Pa]
DeltaPliqtot=DeltaPtubingafterGE+DeltaPmicronit+DeltaPneedlegauge+
    DeltaPneedlegaugeedge1+DeltaPneedlegaugeedge2+1e5+
    DeltaPliqchannel; %Total liquid pressure drop from gas exchanger
    inlet to waste [Pa]
DeltaPgastot=1e5+DeltaPgaschannel+DeltaPgastubingafterGE; %Total gas
    pressure drop from gas inlet to ambient air [Pa]
DeltaPmembrane=DeltaPliqtot-DeltaPgastot;%Pressure difference across
    membrane [Pa]
DeltaPmembranewithoutgasflow=DeltaPliqtot-1e5;
DeltaPmembranewithoutliqflow=DeltaPgastot-1e5;
```

E.2. Delay time for gas flow change influence from gas exchanger to Micronit chip

Using the dimensions of each flow component between the gas exchanger inlet and the sensor spot located in the Micronit chip, we can determine the additional time after the new gas concentration is added to when it is detected by the sensor spot. The gas flow starts in a wider tubing and then is reduced to a smaller diameter tubing. The liquid path is from the gas exchanger to the location of the sensor spot in the Micronit chip. The calculated delay before noticing a change in the oxygen concentration using the sensor spot after changing the gas supply is 77 seconds.

Listing E.1: Experiment 1 optical sensor data visualization

```
Q_l=35e-9/(60); %Liquid flow rate provided by syringe pump
    ↪ [m^3/s]
Q_g=40e-6/60;% Gas flow rate provided by Bronkhorst OEM gas
    ↪ supply [m^3/s]
%Dimensions
x_l=300e-6;% liquid channel height [m]
b_l=4e-3;% liquid channel width [m]
L_l=1e-2; %Length liquid channel [m]
L_m=0.5e-2; % Micronit chip length from inlet to sensor spot [m]
x_m=0.3e-3;% Micronit chip height [m]
b_m=3.4e-3; %Micronit chip width [m]
L_t=0.2 ; %tubing length from syringe to gas exchanger to
    ↪ Micronit chip [m]
D_gsource=0.635e-2;% gas source tubing ID [m]
L_needlegauge=1e-2; %Needle gauge length [m]
D_t=0.25e-3;% liquid tubing inner diameter [m]
D_s=0.1e-3; % needle gauge inner diameter [m]
D_gt=3e-3;% %gas tubing inner diameter [m]
L_gsource=0.3; %gas source tubing length [m]
L_gt=0.1 ; %gas tubing length [m]
%Others:
V_gt=Q_g/(pi*0.5*D_gt^2); %gas tubing velocity [m/s]
V_gsource=Q_g/(pi*D_gsource^2*0.5); %gas source tubing velocity
    ↪ [m/s]
v_l=Q_l/(b_l*x_l); % flow velocity in gas exchanger liquid
    ↪ channel [m/s]
V_needlegauge=Q_l/(0.25*pi*D_s^2); %liquid flow velocity in
    ↪ needle gauge [m/s]
V_t=Q_l/(0.25*pi*D_t^2); % flow velocity in liquid tubing [m/s]
V_m=Q_l/(x_m*b_m); % liquid flow velocity Micronit chip [m/s]
t_tubing=L_t/V_t; % liquid tubing flow time [s]
t_g=L_gt/V_gt +L_gsource/V_gsource;% time needed for gas flow [s]
t_needlegauge=L_needlegauge/V_needlegauge ; % needle gauge flow
    ↪ time [s]
```

```
t_gasexchanger=L_l/v_l;% gas exchanger liquid flow time [s]
t_micronit= L_m/V_m; %liquid flow time Micronit chip section
    ↪ from inlet to sensor spot [s]
t_tot=t_tubing+t_needlegauge*2+t_gasexchanger+t_micronit+t_g;%total
    ↪ time needed
```

E.3. Oxygen sensing data processing

These scripts demonstrate the processing of oxygen sensor data through graphical representation. The raw data from the oxygen sensor is not included in this document due to its extensive and detailed nature. However, it is available upon request. Interested readers can obtain the data by contacting the author via email at jelle.hs@gmail.com. Consistency is maintained across all experiments by setting the same axis bounds, enhancing the clarity of their behavior and kinetics. Initially, the raw data from the Presens sensor text file is imported into the MATLAB environment. Distinct flow rate segments are differentiated by applying specific color codes to corresponding time intervals. These color-coded segments are clearly labeled in the legend for easy interpretation. The axes are labeled with time in minutes and air saturation in percentage to provide a clear understanding of the data. In Experiments 1 and 2, where the gas exchanger is absent, the slope is estimated through linear regression. The same time interval between the data points along the line's x-axis is utilized for both experiments to ensure equal estimation accuracy.

Listing E.2: Experiment 1 optical sensor data visualization

```
% Step 1: Load the data from the text file
filename = 'C:\Users\koenz\OneDrive\Documenten\Thesis␣
    ↪ Jelle\Presens\waterflow22aprilwithoutbs.txt';
fid = fopen(filename, 'r');
data = textscan(fid, '%*s␣%*s␣%f␣%f␣%*f␣%f␣%*f␣%*s',
    ↪ 'Delimiter', ';');
fclose(fid);

% Step 2: Extract the desired columns
time = data{1}; % Extract time values
air_saturation = data{2}; % Extract air saturation values

% Step 3: Define time intervals corresponding to different flow
    ↪ rates
flow_rate_35_1 = time >= 1 & time <= 22; % Time interval for
    ↪ flow rate 35 ul/min (adjusted start time to t=1 min)
```

```matlab
flow_rate_0 = time > 22 & time <= 42; % Time interval for flow
    ↪ rate 0 ul/min
flow_rate_35_2 = time > 42 & time <= 66; % Time interval for
    ↪ flow rate 35 ul/min
flow_rate_70 = time > 66 & time <= 77; % Time interval for flow
    ↪ rate 70 ul/min
flow_rate_105 = time > 77 & time <= 86; % Time interval for flow
    ↪ rate 105 ul/min
flow_rate_140 = time > 86 & time <= 95; % Time interval for flow
    ↪ rate 140 ul/min
flow_rate_175 = time > 95 & time <= 100.849; % Time interval for
    ↪ flow rate 175 ul/min

% Step 4: Plot the data with different colors for each flow rate
    ↪ section
figure;
hold on; % Overlay multiple plots
p1 = plot(time(flow_rate_35_1), air_saturation(flow_rate_35_1),
    ↪ 'b.-'); % Plot data for flow rate 35 ul/min in blue
p2 = plot(time(flow_rate_0), air_saturation(flow_rate_0),
    ↪ 'r.-'); % Plot data for flow rate 0 ul/min in red
p3 = plot(time(flow_rate_35_2), air_saturation(flow_rate_35_2),
    ↪ 'b.-'); % Plot data for flow rate 35 ul/min in blue (same
    ↪ color as first section)
p4 = plot(time(flow_rate_70), air_saturation(flow_rate_70),
    ↪ 'm.-'); % Plot data for flow rate 70 ul/min in magenta
p5 = plot(time(flow_rate_105), air_saturation(flow_rate_105),
    ↪ 'c.-'); % Plot data for flow rate 105 ul/min in cyan
p6 = plot(time(flow_rate_140), air_saturation(flow_rate_140),
    ↪ 'y.-'); % Plot data for flow rate 140 ul/min in yellow
p7 = plot(time(flow_rate_175), air_saturation(flow_rate_175),
    ↪ 'k.-'); % Plot data for flow rate 175 ul/min in black
xlabel('Measurement␣Time␣(min)');
ylabel('Air␣Saturation␣(%)');
title('Oxygen␣measurement␣with␣water␣flow␣experiment␣1');
xlim([0, 180]); % Set x-axis limit to 180 minutes
ylim([0, 160]);  % Set y-axis limit to 160 minutes
grid on;

% Step 6: Add the slope line and calculate its slope
x1 = 22.674;
y1 = 11.855;
x2 = 35.02;
y2 = 46.258;

% Draw the slope line passing through the points
```

```matlab
Line1 = line([x1, x2], [y1, y2], 'Color', 'green', 'LineStyle',
    ↪ '--', 'LineWidth', 1.5);

% Calculate slope
slope = (y2 - y1) / (x2 - x1);
fprintf('Estimated␣slope:␣%.2f\n', slope);

% Convert slope to string
slope_str = num2str(slope);

% Add legend
legend([p1 p2 p3 p4 p5 p6 p7 Line1], ...
    'Flow␣Rate␣35␣ul/min␣(t=1␣to␣t=22)', ...
    'Flow␣Rate␣0␣ul/min␣(t=22␣to␣t=42)', ...
    'Flow␣Rate␣35␣ul/min␣(t=42␣to␣t=66)', ...
    'Flow␣Rate␣70␣ul/min␣(t=66␣to␣t=77)', ...
    'Flow␣Rate␣105␣ul/min␣(t=77␣to␣t=86)', ...
    'Flow␣Rate␣140␣ul/min␣(t=86␣to␣t=95)', ...
    'Flow␣Rate␣175␣ul/min␣(t=95␣to␣t=100.849)', ...
    ['Slope␣Estimation␣=␣', slope_str, '␣%/min.']);
```

Listing E.3: Experiment 2 optical sensor data visualization

```matlab
% Step 1: Load the data from the text file
filename = 'C:\Users\koenz\OneDrive\Documenten\Thesis
    ↪ Jelle\Presens\waterflow22apriltest2withoutbs.txt';
fid = fopen(filename, 'r');
data = textscan(fid, '%*s %*s %f %f %*f %*f %*f %*s',
    ↪ 'Delimiter', ';');
fclose(fid);

% Step 2: Extract the desired columns
time = data{1}; % Extract time values
air_saturation = data{2}; % Extract air saturation values

% Step 3: Define time intervals corresponding to different flow
    ↪ rates
flow_rate_35_1 = time >= 9 & time <= 42; % Time interval for
    ↪ flow rate 35 ul/min
flow_rate_70 = time > 42 & time <= 53; % Time interval for flow
    ↪ rate 70 ul/min
flow_rate_105 = time > 53 & time <= 60; % Time interval for flow
    ↪ rate 105 ul/min
flow_rate_140 = time > 60 & time <= 72; % Time interval for flow
    ↪ rate 140 ul/min
flow_rate_175 = time > 72 & time <= 78; % Time interval for flow
    ↪ rate 175 ul/min
flow_rate_0 = time > 78 & time <= 92; % Time interval for flow
    ↪ rate 0 ul/min
flow_rate_35_2 = time > 92 & time <= 115.354; % Time interval
    ↪ for flow rate 35 ul/min

% Step 4: Plot the data with consistent colors for each flow
    ↪ rate section
figure;
hold on; % Overlay multiple plots
p1 = plot(time(flow_rate_35_1), air_saturation(flow_rate_35_1),
    ↪ 'b.-'); % Plot data for flow rate 35 ul/min in blue
p2 = plot(time(flow_rate_70), air_saturation(flow_rate_70),
    ↪ 'm.-'); % Plot data for flow rate 70 ul/min in red
p3 = plot(time(flow_rate_105), air_saturation(flow_rate_105),
    ↪ 'c.-'); % Plot data for flow rate 105 ul/min in green
p4 = plot(time(flow_rate_140), air_saturation(flow_rate_140),
    ↪ 'y.-'); % Plot data for flow rate 140 ul/min in magenta
p5 = plot(time(flow_rate_175), air_saturation(flow_rate_175),
```

```matlab
    ↪ 'k.-'); % Plot data for flow rate 175 ul/min in cyan
p6 = plot(time(flow_rate_0), air_saturation(flow_rate_0),
    ↪ 'r.-'); % Plot data for flow rate 0 ul/min in yellow
p7 = plot(time(flow_rate_35_2), air_saturation(flow_rate_35_2),
    ↪ 'b.-'); % Plot data for flow rate 35 ul/min in blue (same
    ↪ color as first section)

xlabel('Measurement␣Time␣(min)');
ylabel('Air␣Saturation␣(%)');
title('Oxygen␣measurement␣with␣water␣flow␣experiment␣2');
xlim([0, 180]); % Set x-axis limit to 180 minutes
ylim([0, 160]);  % Set y-axis limit to 160 minutes
grid on;


% Add the slope line and calculate its slope
x1 = 79.346;
y1 = 1.373;
x2 = 91.849;
y2 = 17.805;

% Draw the slope line passing through the points
Line1 = line([x1, x2], [y1, y2], 'Color', 'green', 'LineStyle',
    ↪ '--', 'LineWidth', 1.5);

% Calculate slope
slope = (y2 - y1) / (x2 - x1);
fprintf('Estimated␣slope:␣%.2f\n', slope);

% Convert slope to string
slope_str = num2str(slope);

% Add legend
legend([p1 p2 p3 p4 p5 p6 p7 Line1], ...
    'Flow␣Rate␣35␣ul/min␣(t=9␣to␣t=42)', ...
    'Flow␣Rate␣70␣ul/min␣(t=42␣to␣t=53)', ...
    'Flow␣Rate␣105␣ul/min␣(t=53␣to␣t=60)', ...
    'Flow␣Rate␣140␣ul/min␣(t=60␣to␣t=72)', ...
    'Flow␣Rate␣175␣ul/min␣(t=72␣to␣t=78)', ...
    'Flow␣Rate␣0␣ul/min␣(t=78␣to␣t=92)', ...
    'Flow␣Rate␣35␣ul/min␣(t=92␣to␣t=115.354)', ...
     ['Slope␣Estimation␣=␣', slope_str, '␣%/min.']);  % Updated
        ↪ legend
```

Listing E.4: Experiment 3 with gas exchanger optical sensor data visualization

```matlab
% Step 1: Load the data from the text file
filename = 'C:\Users\koenz\OneDrive\Documenten\Thesis
    ↪ Jelle\Presens\waterflowwithGE22apriltest3withoutbs.txt';
fid = fopen(filename, 'r');
data = textscan(fid, '%*s %*s %f %f %*f %*f %f %*s',
    ↪ 'Delimiter', ';');
fclose(fid);

% Step 2: Extract the desired columns
time = data{1}; % Extract time values
air_saturation = data{2}; % Extract air saturation values

% Step 3: Define time intervals corresponding to different gas
    ↪ flow rates
gas_0 = time >= 11 & time <= 43; % Time interval for gas flow
    ↪ rate = 0 ml/min (adjusted start time to t=11 min)
gas_40_N2 = time > 43 & time <= 66; % Time interval for gas flow
    ↪ rate = 40 ml/min N2 gas
gas_40_air = time > 66 & time <= 120; % Time interval for gas
    ↪ flow rate = 40 ml/min air
gas_40_N2_2 = time > 120 & time <= 168.508; % Time interval for
    ↪ gas flow rate = 40 ml/min N2 gas

% Step 4: Plot the data with different colors for each gas flow
    ↪ rate section
figure;
hold on; % Overlay multiple plots
plot(time(gas_0), air_saturation(gas_0), 'r.-'); % Plot data for
    ↪ gas flow rate = 0 ml/min in red
plot(time(gas_40_N2), air_saturation(gas_40_N2), 'b.-'); % Plot
    ↪ data for gas flow rate = 40 ml/min N2 gas in blue
plot(time(gas_40_air), air_saturation(gas_40_air), 'g.-'); %
    ↪ Plot data for gas flow rate = 40 ml/min air in green
plot(time(gas_40_N2_2), air_saturation(gas_40_N2_2), 'b.-'); %
    ↪ Plot data for gas flow rate = 40 ml/min N2 gas (same color
    ↪ as previous N2 gas section)
xlabel('Measurement Time (min)');
ylabel('Air Saturation (%)');
title('Oxygen Measurement with Gas Exchanger');
xlim([0, 180]); % Set x-axis limit to 180 minutes
ylim([0, 160]);
grid on;

% Step 5: Add legend
legend('Gas Flow Rate = 0 ml/min (t=11 to t=43)', 'Gas Flow Rate
```

```matlab
    ↪ =␣40␣ml/min␣N2␣(t=43␣to␣t=66)', ...
 'Gas␣Flow␣Rate␣=␣40␣ml/min␣Air␣(t=66␣to␣t=120)', 'Gas␣Flow␣
    ↪ Rate␣=␣40␣ml/min␣N2␣(t=120␣to␣t=168.508)'); % Legend
    ↪ for different gas flow rates
```

F. Fabrication parameter optimization

This appendix will present all additional fabricated samples and their corresponding characterizations, along with the parameter settings utilized in the study.

F.1. General speed sweep

Settings used for the speed sweep are visible in Figure 26. Speed is swept from 50 to 1650 mm/s. The results are also visible in this section.

Sample	Power(%)	Speed(mm/s)	Repetitions(N)
O1	20	50	100
O2	20	100	100
O3	20	150	100
O4	20	200	100
O5	20	250	100
06	20	300	100
07	20	350	100
08	20	400	100
09	20	450	100
010	20	500	100
O11	20	550	100
O12	20	600	100
O13	20	650	100
O14	20	700	100
O15	20	750	100
P1	20	750	100
P2	20	900	100
P3	20	1050	100
P4	20	1200	100
P5	20	1350	100
P6	20	1500	100
P7	20	1650	100

Figure 26.: General speed sweep settings
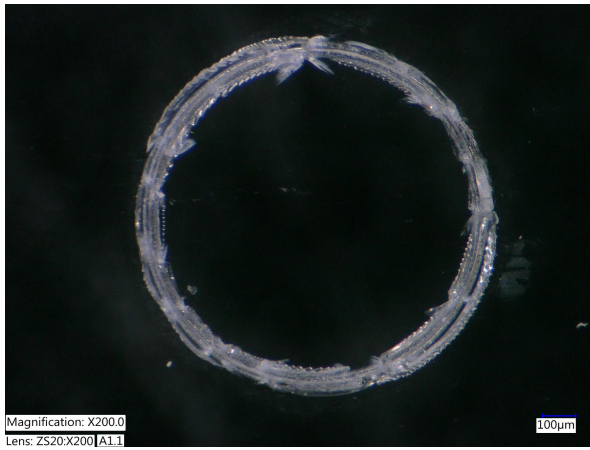
Figure 27.: Speed sample O1
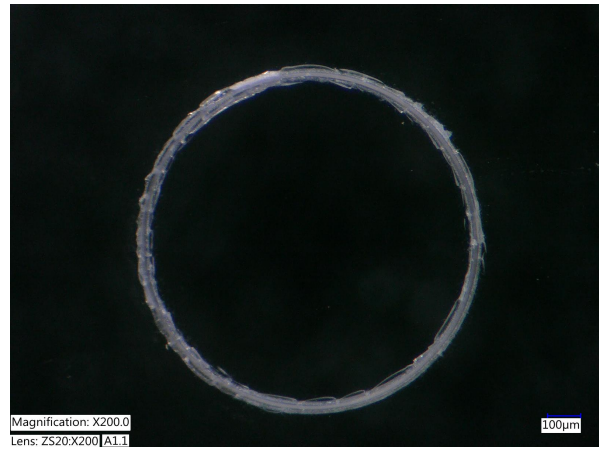
Figure 28.: Speed sample O2
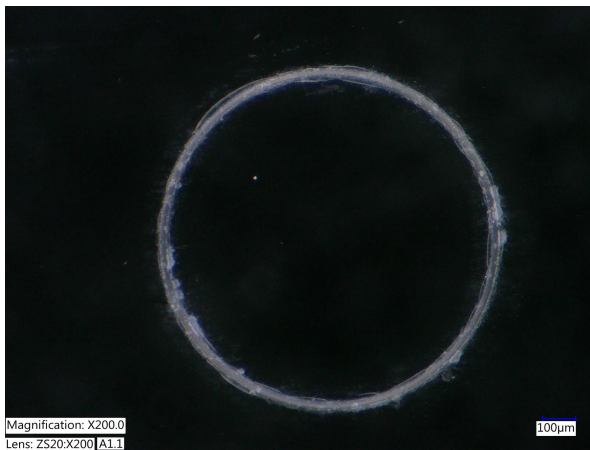
Figure 29.: Speed sample O3
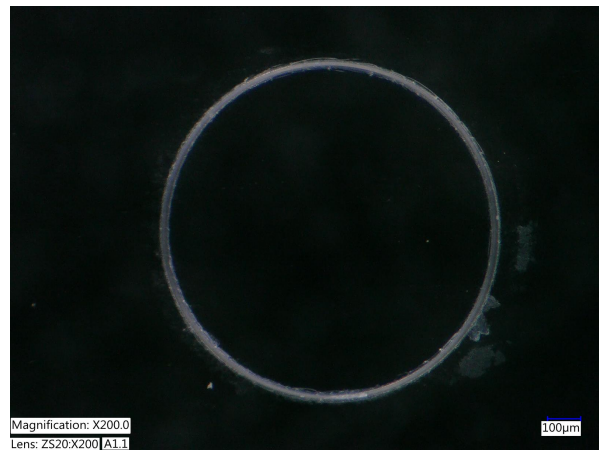
Figure 30.: Speed sample O4

Figure 31.: Speed sample O5

Figure 32.: Speed sample O6
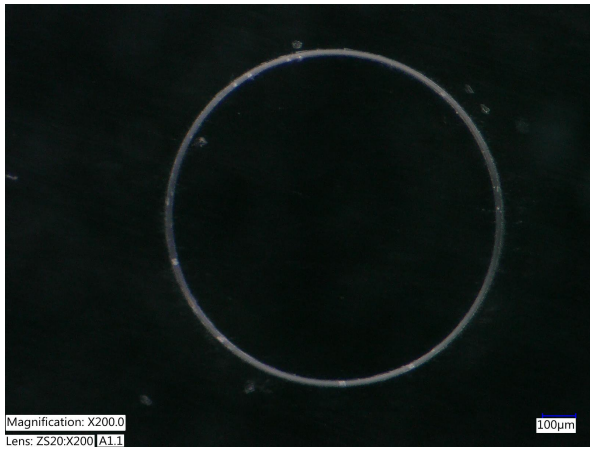
Figure 33.: Speed sample O7
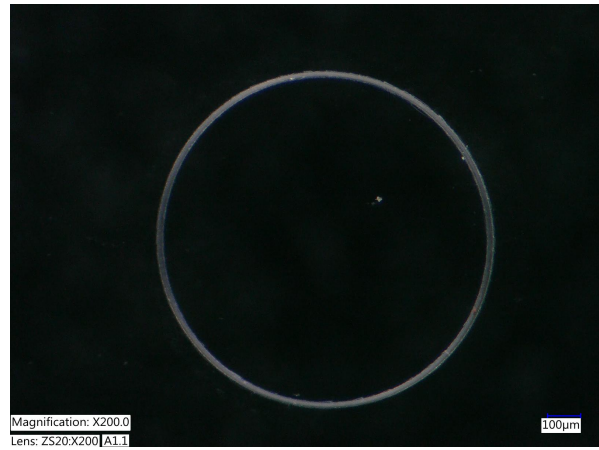
Figure 34.: Speed sample O8

Figure 35.: Speed sample O9
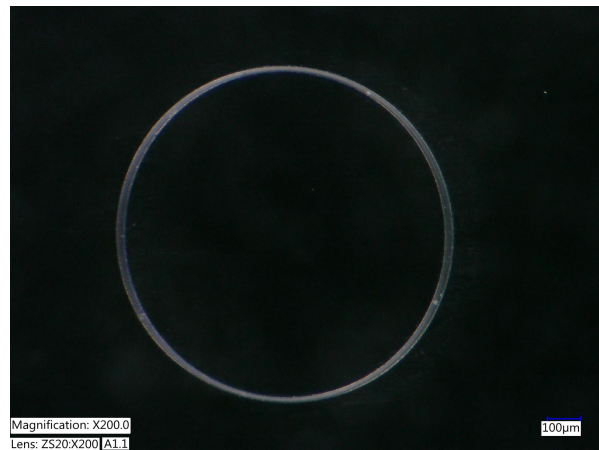
Figure 36.: Speed sample O10
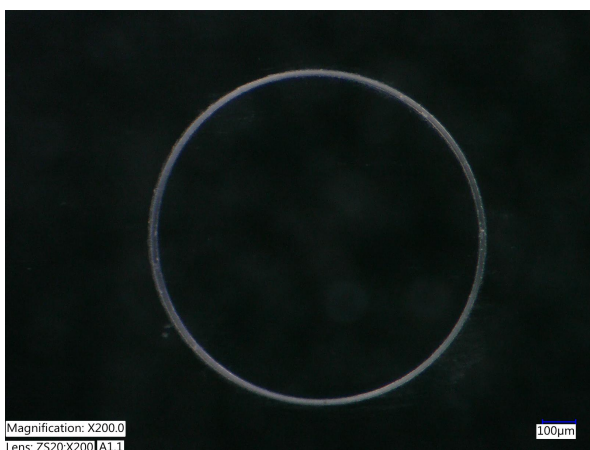
Figure 37.: Speed sample O11

Figure 38.: Speed sample O12
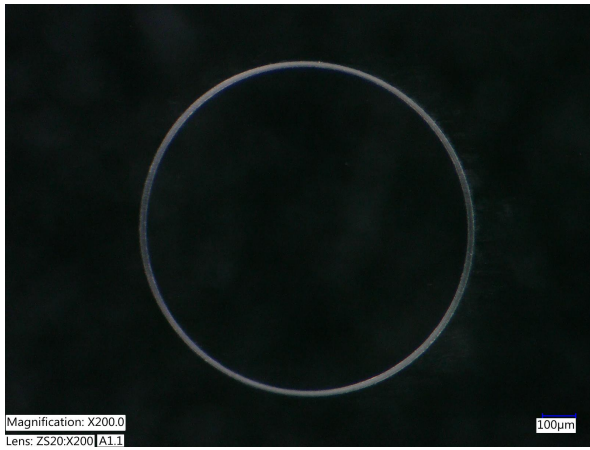
Figure 39.: Speed sample O13
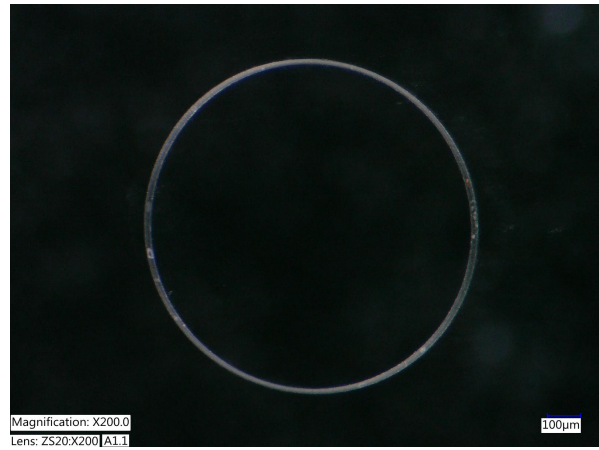
Figure 40.: Speed sample O14
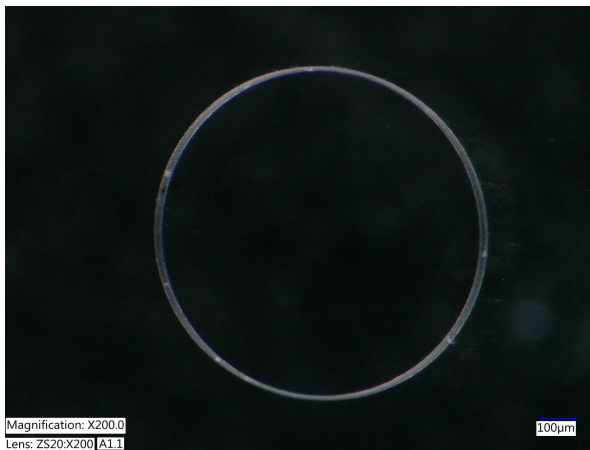
Figure 41.: Speed sample O15
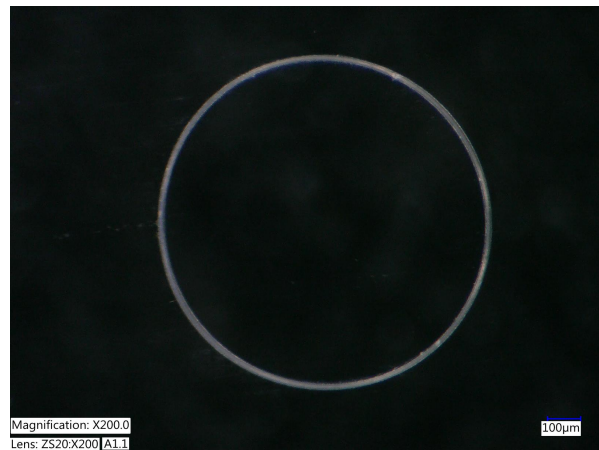
Figure 42.: Speed sample P1

Figure 43.: Speed sample P2

Figure 44.: Speed sample P3
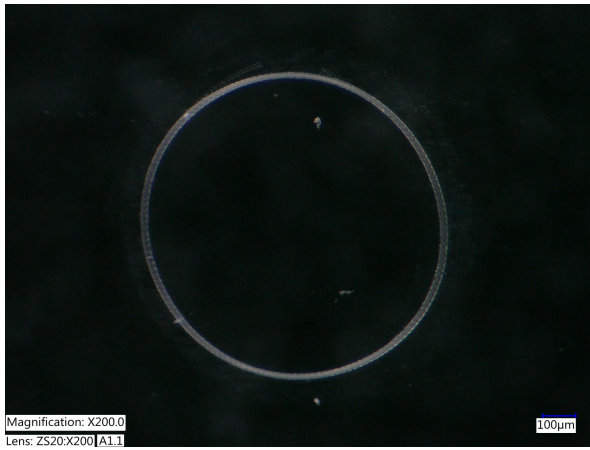
Figure 45.: Speed sample P4
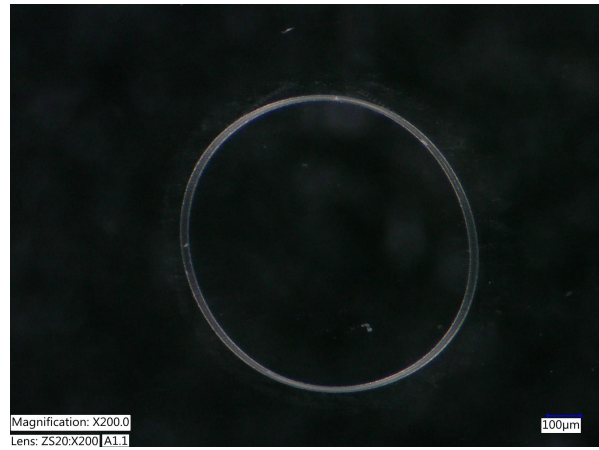
Figure 46.: Speed sample P5
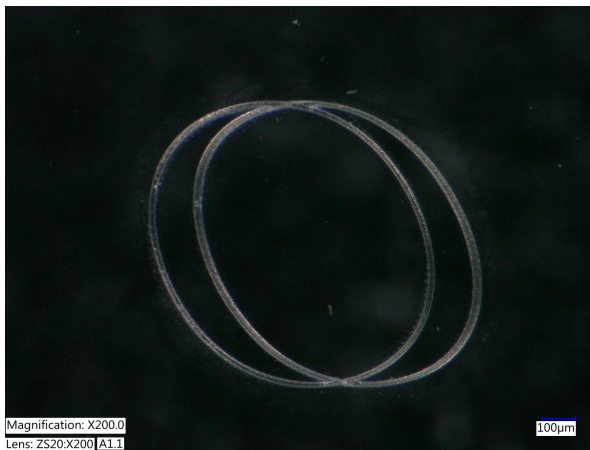
Figure 47.: Speed sample P6

Figure 48.: Speed sample P7

F.2. Through hole outline pitch sweep

Settings used for the through hole outline pitch sweep are visible in Figure 49. The outline pitch is swept from 0.0125 to 0.125 mm. The results are also visible in this section.

Sample	Power(%)	Speed(mm/s)	Repetitions(N)	Outline pitch(mm)	Outlines
A1	20	100	1000	0.0125	3
A2	20	100	1000	0.025	3
A3	20	100	1000	0.0375	3
A4	20	100	1000	0.05	3
A5	20	100	1000	0.0625	3
A6	20	100	1000	0.075	3
A7	20	100	1000	0.0875	3
A8	20	100	1000	0.1	3
A9	20	100	1000	0.1125	3
A10	20	100	1000	0.125	3

Figure 49.: Outline pitch sweep settings
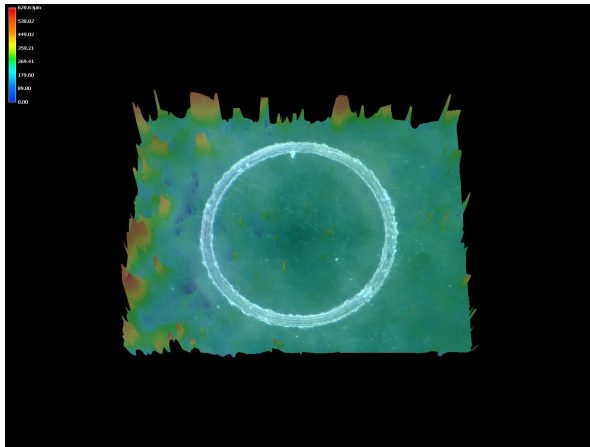
3D Heat Map Sample A1
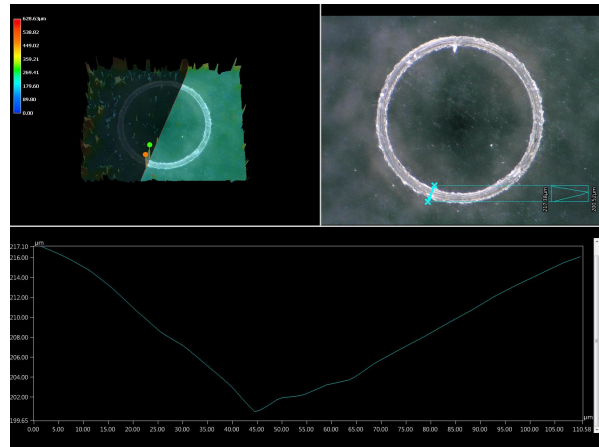
Surface Profile Sample A1
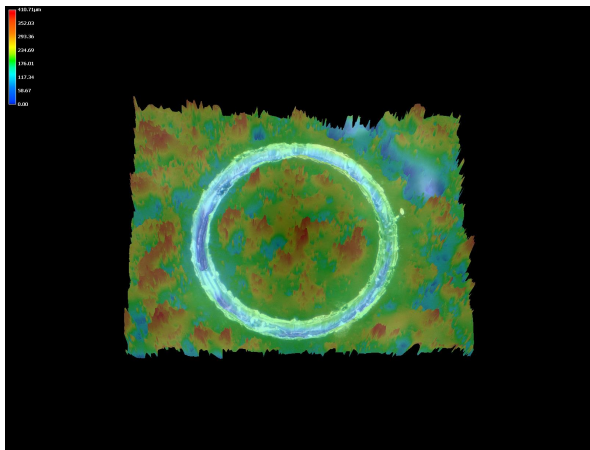
3D Heat Map Sample A2
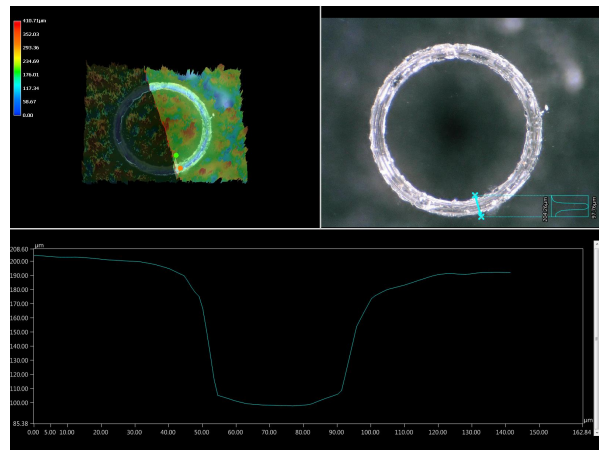
Surface Profile Sample A2
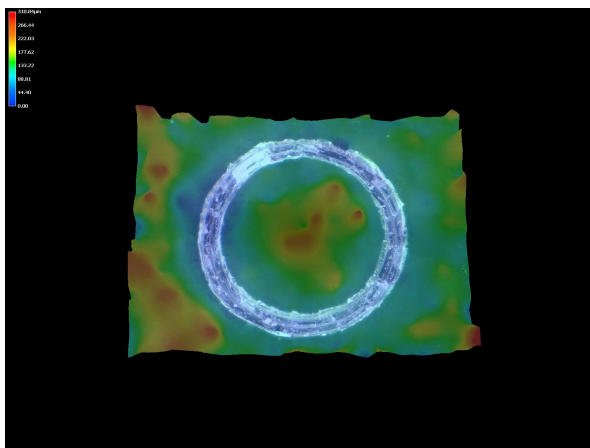
3D Heat Map Sample A3
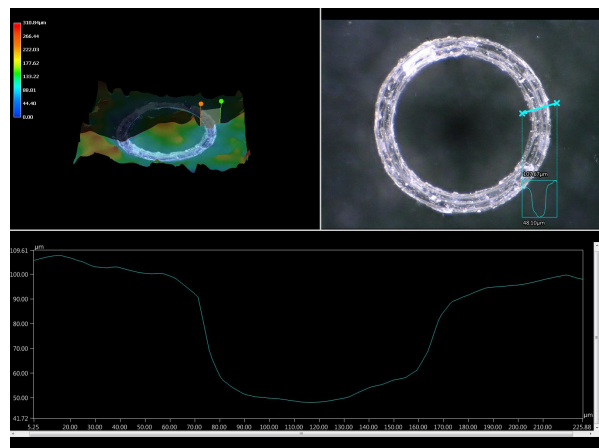
Surface Profile Sample A3
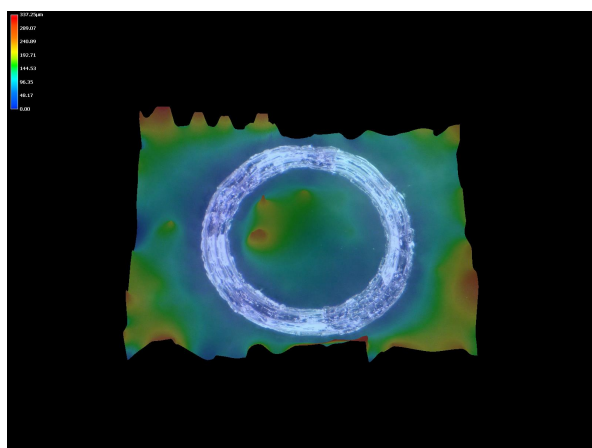
3D Heat Map Sample A4
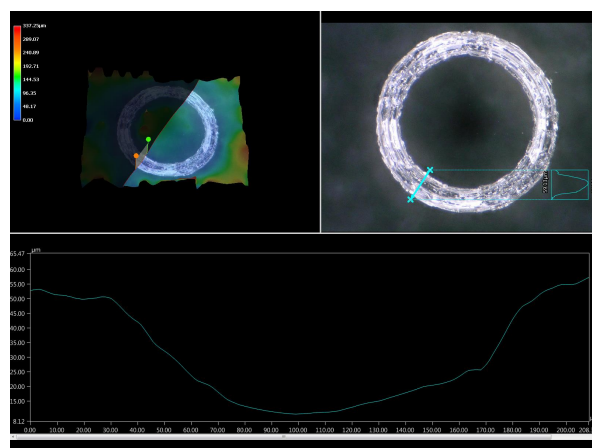
Surface Profile Sample A5
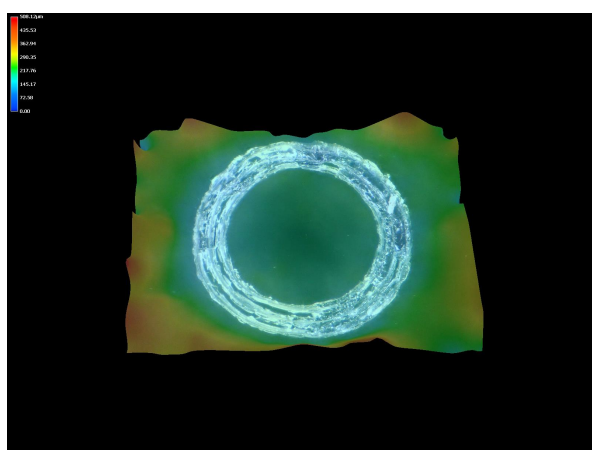
3D Heat Map Sample A6
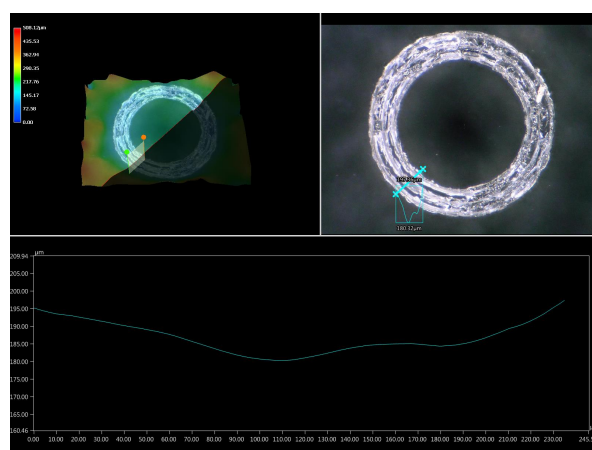
Surface Profile Sample A6
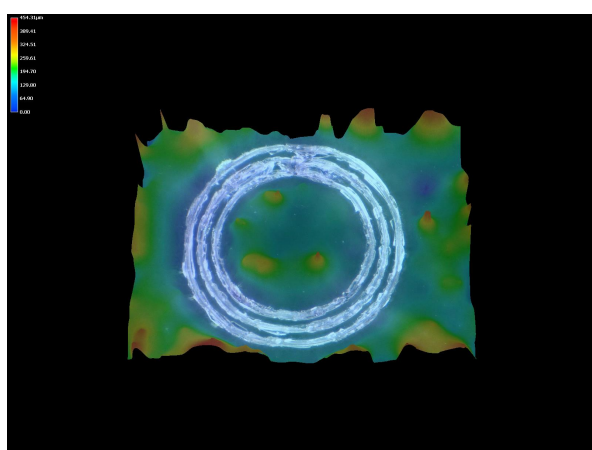
3D Heat Map Sample A7
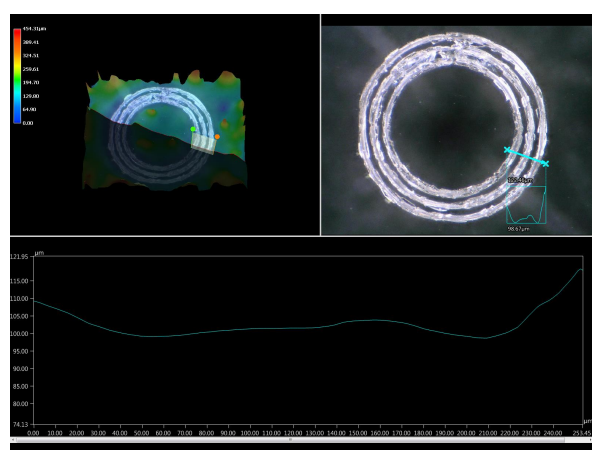
Surface Profile Sample A7
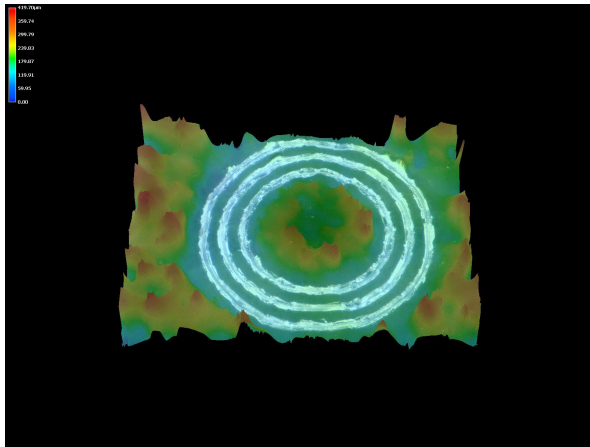
3D Heat Map Sample A8
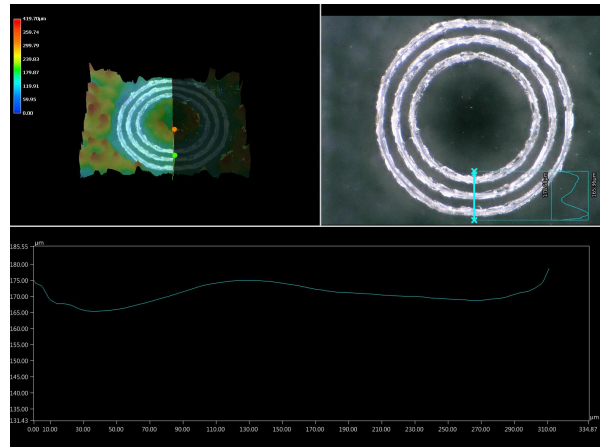
Surface Profile Sample A8
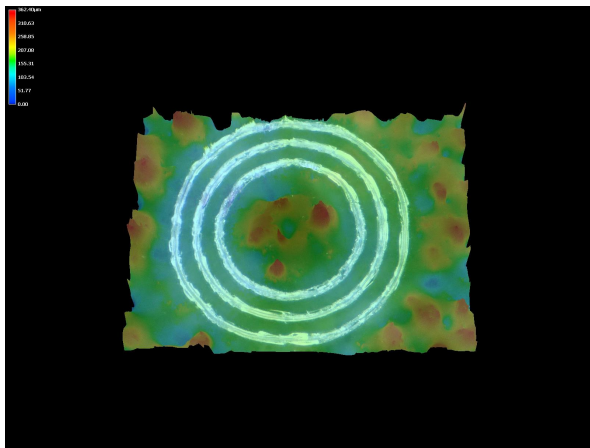
3D Heat Map Sample A9
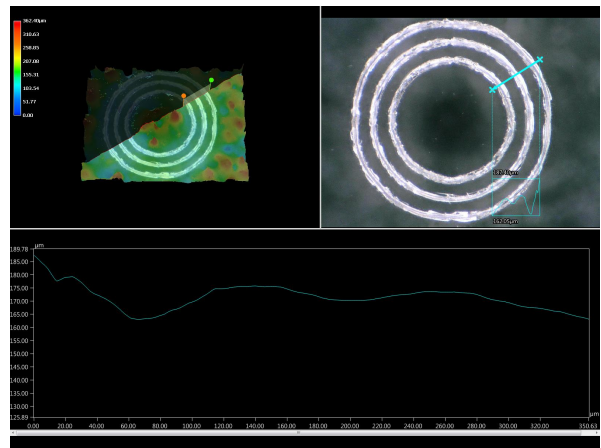
Surface Profile Sample A9
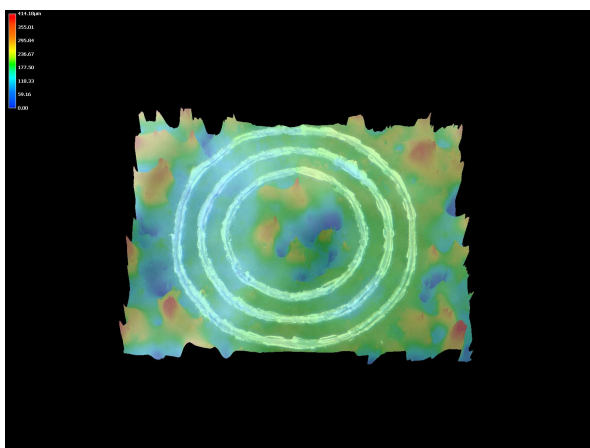
3D Heat Map Sample A10
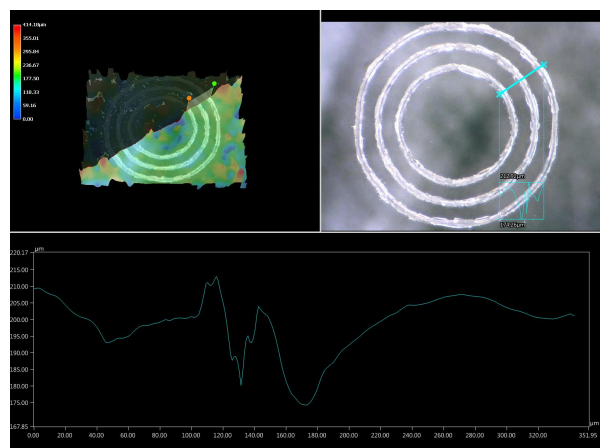
Surface Profile Sample A10

F.3. Through hole repetitions sweep

Settings used for the through hole repetitions sweep are visible in Figure 50. The number of repetitions is swept from 100 to 1000 times. The results are also visible in this section.

Sample	Power(%)	Speed(mm/s)	Repetitions(N)	Outline pitch(mm)	Outlines
B1	20	100	100	0.025	3
B2	20	100	200	0.025	3
B3	20	100	300	0.025	3
B4	20	100	400	0.025	3
B5	20	100	500	0.025	3
B6	20	100	600	0.025	3
B7	20	100	700	0.025	3
B8	20	100	800	0.025	3
B9	20	100	900	0.025	3
B10	20	100	1000	0.025	3

Figure 50.: Repetitions sweep settings
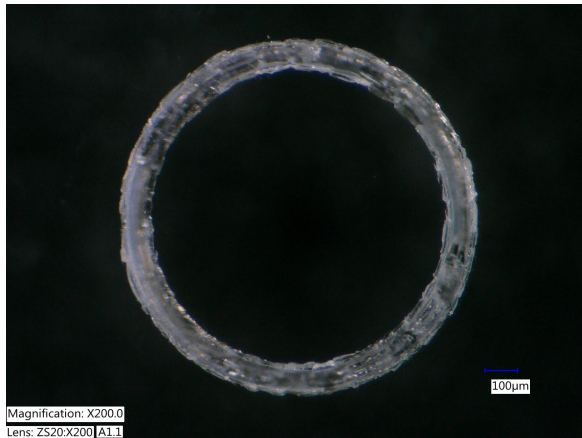
Overview Picture Sample B1
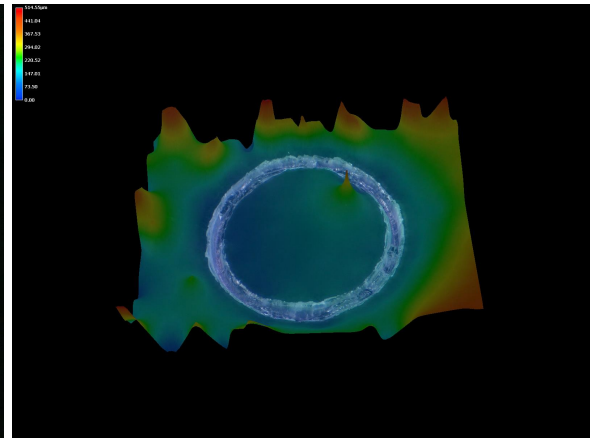
3D Heat Map Sample B1
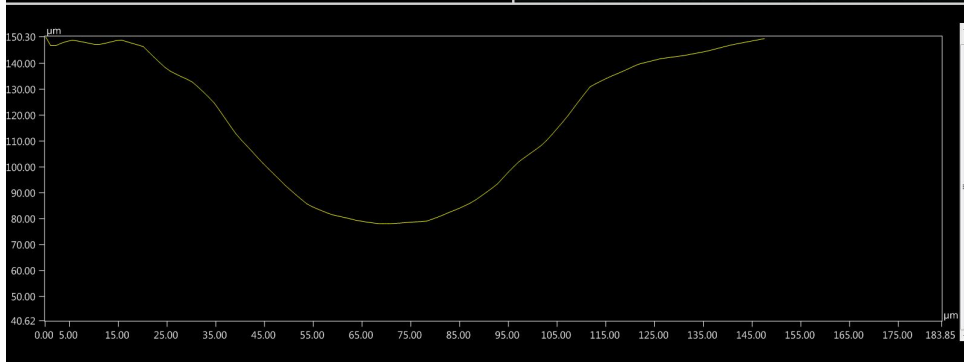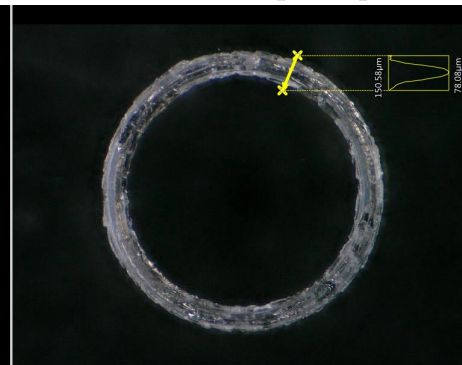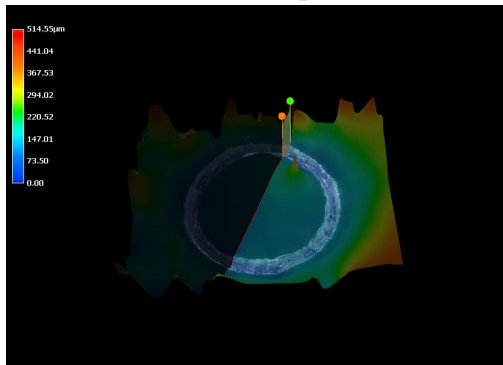
Surface Profile Sample B1
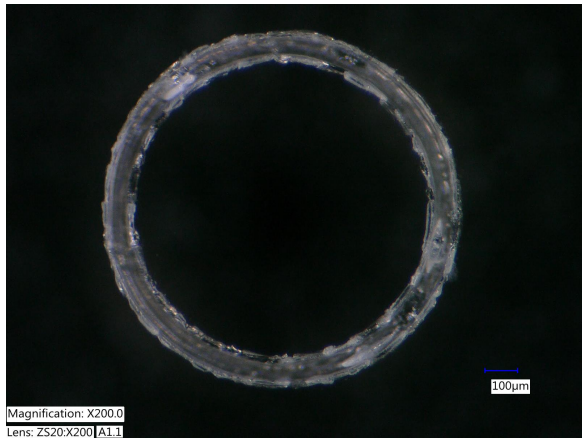
Overview Picture Sample B2
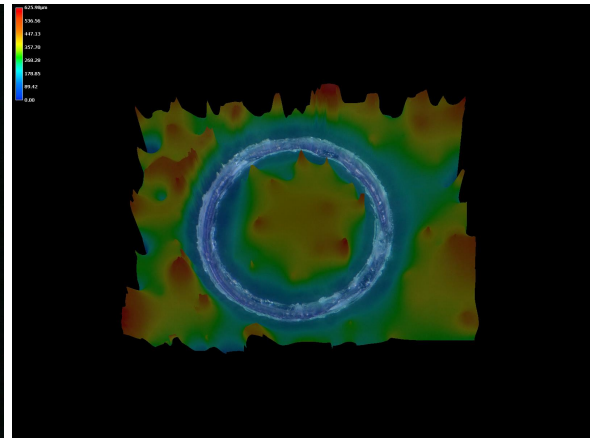
3D Heat Map Sample B2
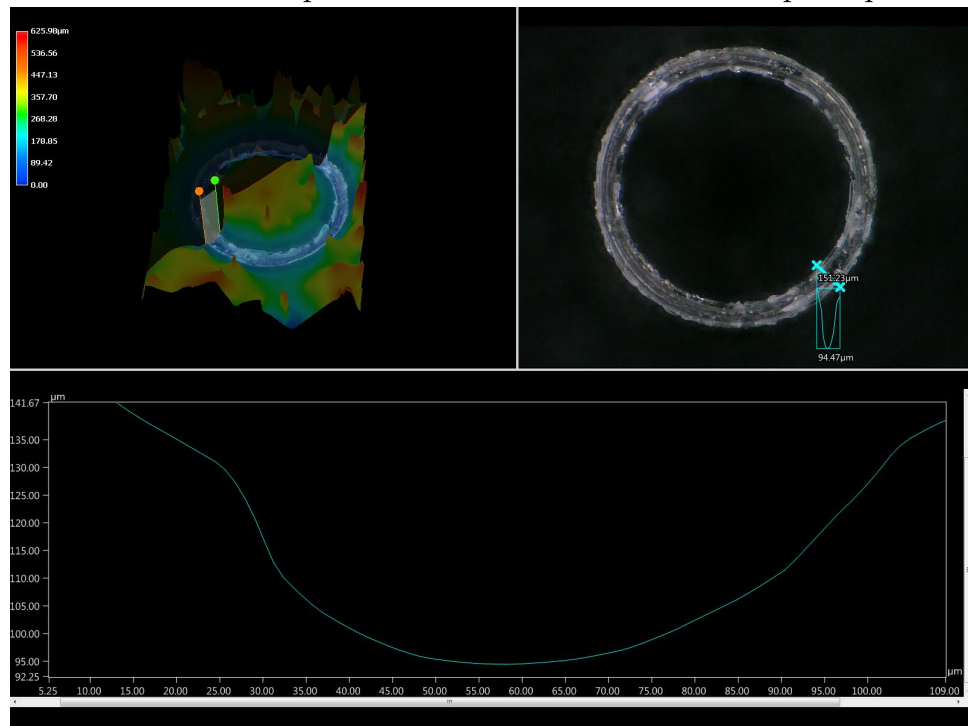
Surface Profile Sample B2
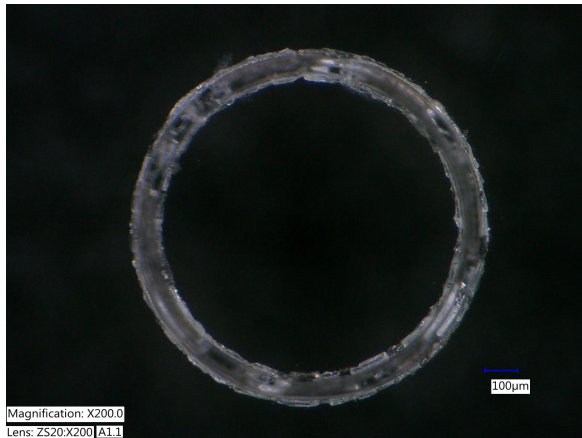
Overview Picture Sample B3
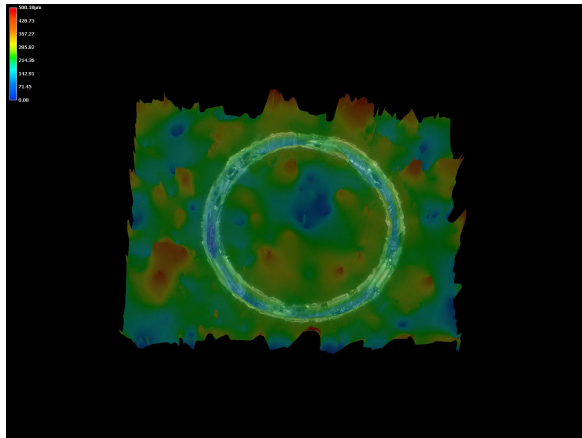
3D Heat Map Sample B3
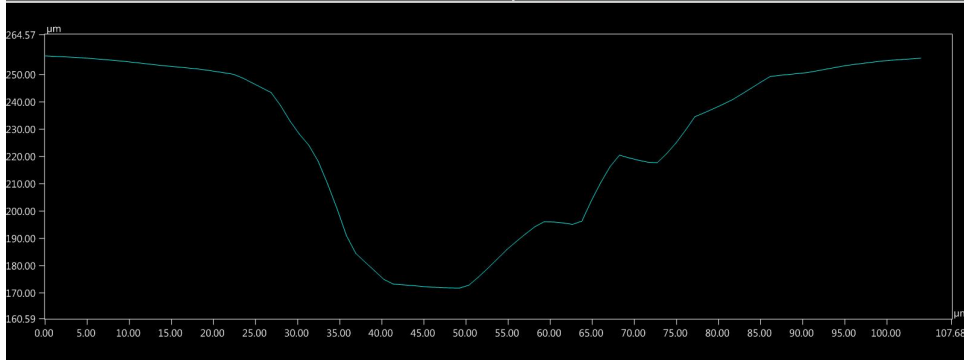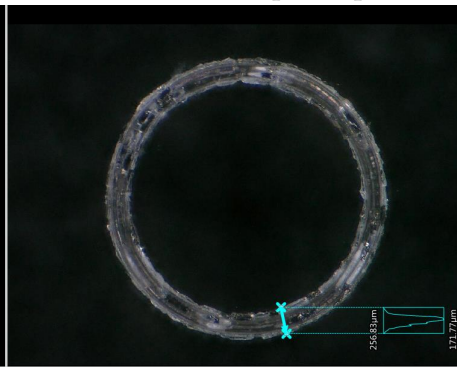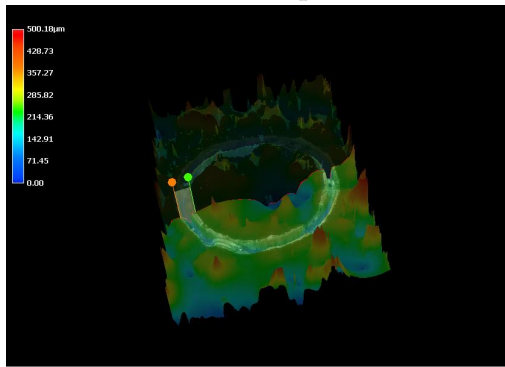
Surface Profile Sample B3
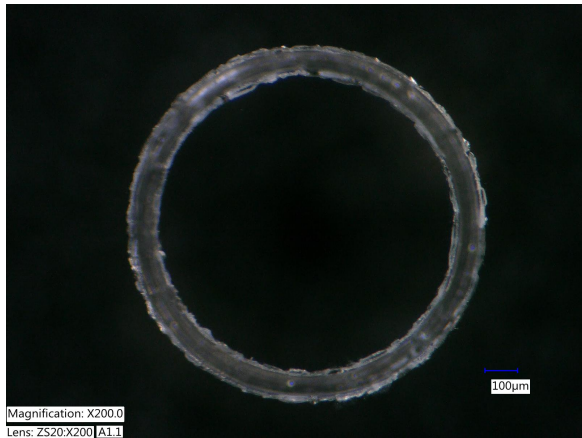
Overview Picture Sample B4
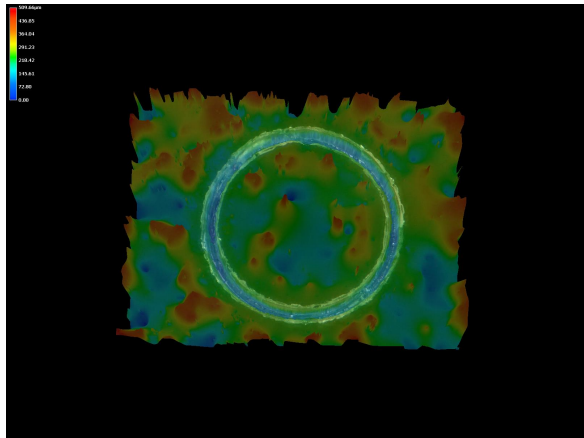
3D Heat Map Sample B4
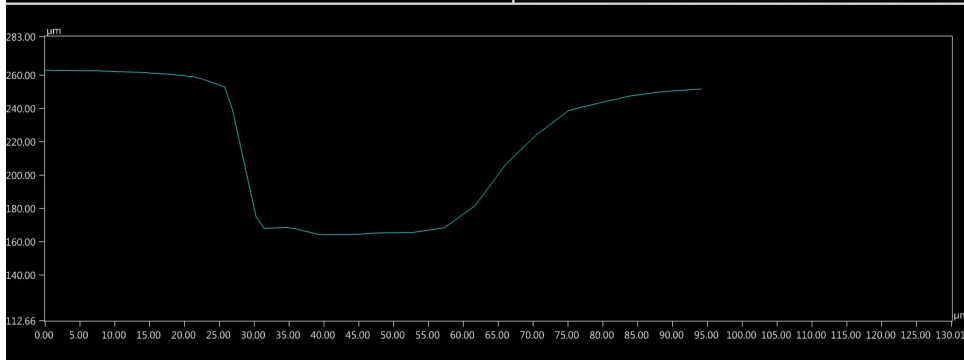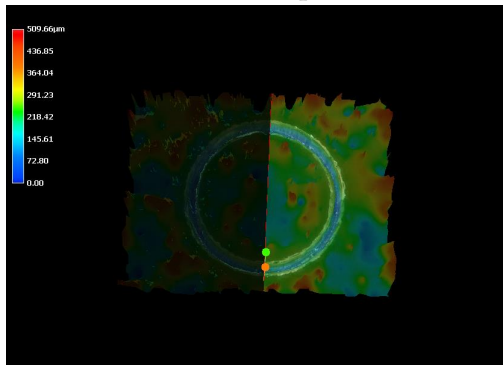
Surface Profile Sample B4
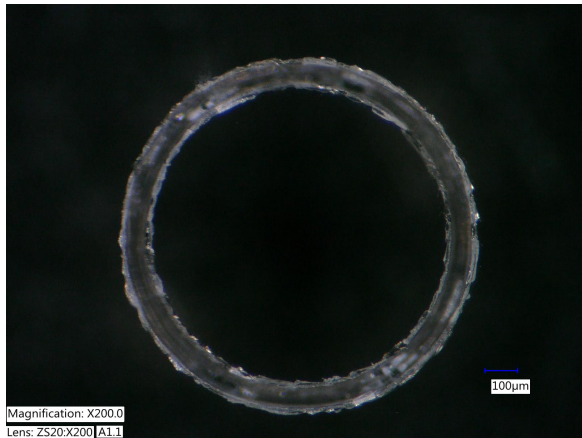
Overview Picture Sample B5
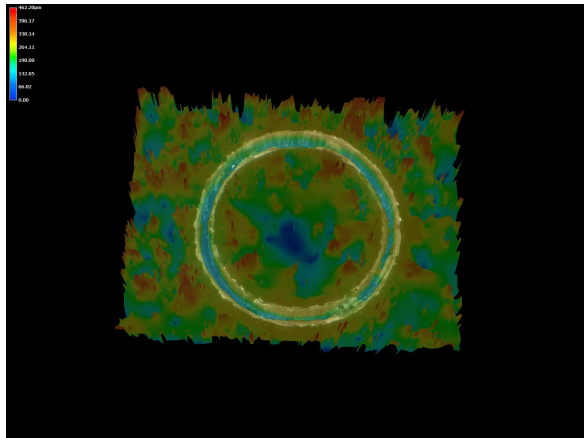
3D Heat Map Sample B5
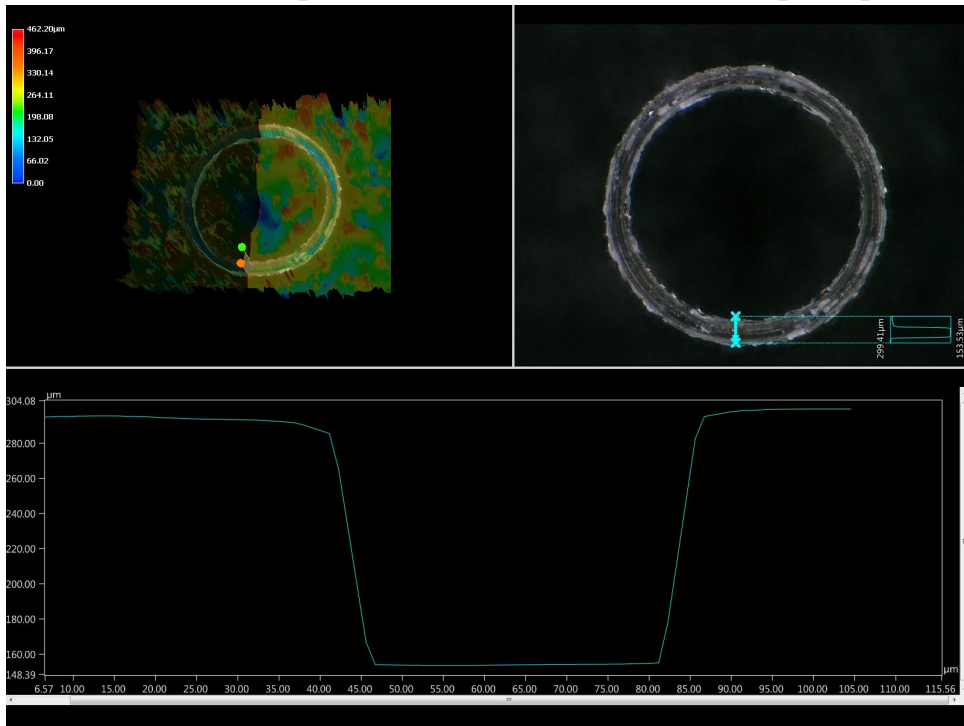
Surface Profile Sample B5
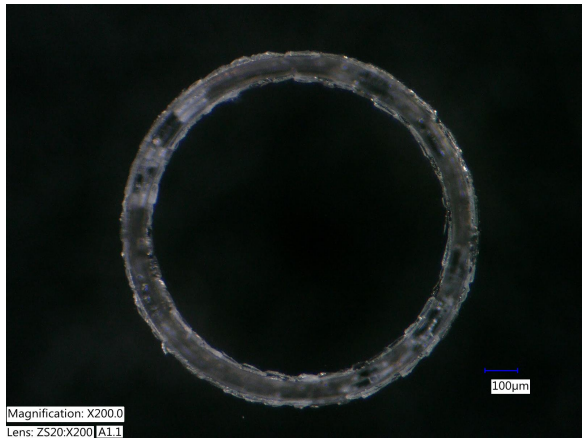
Overview Picture Sample B6
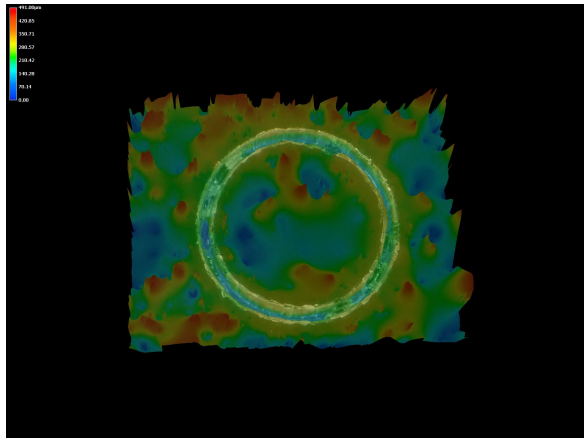
3D Heat Map Sample B6
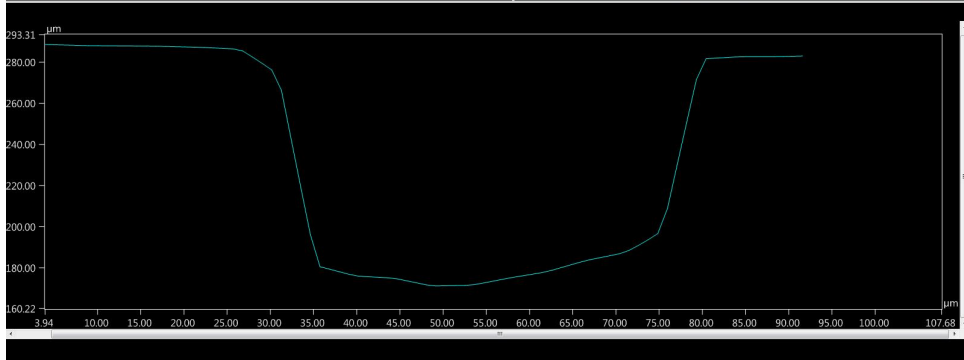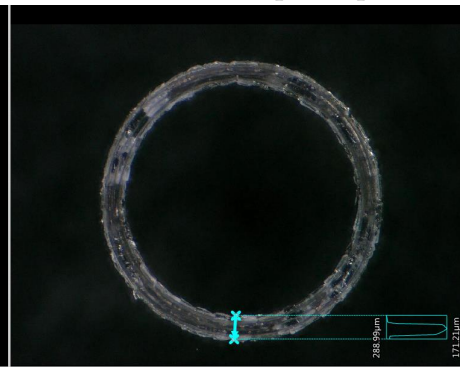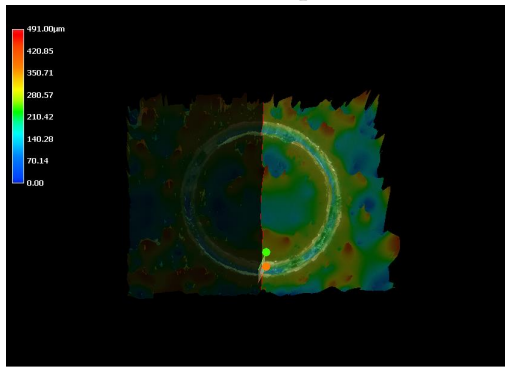
Surface Profile Sample B6
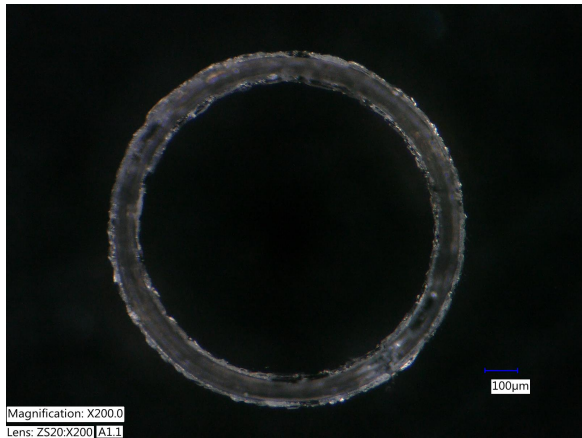
Overview Picture Sample B7
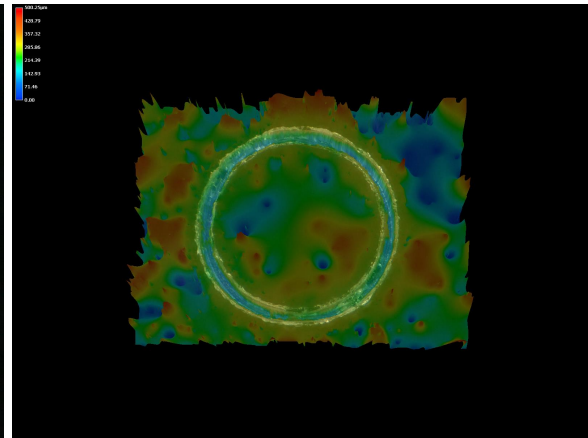
3D Heat Map Sample B7
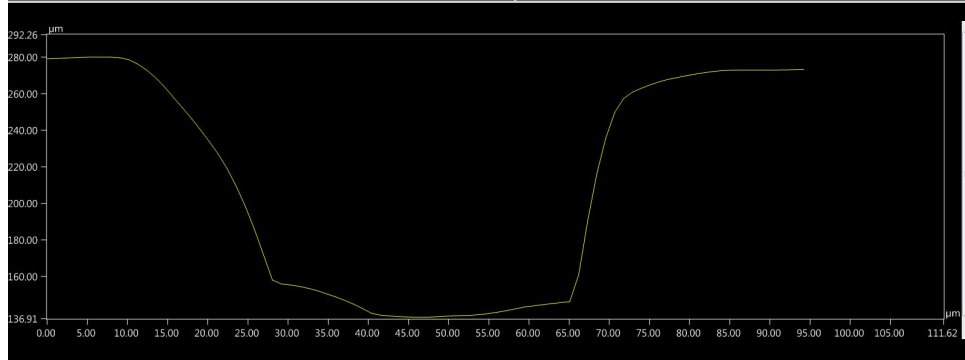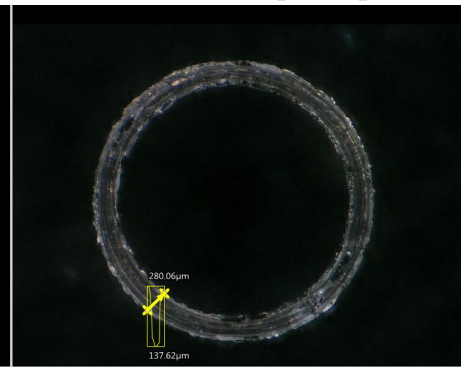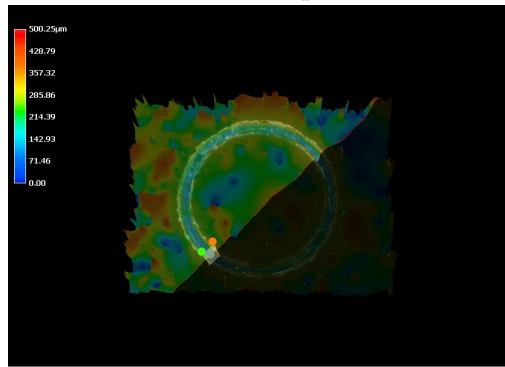
Surface Profile Sample B7
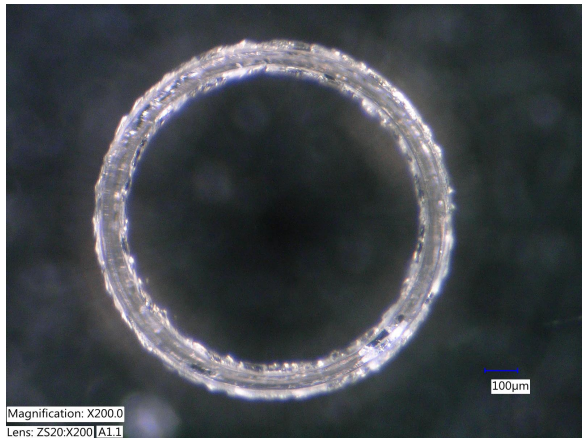
Overview Picture Sample B8
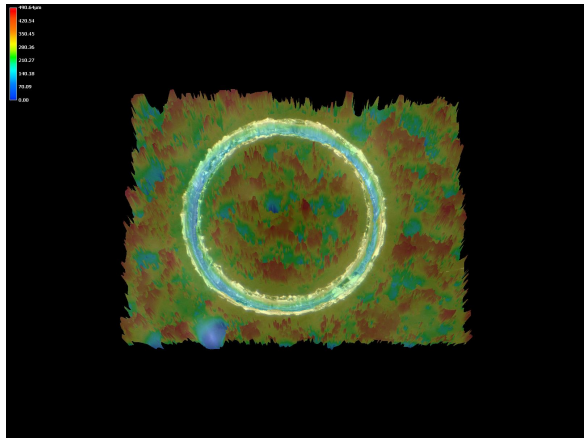
3D Heat Map Sample B8
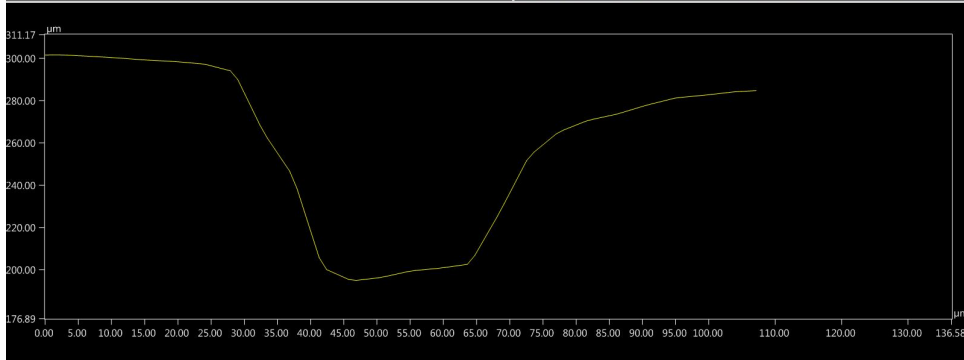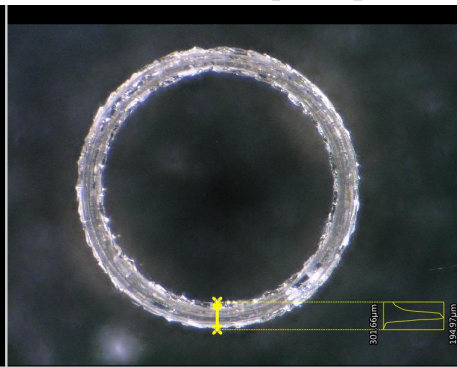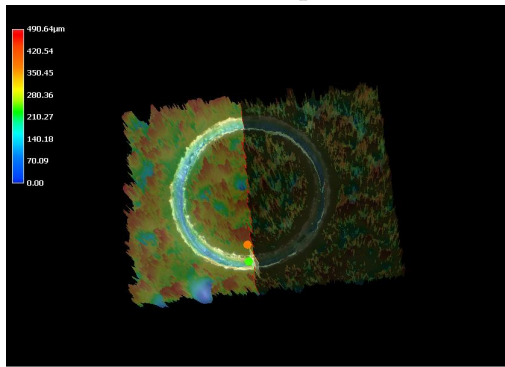
Surface Profile Sample B8
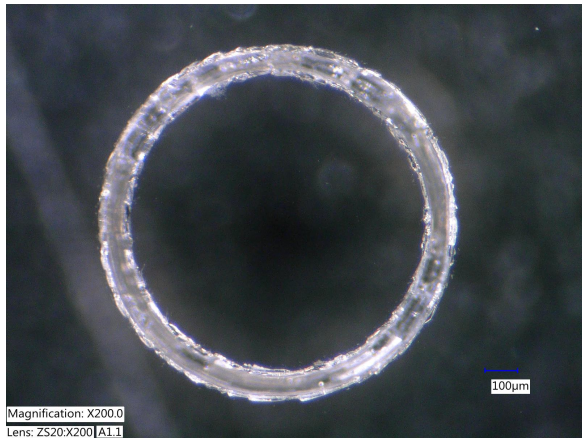
Overview Picture Sample B9
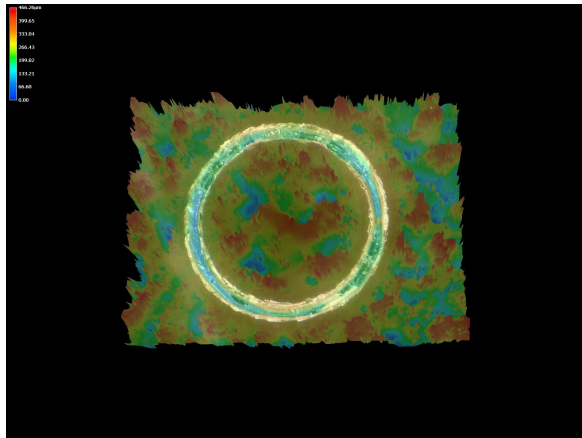
3D Heat Map Sample B9
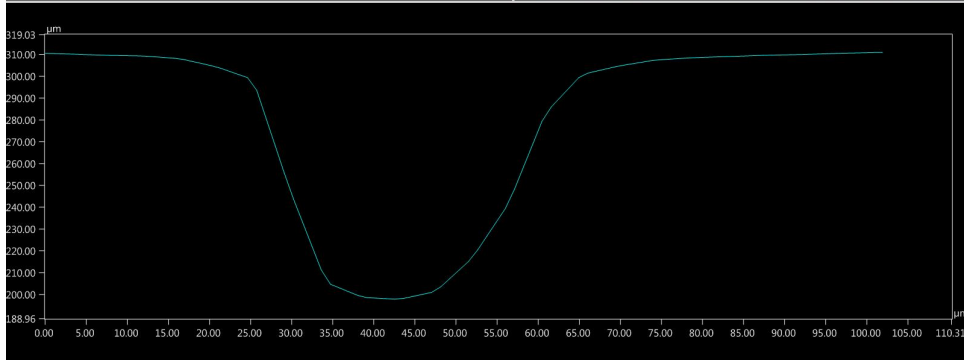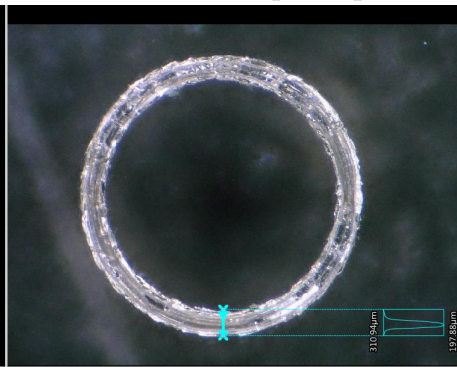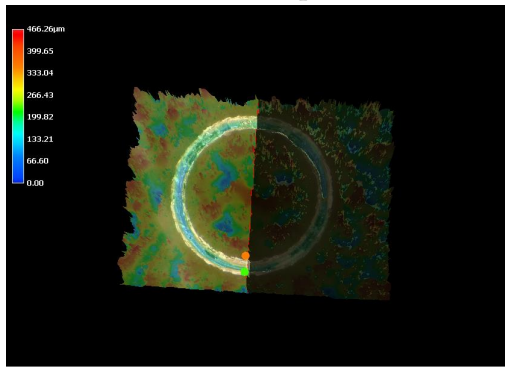
Surface Profile Sample B9
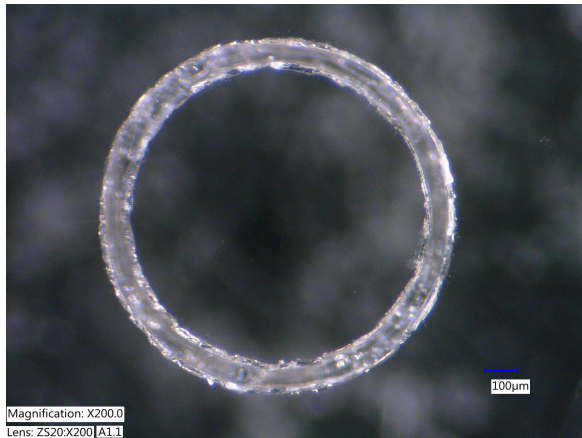
Overview Picture Sample B10   3D Heat Map Sample B10
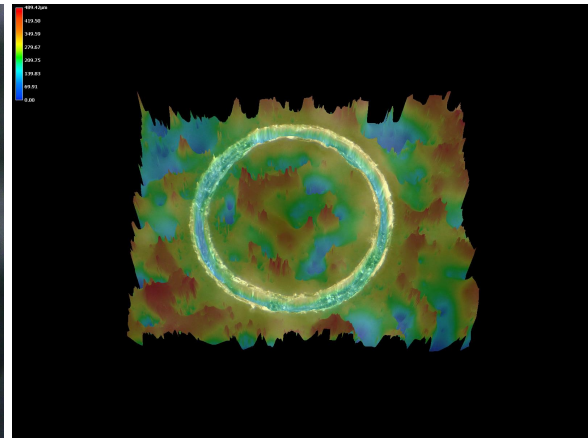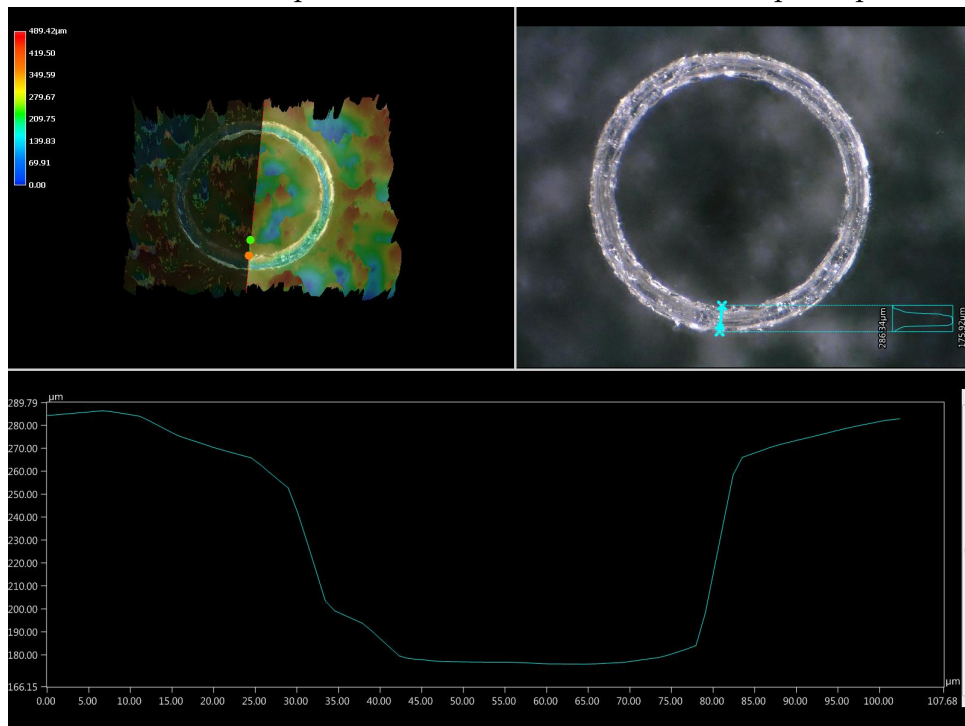
Surface Profile Sample B10

F.4. Through hole perimeter cutting vs. area hatching settings

Settings used for both methods for through holes are visible in Figure 61.

Sample	Power(%)	Speed(mm/s)	Repetitions(N)	Outline pitch(mm)	Outlines	Layers(N)	Layer pitch(mm)	Hatch pitch(mm)	Hatch pattern	Note
Through hole perimeter cutting	40	100	300	0.025	3	10	0.1	N/A	N/A	Flip over and repeat, diameter=1.8 mm
Through hole area hatching	15	150	10	N/A	N/A	10	0.1	0.0015	horizontal	Diameter=1.8 mm

Figure 61.: Settings used for both methods for through holes

F.5. Gas exchanger through hole settings used

Settings used for the different gas exchanger through holes are visible in Figure 62.

Sample	Power(%)	Speed(mm/s)	Repetitions(N)	Outline pitch(mm)	Outlines	Layers(N)	Layer pitch(mm)	Hatch pitch(mm)	Hatch pattern	Note
Through holes alignment	40	100	300	0.025	3	10	0.1	N/A	N/A	Flip over and repeat, diameter=2 mm
Gas through hole	40	100	300	0.025	3	10	0.1	N/A	N/A	Flip over and repeat, diameter=1.7 mm
Liquid through hole	15	150	10	N/A	N/A	10	0.1	0.0015	horizontal	Diameter=0.3 mm

Figure 62.: Settings used for the gas exchanger through holes

F.6. Channel engraving square sweep

Settings used for the square channel different parameter sweep are visible in Figure 63. The results are also visible in this section.

Sample	Power(%)	Speed(mm/s)	Repetitions(N)	Hatch pitch(mm)	Hatch pattern
Square 1	15	150	100	0.0015	horizontal
Square 2	5	150	30	0.0075	horizontal
Square 3	5	150	50	0.0075	horizontal
Square 4	3	150	50	0.0075	horizontal
Square 5	3	150	100	0.0075	horizontal
Square 6	3	150	150	0.0075	horizontal
Square 7	3	150	150	0.0075	erode
Square 8	3	150	150	0.0075	diagonal 135-degree
Square 9	3	150	100	0.0015	horizontal
Square 10	1	150	100	0.0015	horizontal

Figure 63.: Parameter settings square channel samples
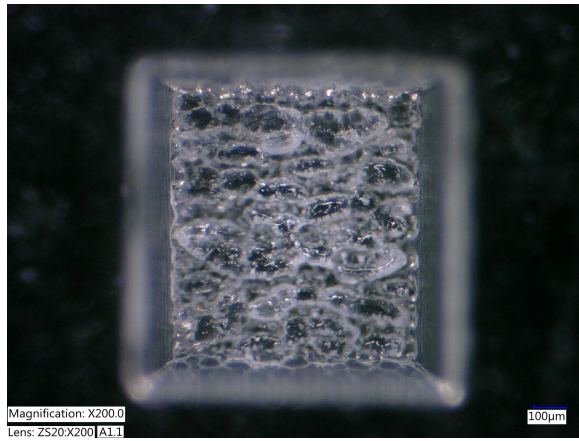
Overview Picture square 1
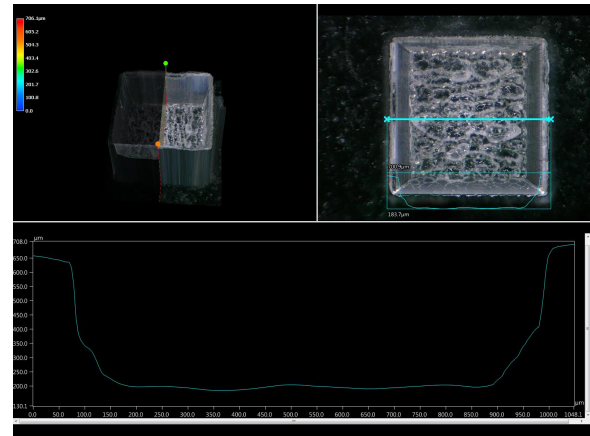
Surface Profile square 1
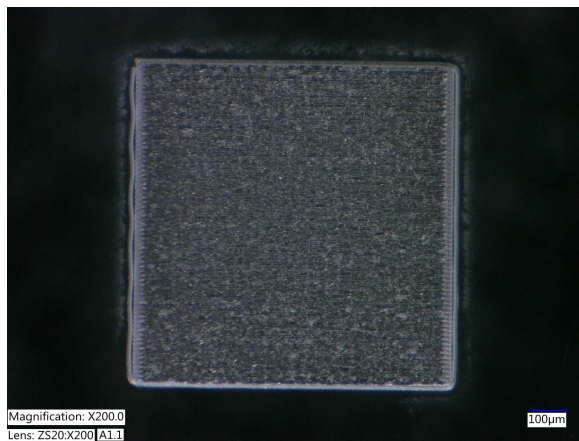
Overview Picture square 2
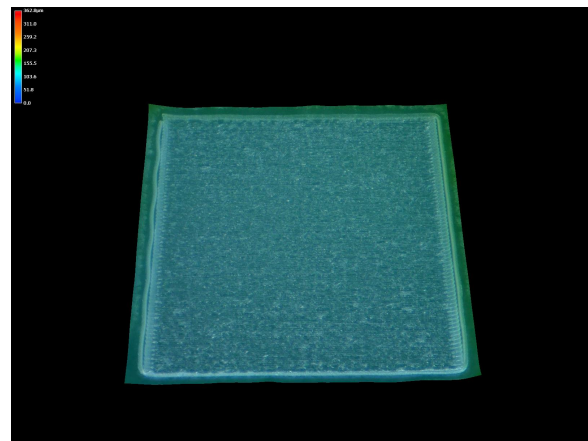
3D Heat Map square 2
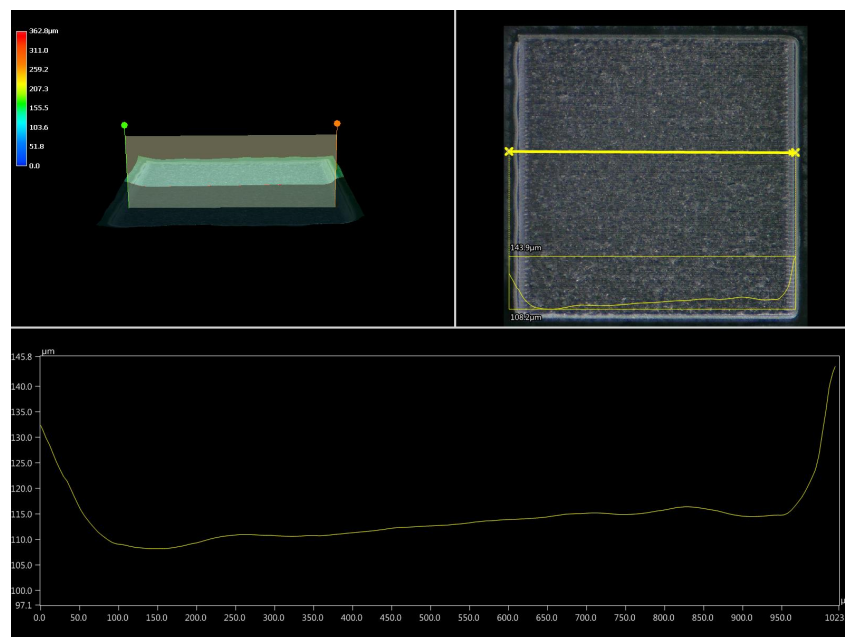
Surface Profile square 2
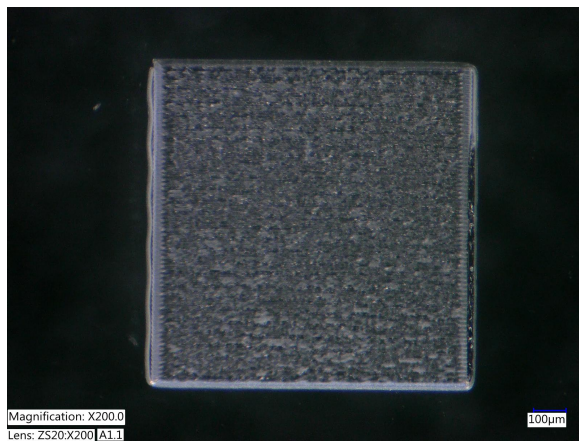
Overview Picture square 3
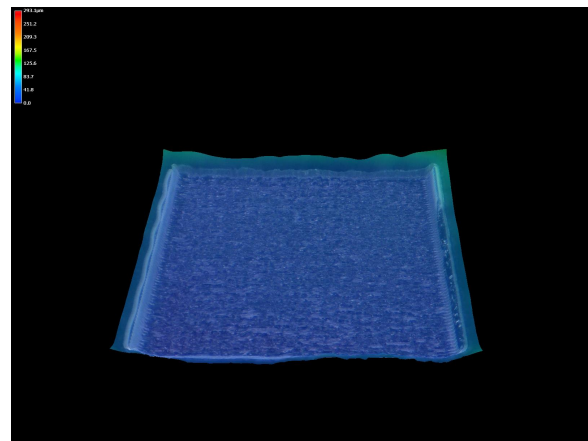
3D Heat Map square 3
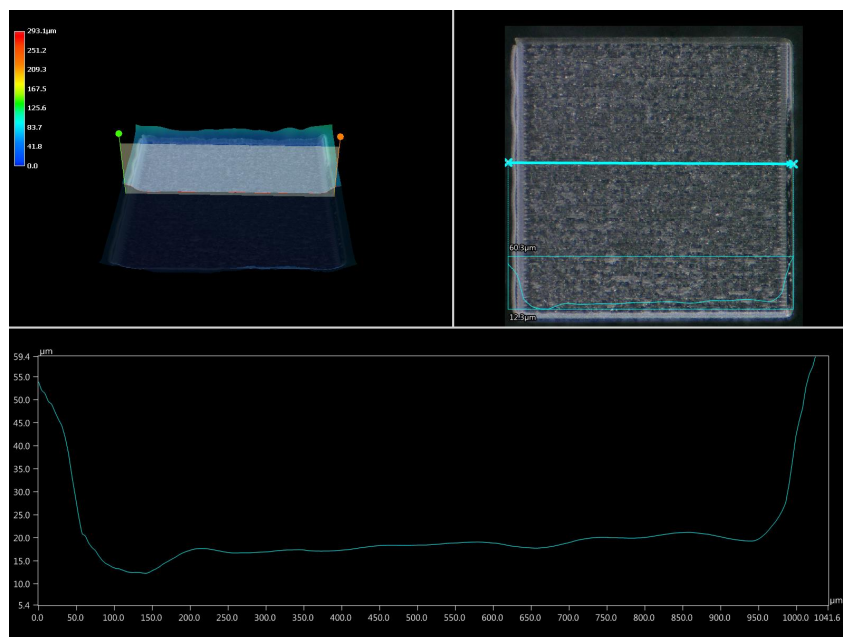
Surface Profile square 3
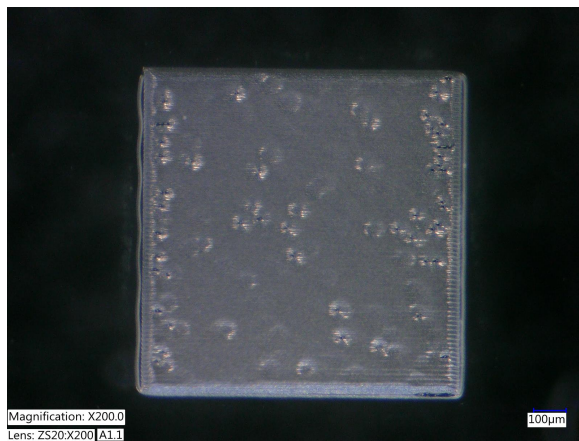
Overview Picture square 4
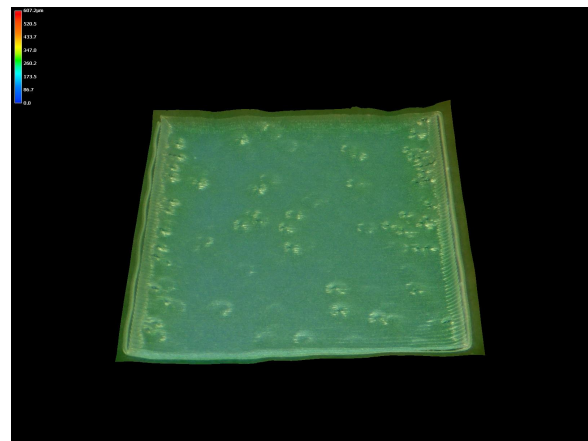
3D Heat Map square 4
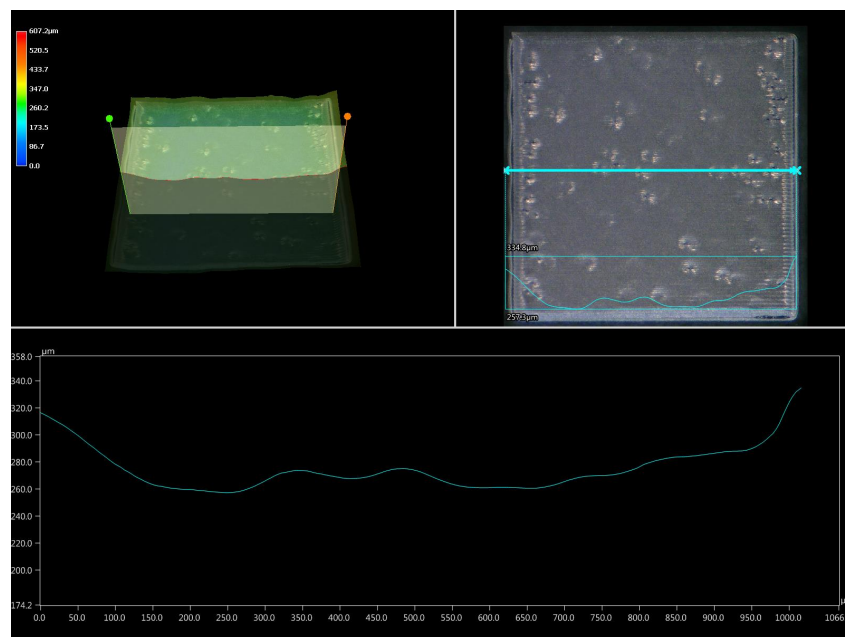
Surface Profile square 4
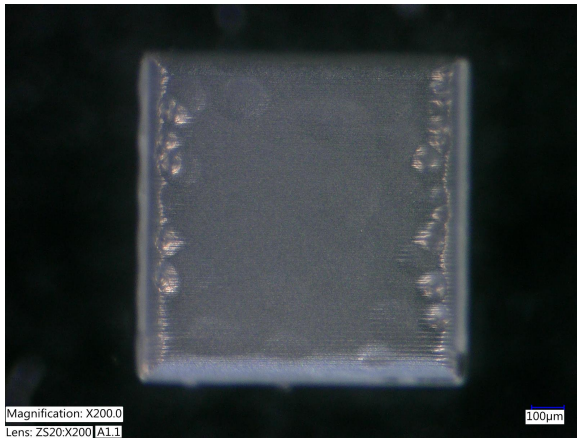
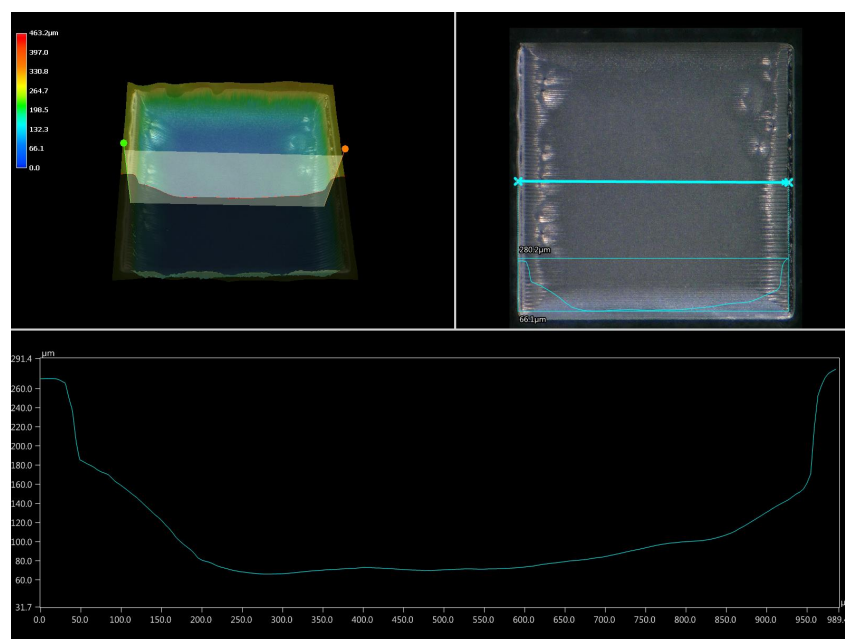Overview Picture square 5
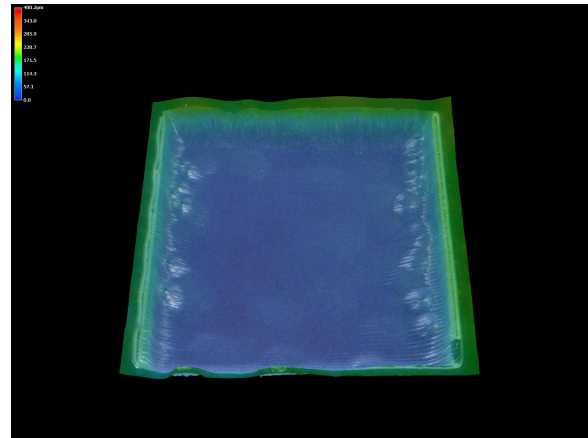
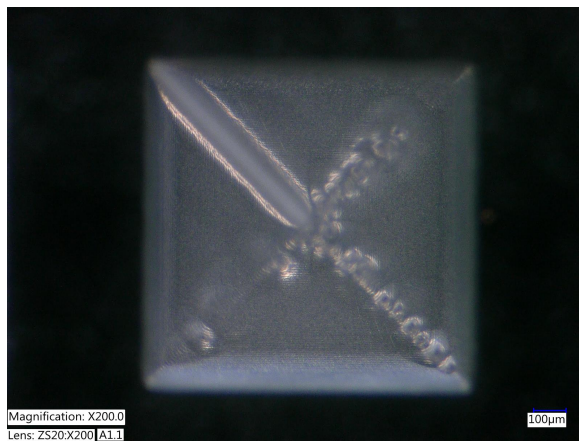3D Heat Map square 5
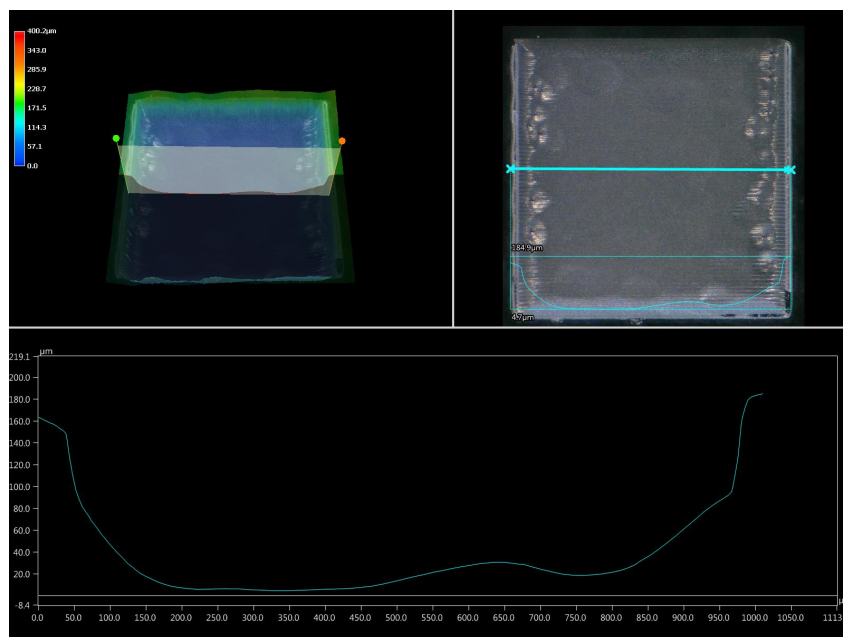
Surface Profile square 5
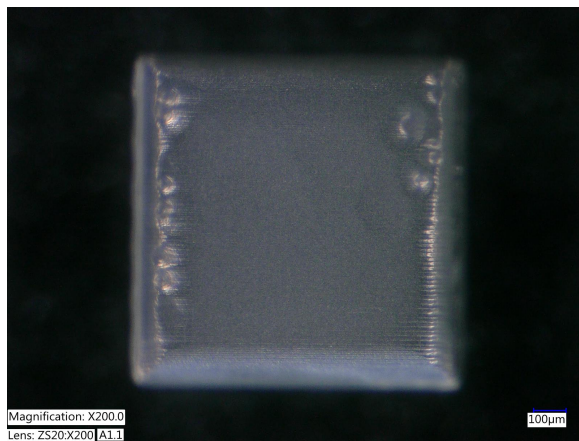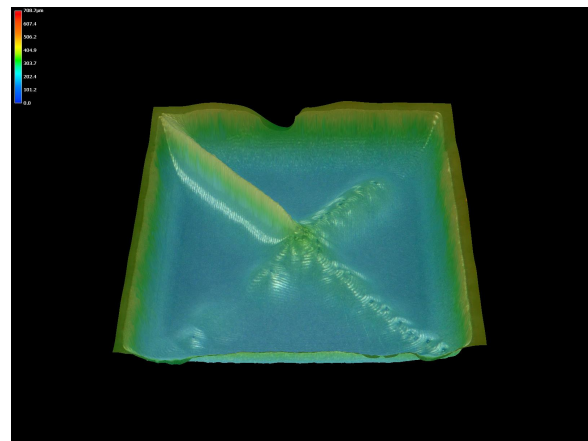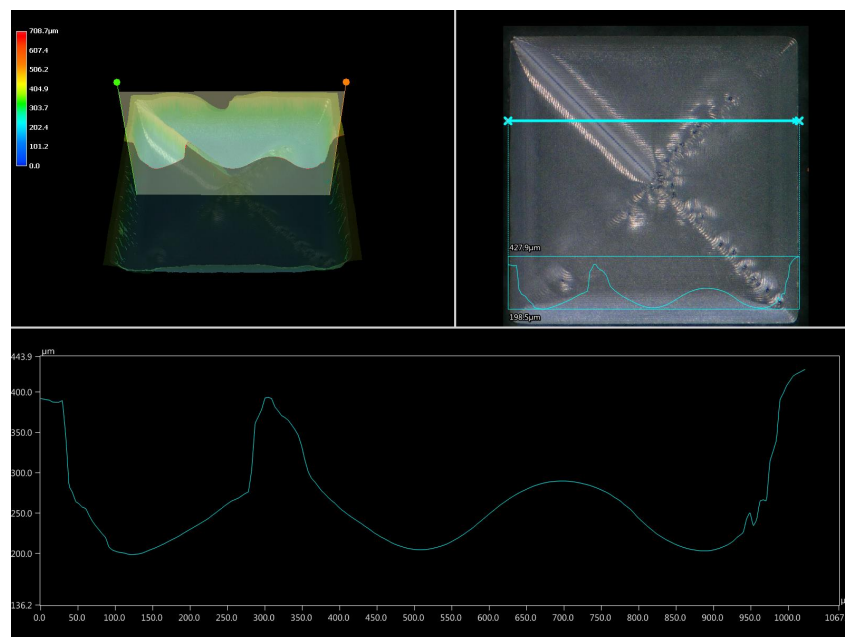
Overview Picture square 6
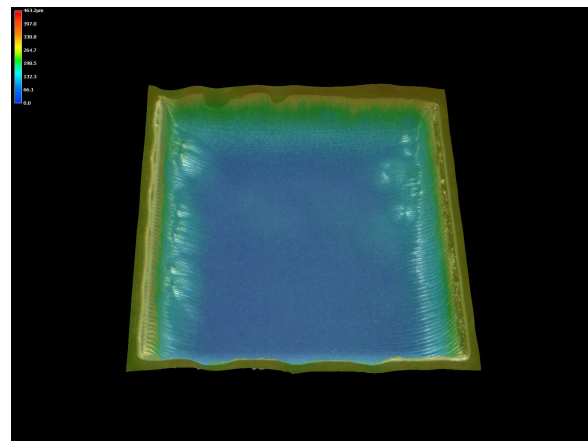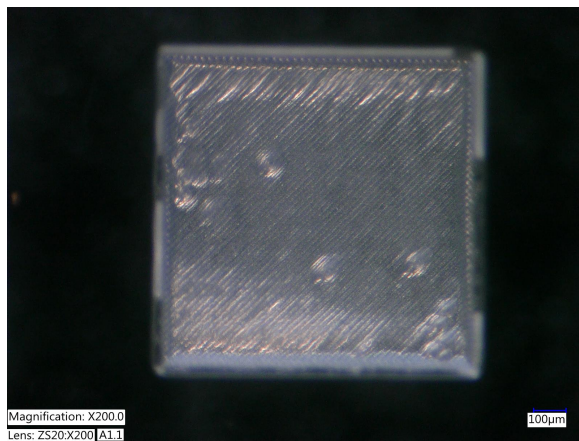

3D Heat Map square 6

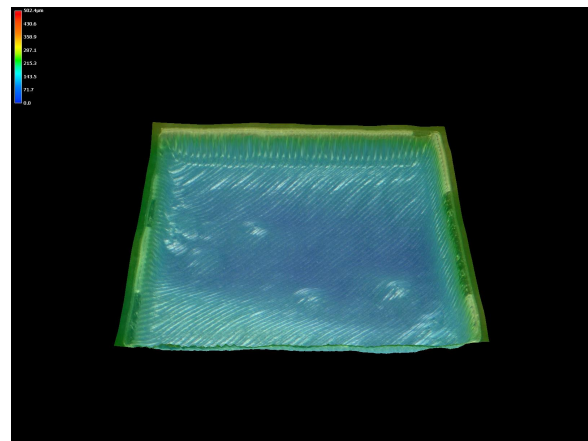Surface Profile square 6
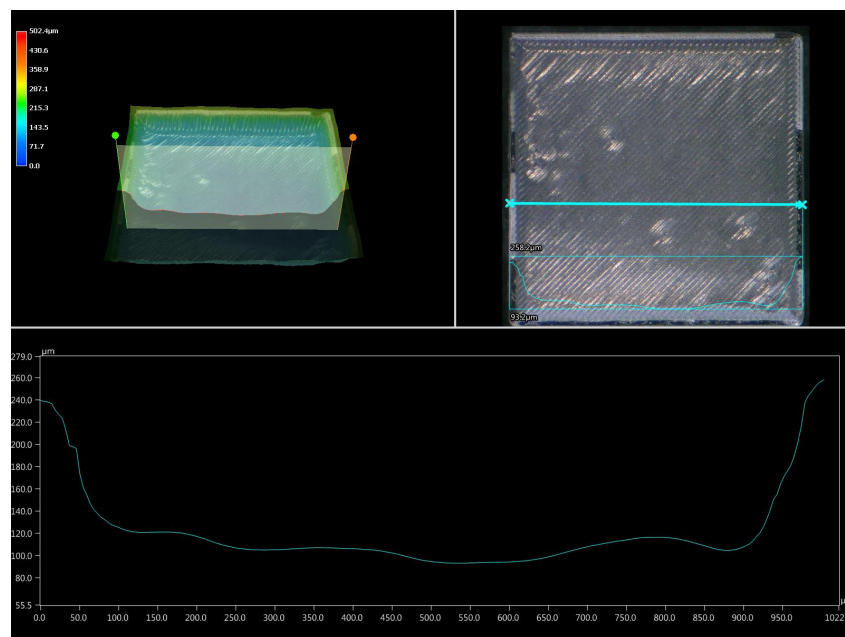
Overview Picture square 7

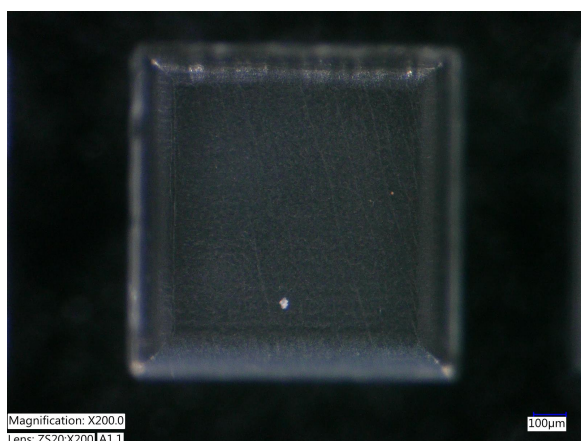3D Heat Map square 7

Surface Profile square 7
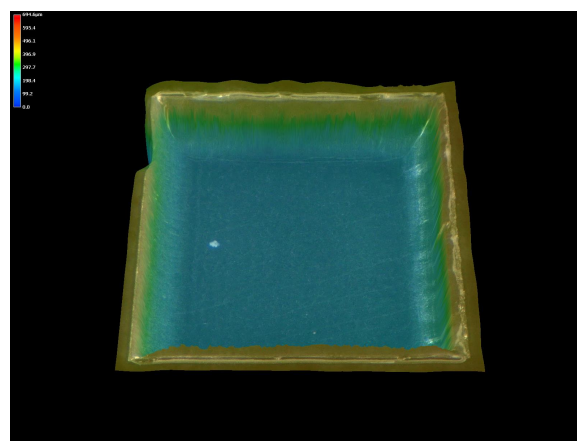
Overview Picture square 8

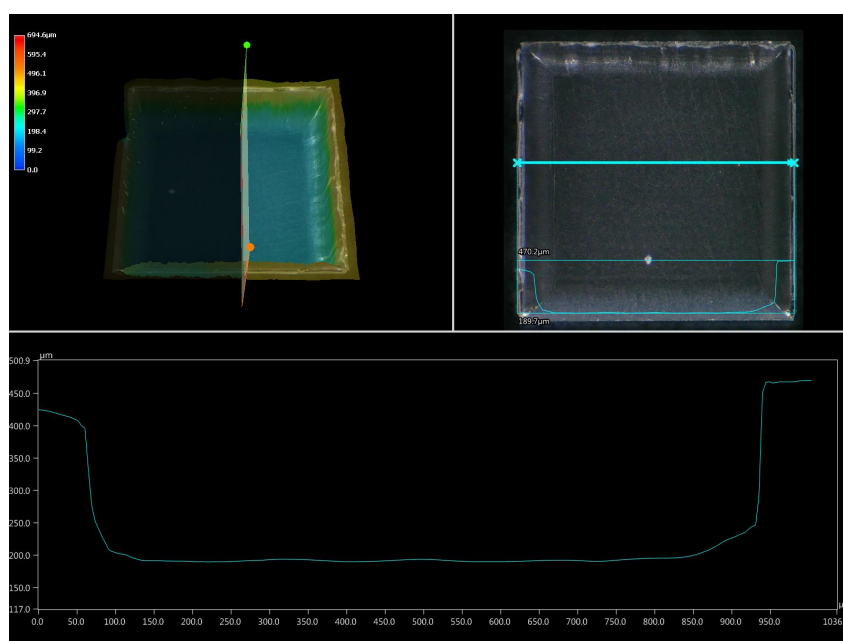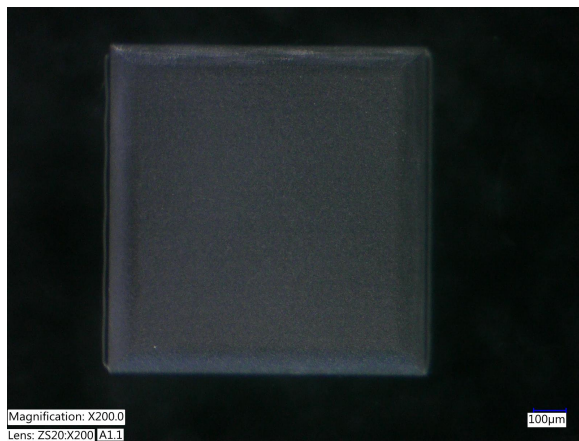3D Heat Map square 8

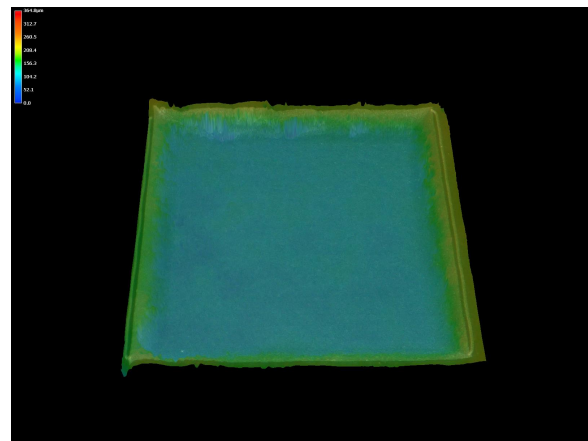Surface Profile square 8

Overview Picture square 9
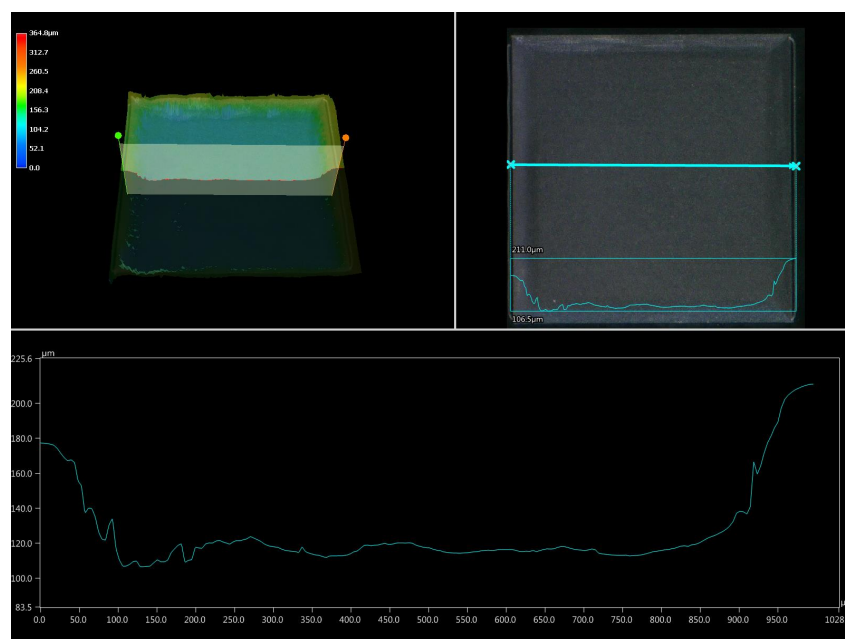

3D Heat Map square 9

Surface Profile square 9

Overview Picture square 10

3D Heat Map square 10

Surface Profile square 10

F.7. Channel circle samples

Settings used for this circular channels are visible in Figure 64.

Sample	Power(%)	Speed(mm/s)	Repetitions(N)	Layers(N)	Layer pitch(mm)	Hatch pitch(mm)	Hatch pattern	Note
Sample J	10	100	4	4	0.075	0.0015	horizontal	Turn sample 180-degree after 2nd layer
Sample F	10	100	4	6	0.075	0.0015	horizontal	Turn sample 180-degree after 3rd layer

Figure 64.: Settings used for circular channel samples

F.8. Channel engraving sweep settings of samples K

Settings used for this channel sweep are visible in Figure 65.

Sample	Power(%)	Speed(mm/s)	Repetitions(N)	Layers(N)	Layer pitch(mm)	Hatch pitch(mm)	Hatch pattern	Note
K1	10	100	4	4	0.075	0.0015	horizontal	Fume extraction OFF
K2	10	100	4	4	0.075	0.0015	horizontal	Fume extraction ON, turn sample 180-degree after 2nd step
K3	10	10	4	4	0.075	0.015	horizontal	Fume extraction ON, turn sample 180-degree after 2nd step

Figure 65.: Settings channel samples K

F.9. Gas exchanger channel settings used

Settings used for the gas exchanger channels are visible in Figure 66.

Sample	Power(%)	Speed(mm/s)	Repetitions(N)	Layers(N)	Layer pitch(mm)	Hatch pitch(mm)	Hatch pattern	Note
Liquid channel	10	100	4	4	0.075	0.0015	horizontal	Turn sample 180-degree after 2nd layer
Gas channel	10	100	4	6	0.075	0.0015	horizontal	Turn sample 180-degree after 3rd layer

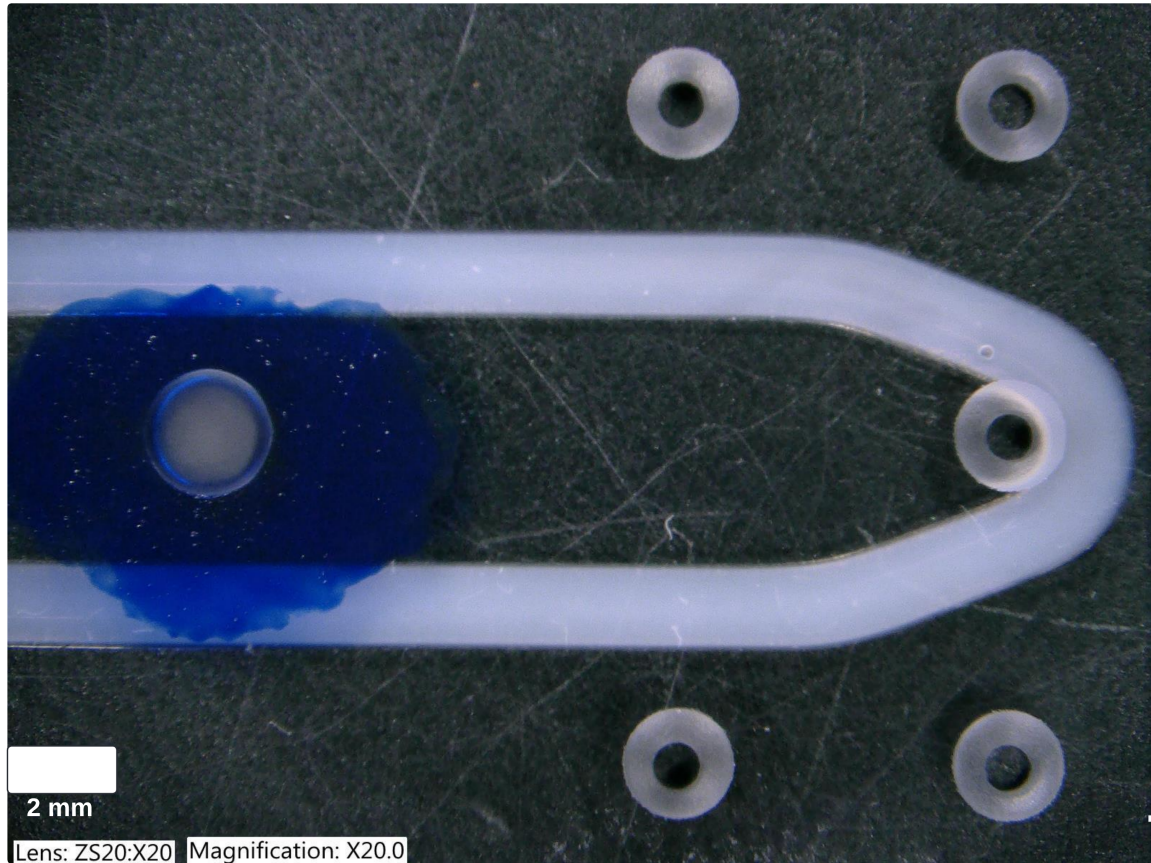Figure 66.: Gas exchanger channels settings

Figure 68.: Micronit chip with blue stained sensor spot hole

F.10. Micronit sensor hole

Settings used for the sensor spot hole are visible in Figure 67. Figure 68 shows the sensor hole on the Micronit chip.

Sample	Power(%)	Speed(mm/s)	Repetitions(N)	Hatch pitch(mm)	Hatch pattern	Layers(N)	Layer pitch(mm)	Note
Sensor hole	15	150	5	0.0015	horizontal	10	0.05	2.14 mm diameter, 10 times lowered by layer pitch

Figure 67.: Sensor hole settings

G. Drawings

G.1. Gas exchanger

The gas exchanger consists of three layers; top glass slide, PDMS membrane layer, bottom glass slide. This section shows their SolidWorks technical drawings with dimensions.

G.1.1. Top layer

Figure 69 shows the dimensions of the top slide.

G.1.2. PDMS membrane layer

Figure 70 shows the dimensions of the PDMS membrane layer.

G.1.3. Bottom layer

Figure 71 shows the dimensions of the bottom layer.

G.2. Alignment tool

Figure 72 shows the dimensions of the 3D printed alignment tool.

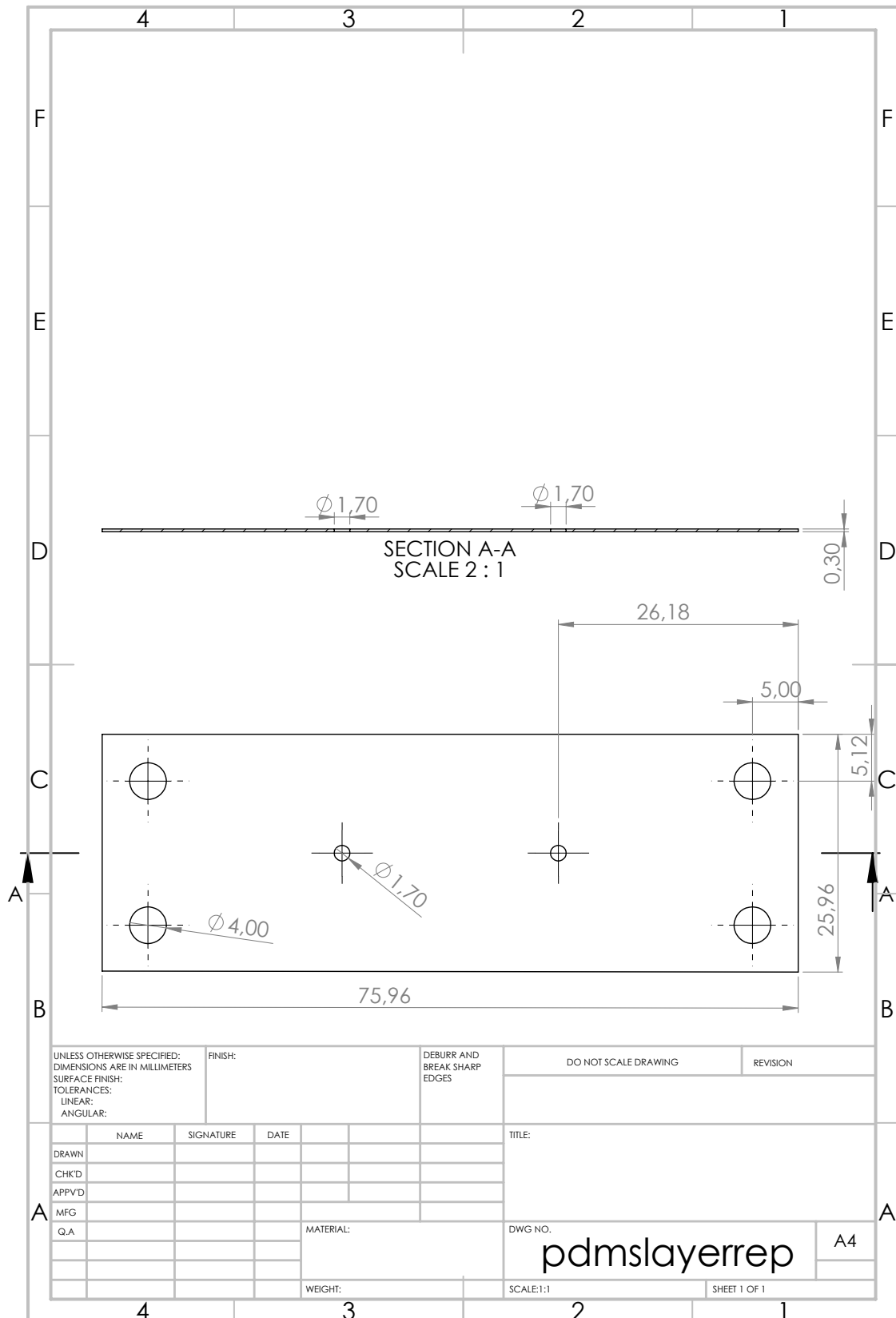Figure 69.: Top slide SolidWorks technical drawing

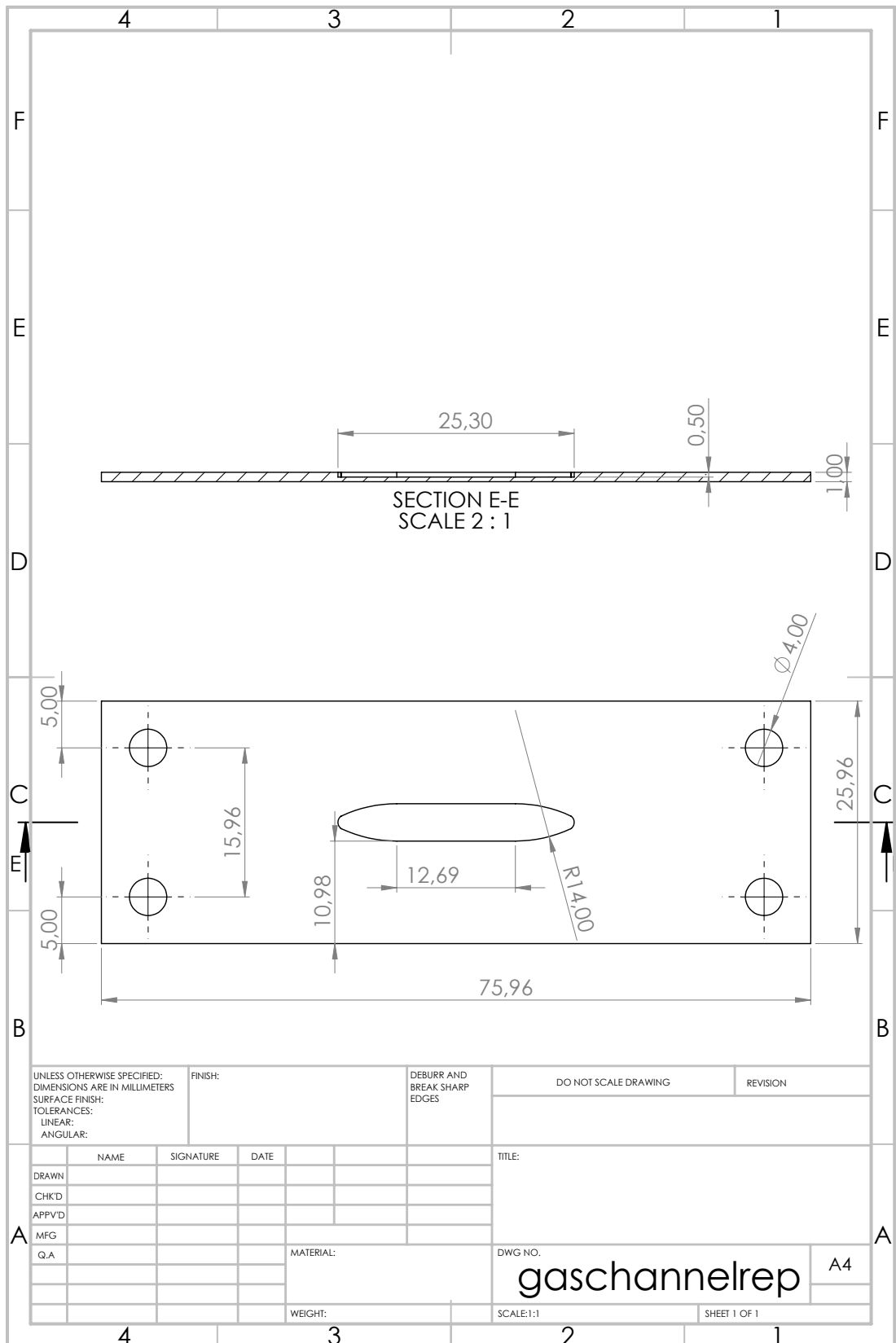Figure 70.: Membrane layer SolidWorks technical drawing

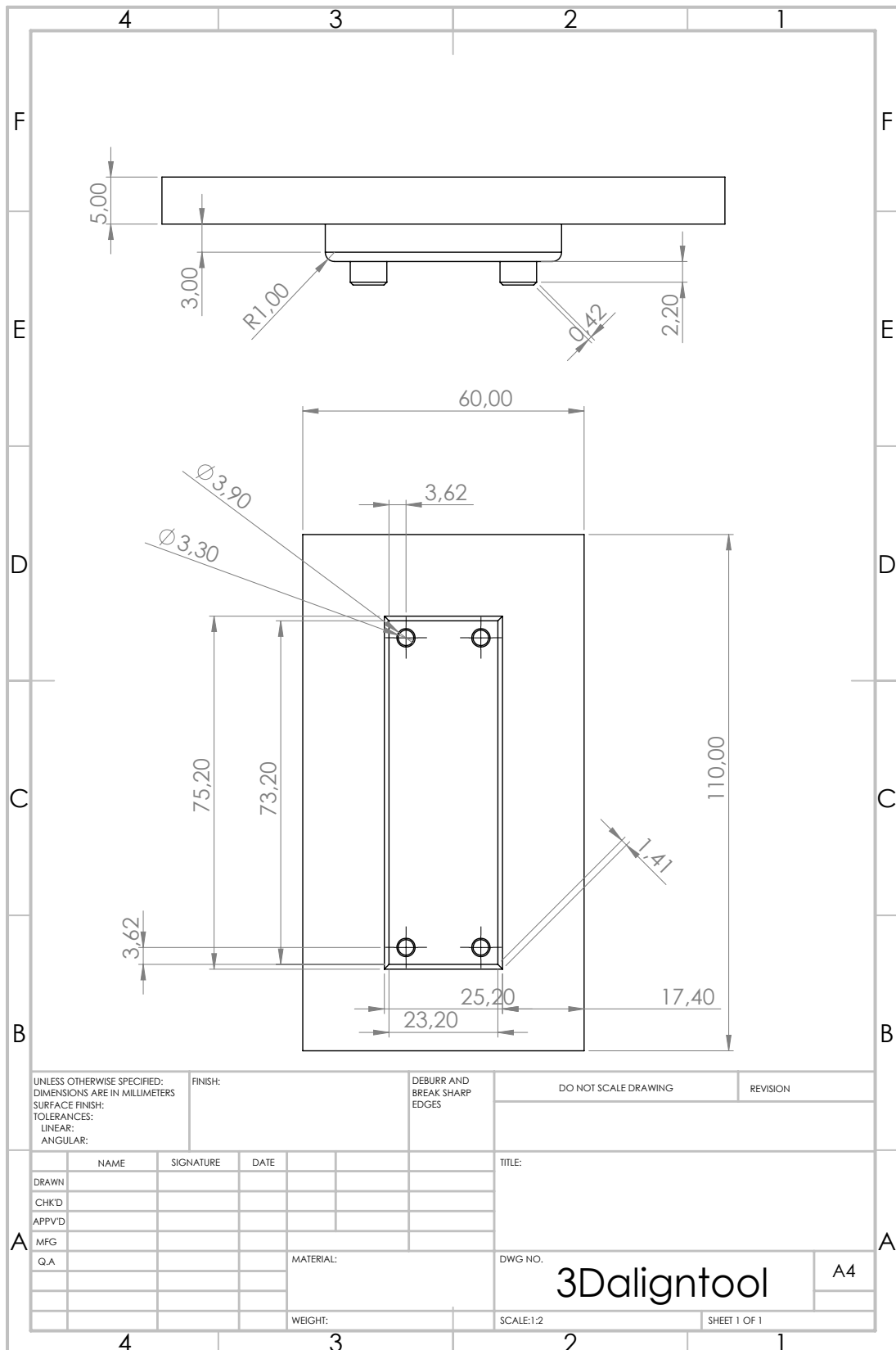Figure 71.: Bottom layer SolidWorks technical drawing

Figure 72.: 3D printed alignment tool SolidWorks technical drawing

Common Issues and Mitigation Strategies in Fs Laser Fabrication

Throughout the laser machining process, several common issues were encountered, each requiring specific mitigation strategies:

- **Cracking of glass:** Cracking of the glass substrate predominantly occurs due to a combination of excessively low speed and overly high power settings. Although increasing speed and lowering power may seem like a solution, it introduces a trade-off. High speed can compromise quality due to imprecise lens movement, resulting in shortcuts in certain parts of the trajectory. Conversely, low power reduces penetration depth, leading to extended ablation times, sometimes spanning several hours for a small area.

- **Debris clogging:** The presence of small glass residues in the microstructure can negatively impact surface smoothness by rebonding to the substrate during ablation. To counteract this, a fume extraction system, such as BOFA Oracle, is utilized to create airflow over the workpiece, as depicted in Figure **??**. This issue plays a larger role at smaller and deeper hatches since the debris build-up is higher and is harder to be blown away than at shallow and wide hatches. Additionally, a pressure pump aids in blowing away debris.

- **Accuracy loss when out of focus:** The LS-Lab micromachining setup experiences accuracy loss when the laser is emitted too far from the focus point(40x40mm). To mitigate this issue, cut files can be divided into separate sections using event prompts. This ensures the stage moves to the correct position before cutting sections that were otherwise out-of-focus, enhancing accuracy.

H. COMSOL settings and sensitivity analyses

Having 5 mL/min of gas flow, the initially planned gas flow rate, is also modeled with COMSOL. The gas exchanger shows no negative sensitivity or influence to the change in gas flow rate to 40 mL/min. This can be concluded from Figure 73, showing an identical graph to the graph in the article with a gas flow rate of 40 mL/min.
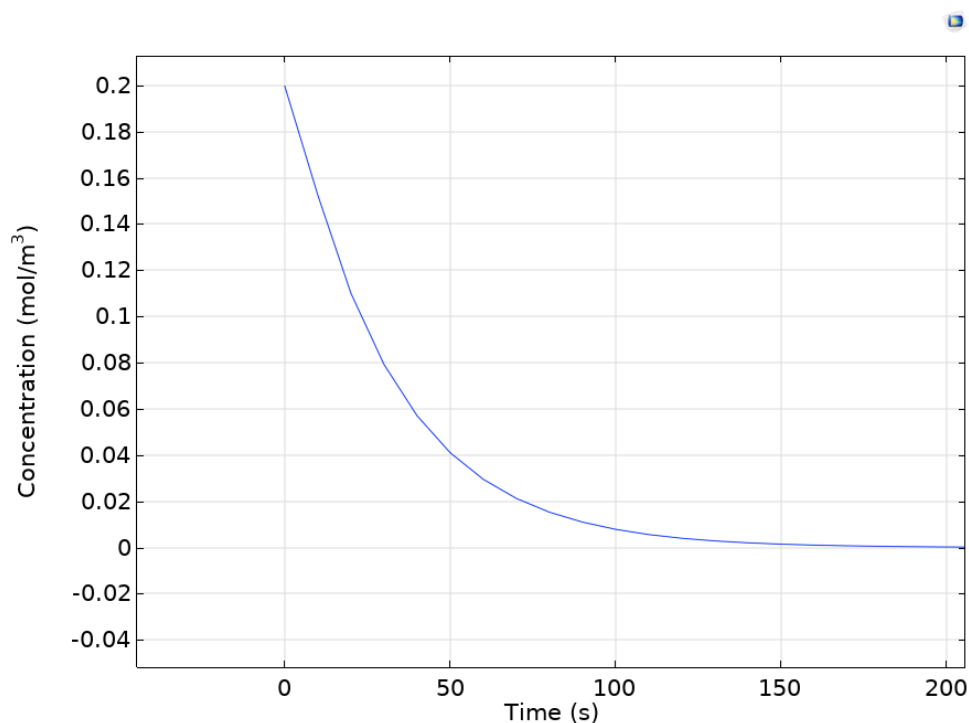

Figure 73.: Average surface concentration profile of the gas exchanger liquid outlet using a gas flow rate of 5 mL/min.

If the membrane gets deformed more than expected, blocking the gas channel, the following COMSOL model examined the effects on the performance of the oxygen concentration regulation. To simplify the model of a very deformed membrane state, the gas channel is set to a uniform height of only 100 μm and the membrane layer kept the original thickness and the liquid channel to 700 μm, since this side would be bloated if the gas side would be made smaller. The result shows a difference compared to the other models. It takes more time to reach within 10% and 1% of

the set value compared to the other models. It takes approximately 262 seconds to reach within 10% of the target value, and 530 seconds to reach within 1% of the target value. The used geometry is visible in Figure 74 and the concentration profile of this model is visible in Figure 75.
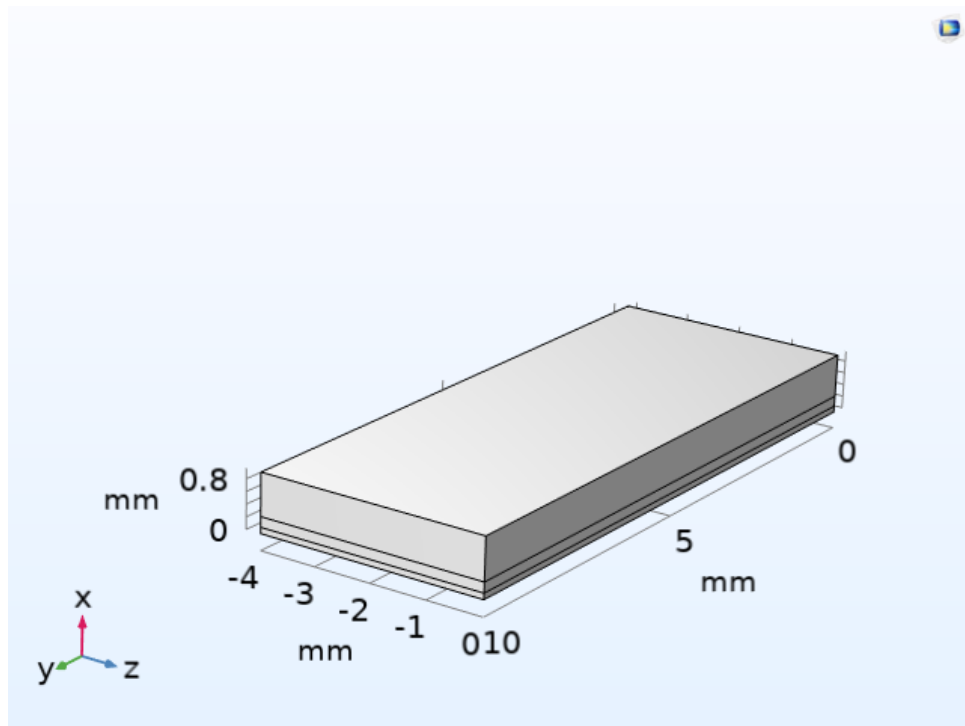

Figure 74.: The geometry for the deformed gas exchanger simulation consists of three layers: the top layer is the liquid channel, the middle layer is the PDMS membrane sheet, and the bottom layer is the gas channel.
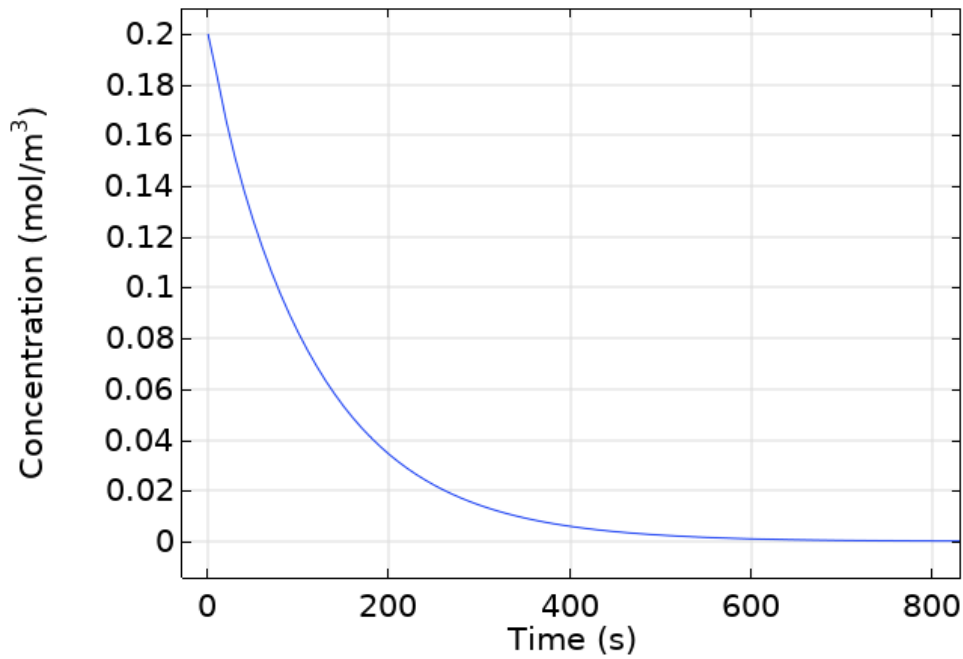
Figure 75.: Average surface concentration profile of the deformed gas exchanger's liquid outlet

H.1. COMSOL simulation parameters

The following COMSOL simulation parameter values are used in the models.

COMSOL parameters used in the gas exchanger simulation in the article:

```
w_medchannel 4[mm] "Width medium channel"
w_gaschannel 4[mm] "Width gas channel"
v_med Q_med/A_medchannel "Medium Flow velocity"
v_gas Q_gas/A_gaschannel "Gas channel flow velocity"
Q_med "(35e-9/60) [m^3/s]" "Medium flow rate"
Q_gas "(40e-6/60) [m^3/s]" "Gas flow rate"
mu_med "0.958 [mPa*s]" "dynamic viscosity cell medium"
h_pdms 170[um] "Height PDMS membrane"
h_medchannel 300[um] "Height medium channel"
h_gaschannel 500[um] "Height gas channel"
D_o2pdms 3.25E-9[m^2/s] "Diffusion coefficient PDMS"
D_o2n2 "3.472e-5 [m^2/s]" "Diffusion coefficient nitrogen"
D_o2med "2.69e-9 [m^2 /s]" "Diffusion coefficient medium"
c_N2ini "0 [mol/m^3]" "initial o2 conc N2"
c_medsat "0.2 [mol/m^3]" "saturated oxygen concentration, 20 degrees"
```

```
A_medchannel w_medchannel*h_medchannel "Medium channel area"
A_gaschannel h_gaschannel*w_gaschannel "Gas channel area"
```

COMSOL parameters used in the initial COMSOL simulation
using a gas flow rate of 5 mL/min:

```
w_medchannel 4[mm] "Width medium channel"
w_gaschannel 4[mm] "Width gas channel"
v_med Q_med/A_medchannel "Medium Flow velocity"
v_gas Q_gas/A_gaschannel "Gas channel flow velocity"
Q_med "(35e-9/60) [m^3/s]" "Medium flow rate"
Q_gas "(5e-6/60) [m^3/s]" "Gas flow rate"
mu_med "0.958 [mPa*s]" "dynamic viscosity cell medium"
h_pdms 170[um] "Height PDMS membrane"
h_medchannel 300[um] "Height medium channel"
h_gaschannel 500[um] "Height gas channel"
D_o2pdms 3.25E-9[m^2/s] "Diffusion coefficient PDMS"
D_o2n2 "3.472e-5 [m^2/s]" "Diffusion coefficient nitrogen"
D_o2med "2.69e-9 [m^2 /s]" "Diffusion coefficient medium"
c_N2ini "0 [mol/m^3]" "initial o2 conc N2"
c_medsat "0.2 [mol/m^3]" "saturated oxygen concentration, 20 degrees"
A_medchannel w_medchannel*h_medchannel "Medium channel area"
A_gaschannel h_gaschannel*w_gaschannel "Gas channel area"
```

COMSOL parameters used in the deformed COMSOL simulation with
different gas and liquid channel heights:

```
w_medchannel 4[mm] "Width medium channel"
w_gaschannel 4[mm] "Width gas channel"
v_med Q_med/A_medchannel "Medium Flow velocity"
v_gas Q_gas/A_gaschannel "Gas channel flow velocity"
Q_med "(35e-9/60) [m^3/s]" "Medium flow rate"
Q_gas "(40e-6/60) [m^3/s]" "Gas flow rate"
mu_med "0.958 [mPa*s]" "dynamic viscosity cell medium"
h_pdms 170[um] "Height PDMS membrane"
h_medchannel 700[um] "Height medium channel"
h_gaschannel 100[um] "Height gas channel"
D_o2pdms 3.25E-9[m^2/s] "Diffusion coefficient PDMS"
D_o2n2 "3.472e-5 [m^2/s]" "Diffusion coefficient nitrogen"
```

```
D_o2med "2.69e-9 [m^2 /s]" "Diffusion coefficient medium"
c_N2ini "0 [mol/m^3]" "initial o2 conc N2"
c_medsat "0.2 [mol/m^3]" "saturated oxygen concentration, 20 degrees"
A_medchannel w_medchannel*h_medchannel "Medium channel area"
A_gaschannel h_gaschannel*w_gaschannel "Gas channel area"
```

The raw data from the COMSOL simulations is not included in this document due to its extensive and detailed nature. However, it is available upon request. Interested readers can obtain the data by contacting the author via email at jelle.hs@gmail.com.

I. Needle gauge separation and gluing connection

I.1. Needle gauge separation

To establish a connection between the liquid port of the gas exchanger and a PEEK tubing, an off-the-shelf metal elbow tubing could have been a viable option. However, due to the constraints of small dimensions, suitable metal elbow pieces are not readily available. As an alternative, the interior of a needle gauge, a small hollow tube designed for liquid flow, can serve this purpose by linking the gas exchanger's liquid port (which is also a PEEK tubing) to the other PEEK tubing. Both tubes have an inner diameter of 0.25 mm. A 32G yellow needle gauge is suitable for this application because its outer diameter closely matches the inner diameter of the PEEK tubing. Testing was also conducted with a lavender 30G needle, but it did not fit, even under pressure. The needle gauge dimensions are illustrated in Figure 76.

To remove the housing of the needle gauge, a minor operation is required. Separating the needle gauge's inner metal tubing from the plastic housing can be achieved by applying pressure to the glue connection between the tubing and the housing, using pliers. Carefully cutting the glue connection at an angle without exerting pressure on the metal tubing is crucial to prevent blockage or damage to the tubing. When performed correctly, this process yields a plastic housing and a thin metal tubing. The plier and resulting separation are visible in Figure 77.

I.2. Gluing connection

Excessive clearance between the needle gauge's interior metal tubing and the PEEK tubing resulted in leakage during perfusion. To solve this issue, Super Glue (specifically, Loctite Super Glue 3 Precision) was employed to seal the leaks. Figure 78 depicts a microscope image captured after the application of the glue. Following this adjustment, no further leakages occurred during perfusion.

Precision Dispense Tips

PRECISION STAINLESS STEEL TIPS

Gauge		Color	ID		OD	
			mm	inch	mm	inch
14		Olive	1.54	0.060	1.83	0.072
15		Amber	1.36	0.053	1.65	0.065
18		Green	0.84	0.033	1.27	0.050
20		Pink	0.61	0.024	0.91	0.036
21		Purple	0.51	0.020	0.82	0.032
22		Blue	0.41	0.016	0.72	0.028
23		Orange	0.33	0.013	0.65	0.025
25		Red	0.25	0.010	0.52	0.020
27		Clear	0.20	0.008	0.42	0.016
30		Lavender	0.15	0.006	0.31	0.012
32		Yellow	0.10	0.004	0.24	0.009

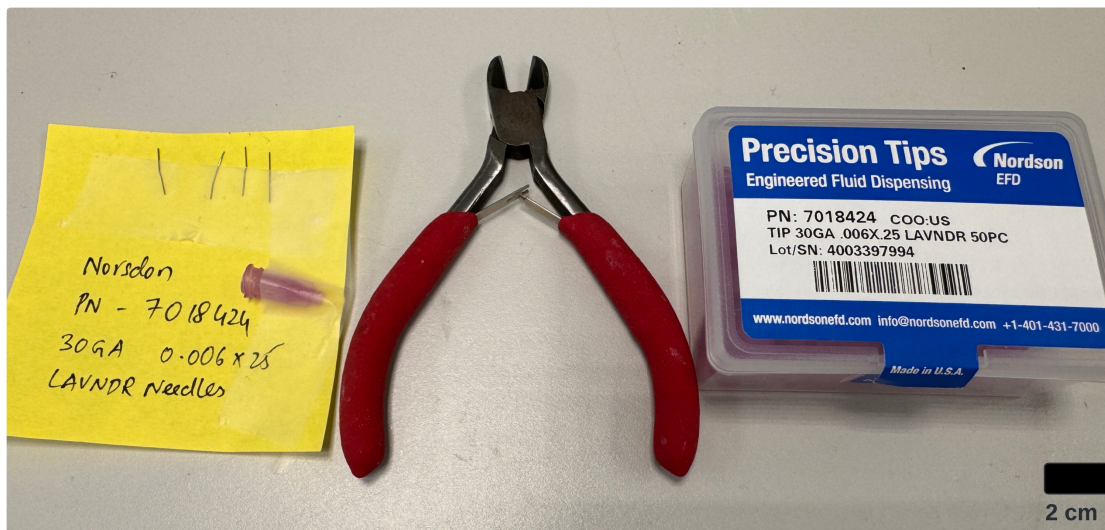Figure 76.: Needle gauge dimensions, adjusted from [38]

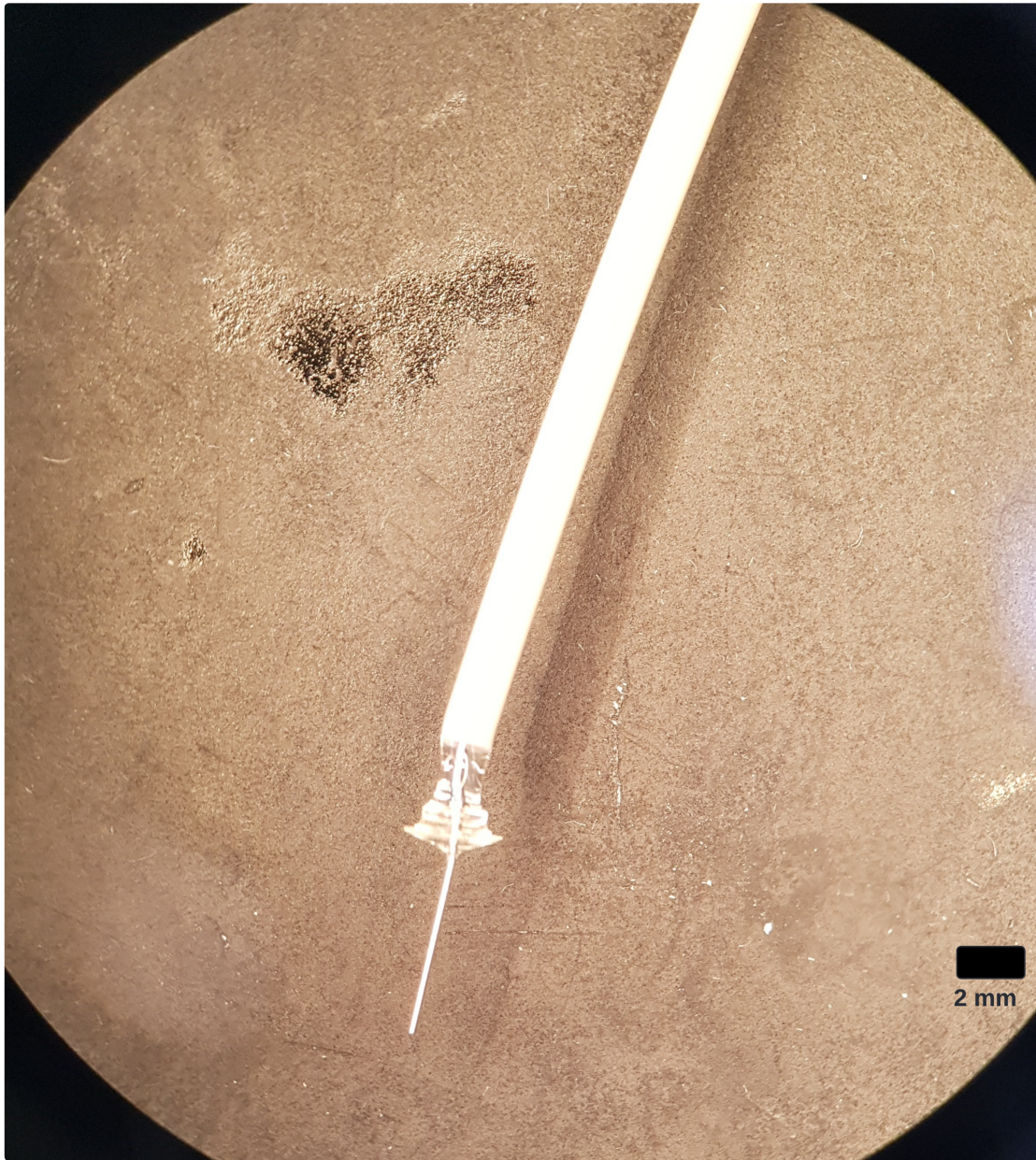Figure 77.: Needle gauge separation, received by M. K. Ghatkesar (2024) [22]

Figure 78.: Microscope image of glue bonding the needle gauge's interior metal tubing into the PEEK tubing

J. Factors Influencing Laser Result Quality

The following figure demonstrates a cause-effect (Ishikawa) diagram of the determinants that influence the laser result quality.
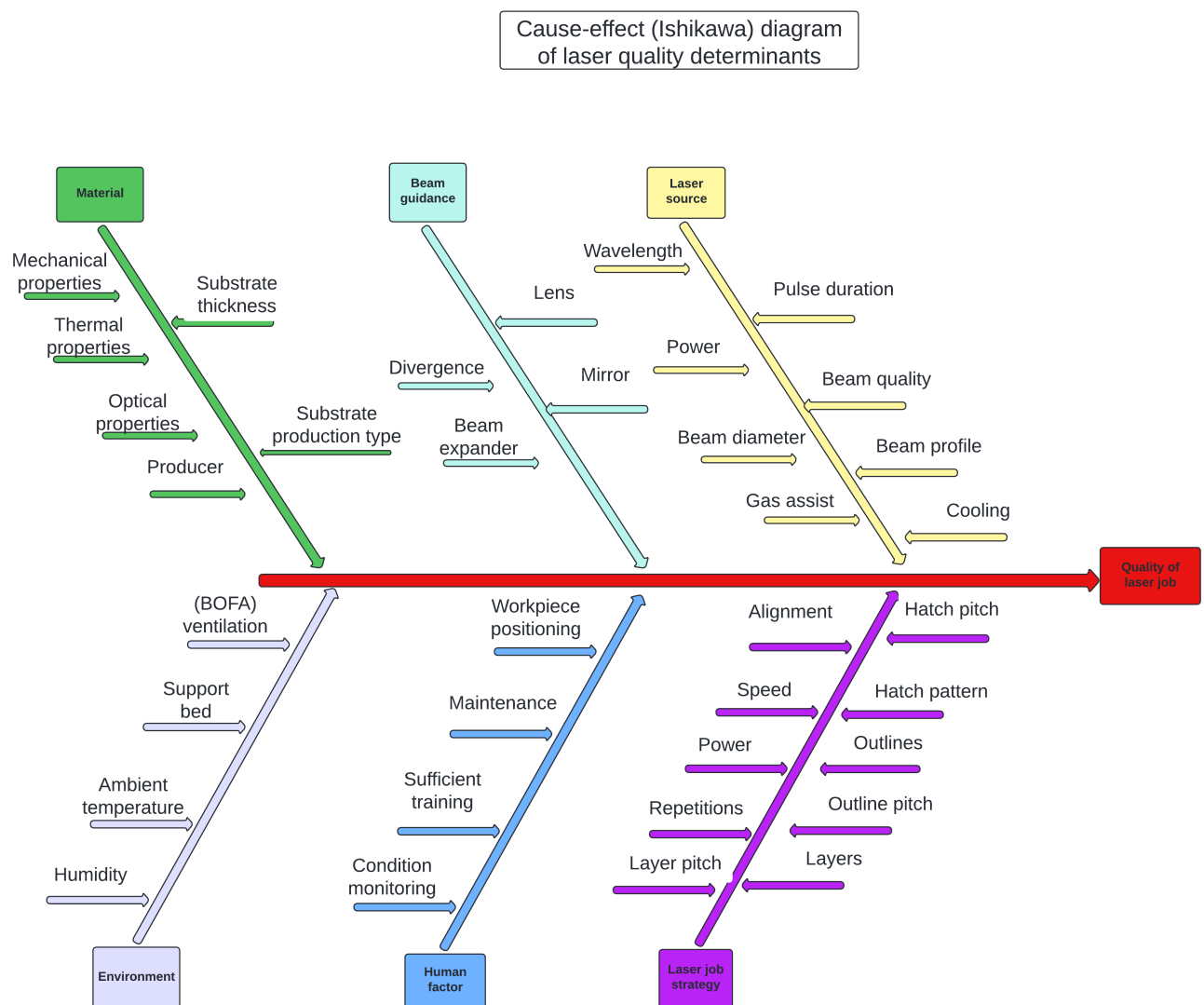

Figure 79.: Cause-effect (Ishikawa) diagram of laser quality determinants

K. Calibration of Presens Sensor Spot

This chapter details the calibration procedures and outcomes.

To begin the calibration, a 100 mL glass bottle is employed, with a 5 mm sensor spot from Presens Precision Sensing GmbH affixed to the inner wall using 2 ($\pm$0.5) μL of silicone glue (Wacker Elastosil E43). The process begins after allowing a day for drying. Subsequently, 80 mL of Milli-Q water is added to the bottle, ensuring the sensor is fully submerged and in close contact with the water. To enhance diffusion time and ensure precise measurements, a temperature probe(Pt100, PreSens Precision Sensing GmbH) and a gas tube with a diffuser stone are utilized, generating small bubbles with increased contact area. Refer to Figure 80 for a visual representation of the setup. It's noteworthy that a magnetic stirring plate should be avoided to prevent temperature fluctuations, as temperature plays a crucial role in oxygen saturation measurement.

A two-point calibration is conducted, aiming for both 0% oxygen (cal0) and 100% air saturation (cal100). A gas flow rate of 500 mL/min or higher is employed for calibration, using nitrogen gas flow for 0% oxygen and airflow for 100% air saturation. Throughout the calibration process, a weather station is utilized to monitor atmospheric pressure, as this parameter influences the maximum solubility of oxygen in water and, consequently, air saturation levels. Figure 81 illustrates the resulting calibration values, all falling within the calibration limits specified by Presens Precision Sensing GmbH. The measured atmospheric pressure is recorded as 986 mbar. Finally, the temperature, atmospheric pressure, amplitude, and phase data are entered into the Presens software.

The 2 mm sensor spots have the same values for the amplitude and phase bounds according to their Presens manual. Due to time restrictions, the 2 mm sensor spots are expected to have the same sensitivity and are not calibrated.
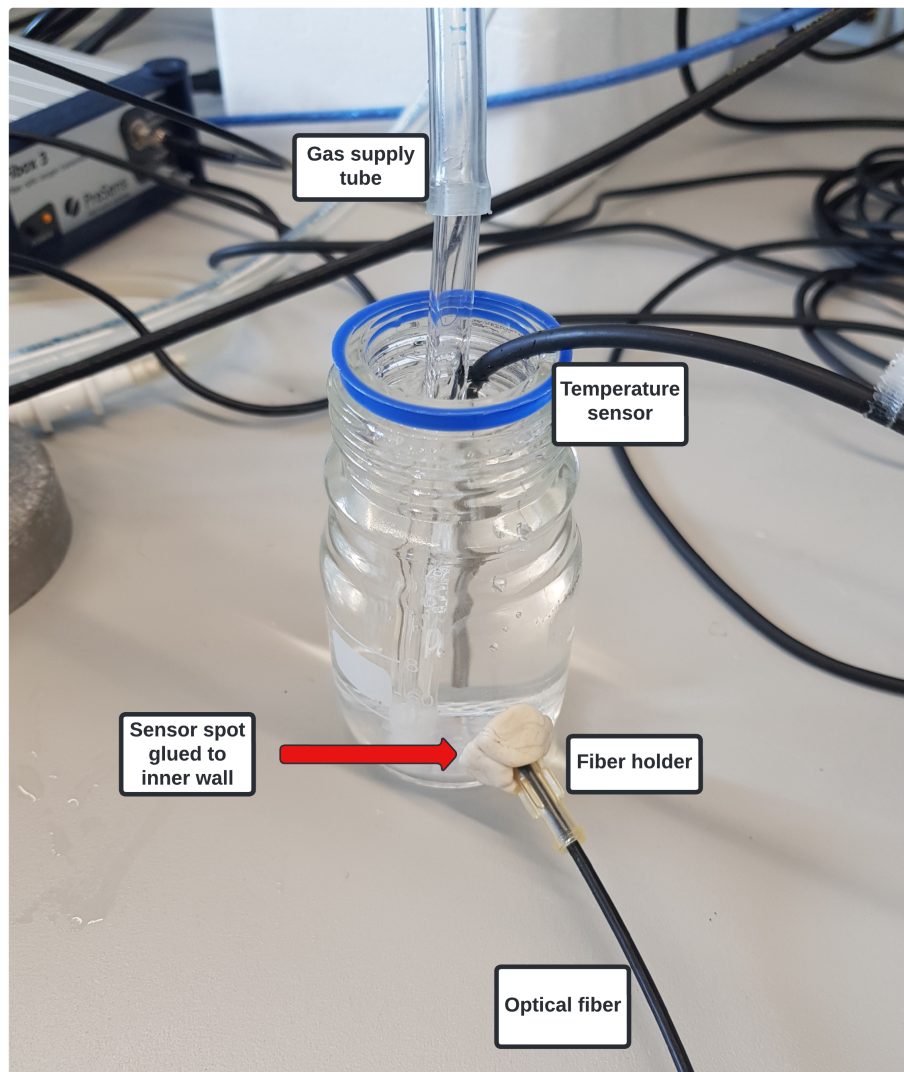
Figure 80.: Calibration setup

Calibration	Cal0	Cal100	Calibration limits
Temperature	18.7C	20.1C	18.0C-22.0C
Amplitude	142827	41028	
Phase	60.90	28.29	
Calibration limits	58.00-62.00	25.00-29.00	

Figure 81.: Calibration values, within the bounds for reliable sensor values

L. Gas mixing compositions from Bronkhorst OEM gas supply

Totale flow	200 ml/min	(5-20 % O2)		%CO2	5
	400 ml/min	(0-4% O2)			

% O2	AIR	N2	CO2	Total
20,95				
20	191	-1	10	200,0
19	181	9	10	200,0
18	172	18	10	200,0
17	162	28	10	200,0
16	153	37	10	200,0
15	143	47	10	200,0
14	134	56	10	200,0
13	124	66	10	200,0
12	115	75	10	200,0
11	105	85	10	200,0
10	95	95	10	200,0
9	86	104	10	200,0
8	76	114	10	200,0
7	67	123	10	200,0
6	57	133	10	200,0
5	48	142	10	200,0
4	76	304	20	400,0
3	57	323	20	400,0
2	38	342	20	400,0
1	19	361	20	400,0
0	0	380	20	400,0

Figure 82.: Gas mixing ratios for the Bronkhorst OEM gas supply system

Figure 83.: The Bronkhorst OEM gas supply system

M. Slope and Width Estimation Through Holes

Both through hole fabrication methods exhibit a noticeable slope from the top edge to the bottom, influenced by factors such as glass debris and variations in result quality. To quantify this slope, a triangular region is defined on both edges of each hole to determine the x and y coordinates of the top and bottom points. The slope values of both edges are then averaged to derive an average slope value, known as the height-to-width ratio. Both figures with the triangles are depicted in Figure 84 and Figure 85.

The slope from the top edge to the bottom of both edges that was estimated using perimeter cutting resulted in an average slope of:

$$\text{Average Slope}_{\text{perimeter}} = \frac{\left|\frac{1075-25}{15.27-80}\right| + \left|\frac{25-1000}{1550-1940}\right|}{2} = \frac{(16.22+2.5)}{2} = 9.36\text{m/m}. \quad \text{(M.1)}$$

In comparison, the area hatching method yielded a slope of:

$$\text{Average Slope}_{\text{area hatching}} = \frac{\left|\frac{990-10}{15.64-350}\right| + \left|\frac{10-1000}{1600-1839}\right|}{2} = (2.9+4.1) = 3.5\text{m/m}. \quad \text{(M.2)}$$

The significantly higher slope obtained from the perimeter cutting method suggests that the fabricated hole exhibits higher quality and experiences a less gradual decrease in slope along its length compared to the area hatching method.

By considering the x-coordinates of the red triangles, we can estimate the width of the hole. The perimeter cutting method yields a width of 1470 µm (1550 - 80), while the area hatching method provides a width of 1250 µm (1600 - 350).
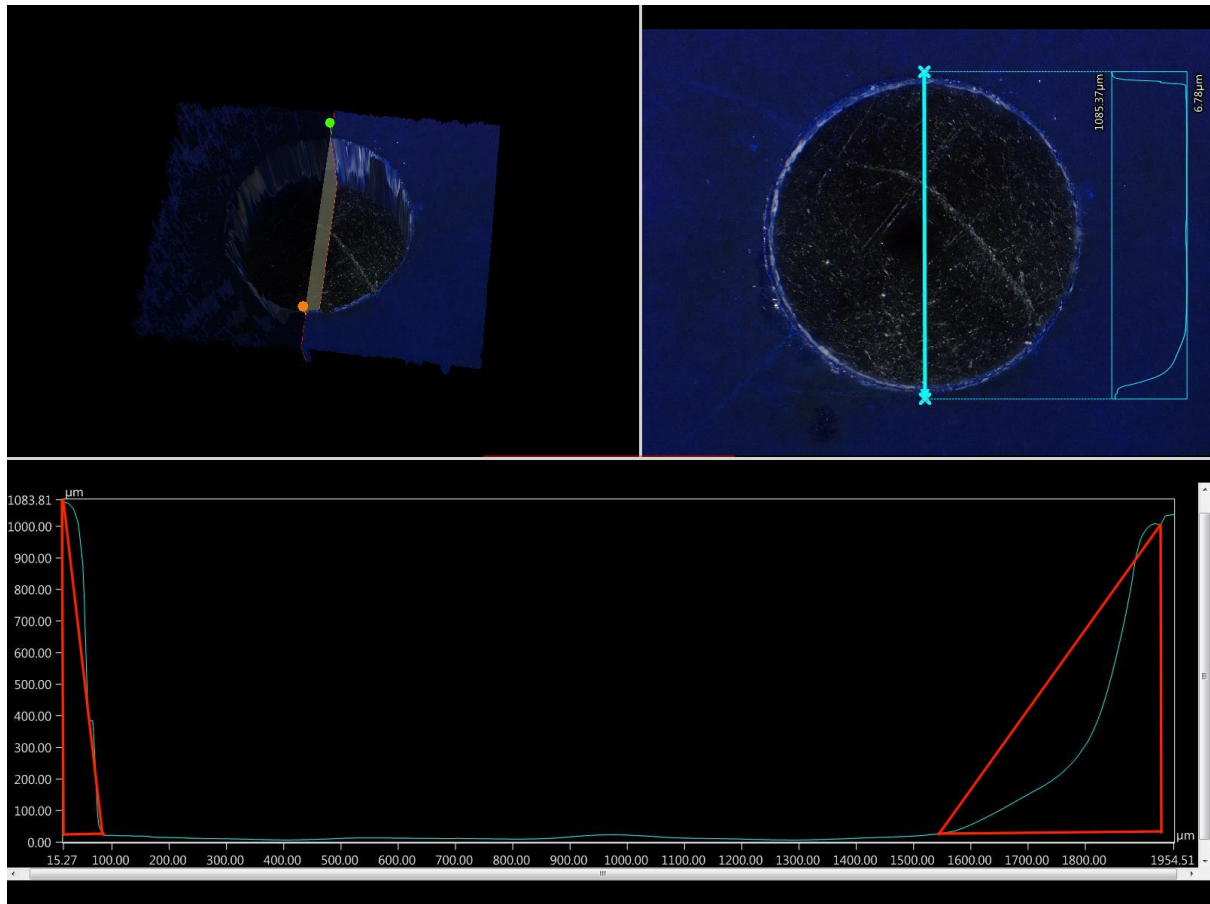
Figure 84.: Slope estimation of a through hole using perimeter cutting, with in red the estimation triangles
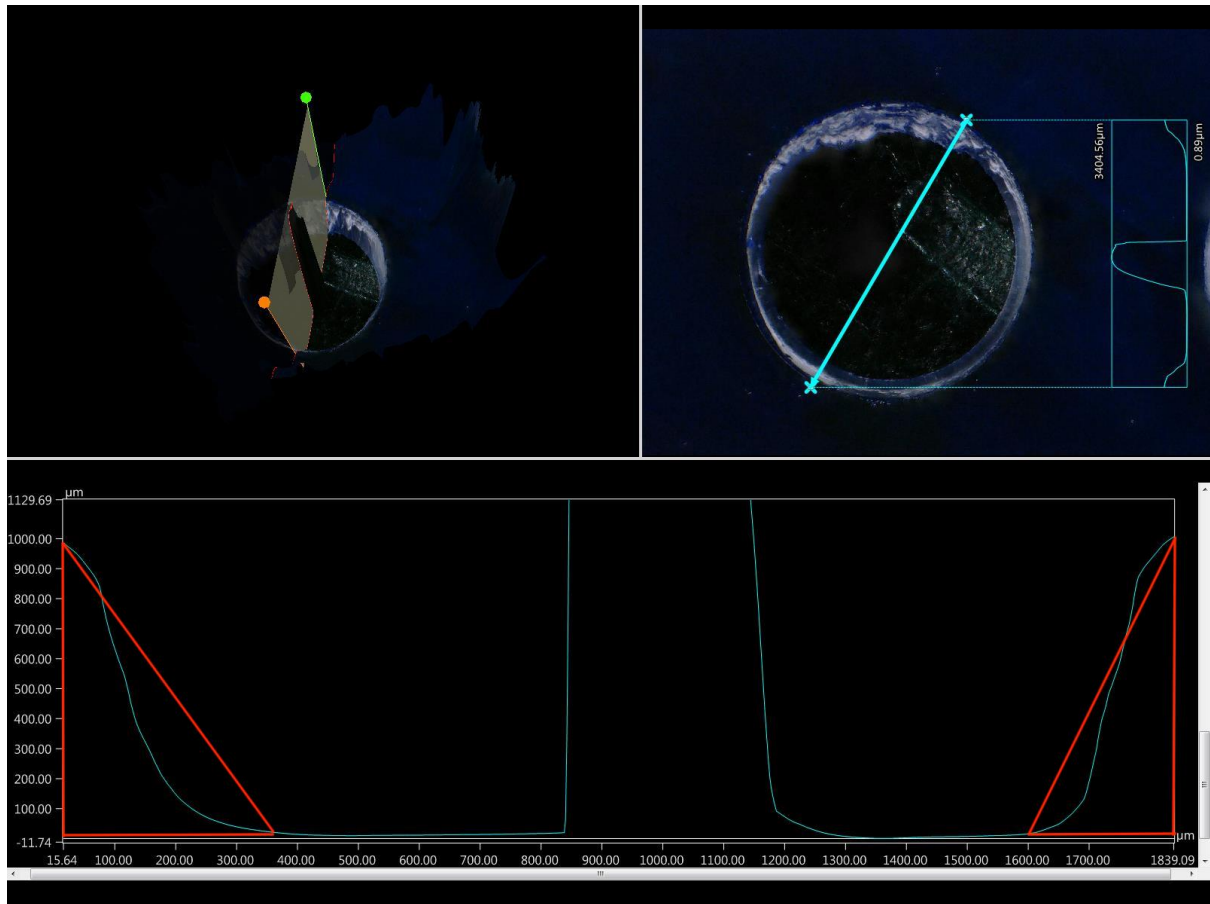
Figure 85.: Slope estimation of a through hole using area hatching, with in red the estimation triangles

N. Sensor spot height and diameter characterization

This chapter shows the result of the sensor spot height and radius measurement using the Keyence digital microscope. This characterization is essential for determining the dimensions needed for the sensor spot hole, being fabricated into the Micronit glass slide.

Figure 86 shows the sensor spot top view, including the radius measurement. The radius is estimated to be 985 μm. The height of the sensor spot is measured to be 220.9 μm, as visible in figure 87.
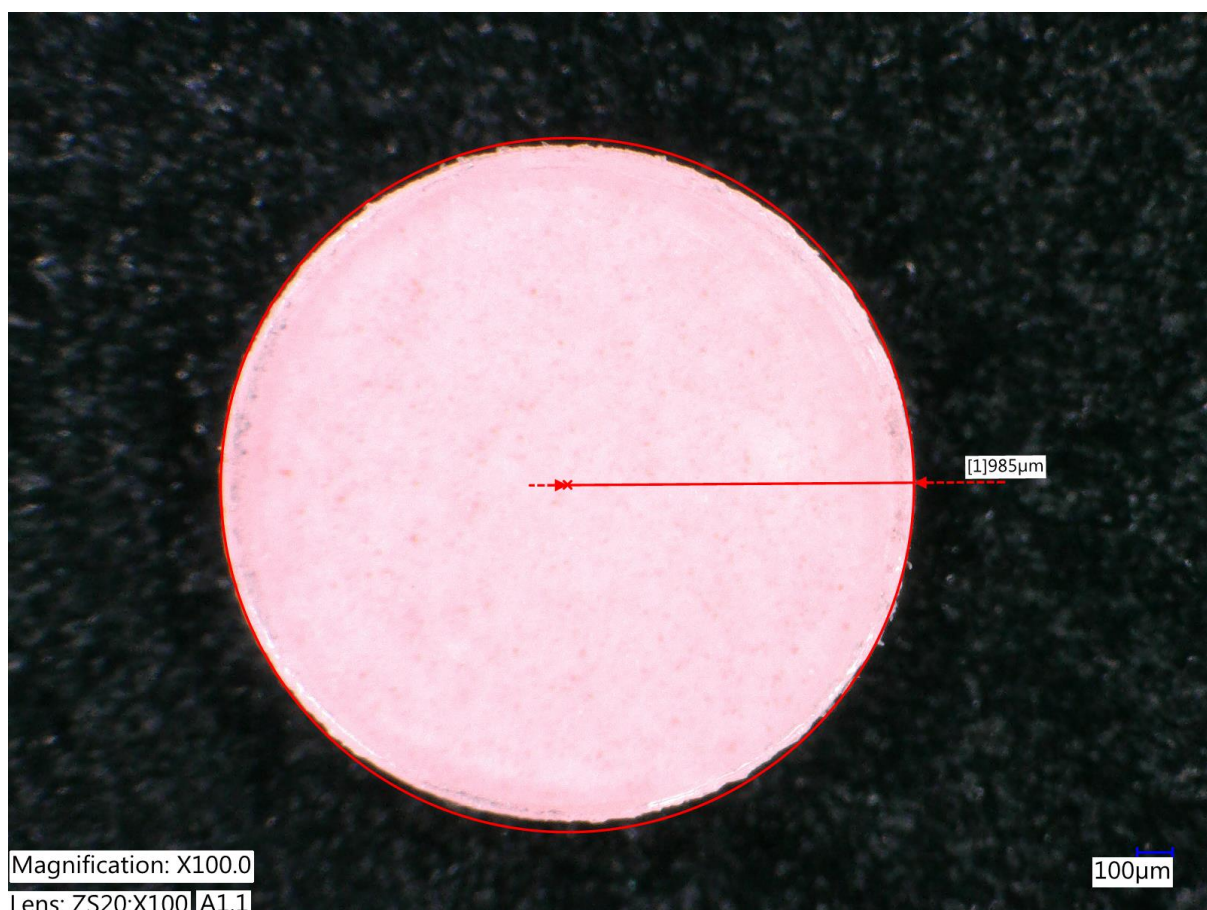
Figure 86.: Sensor spot radius measurement
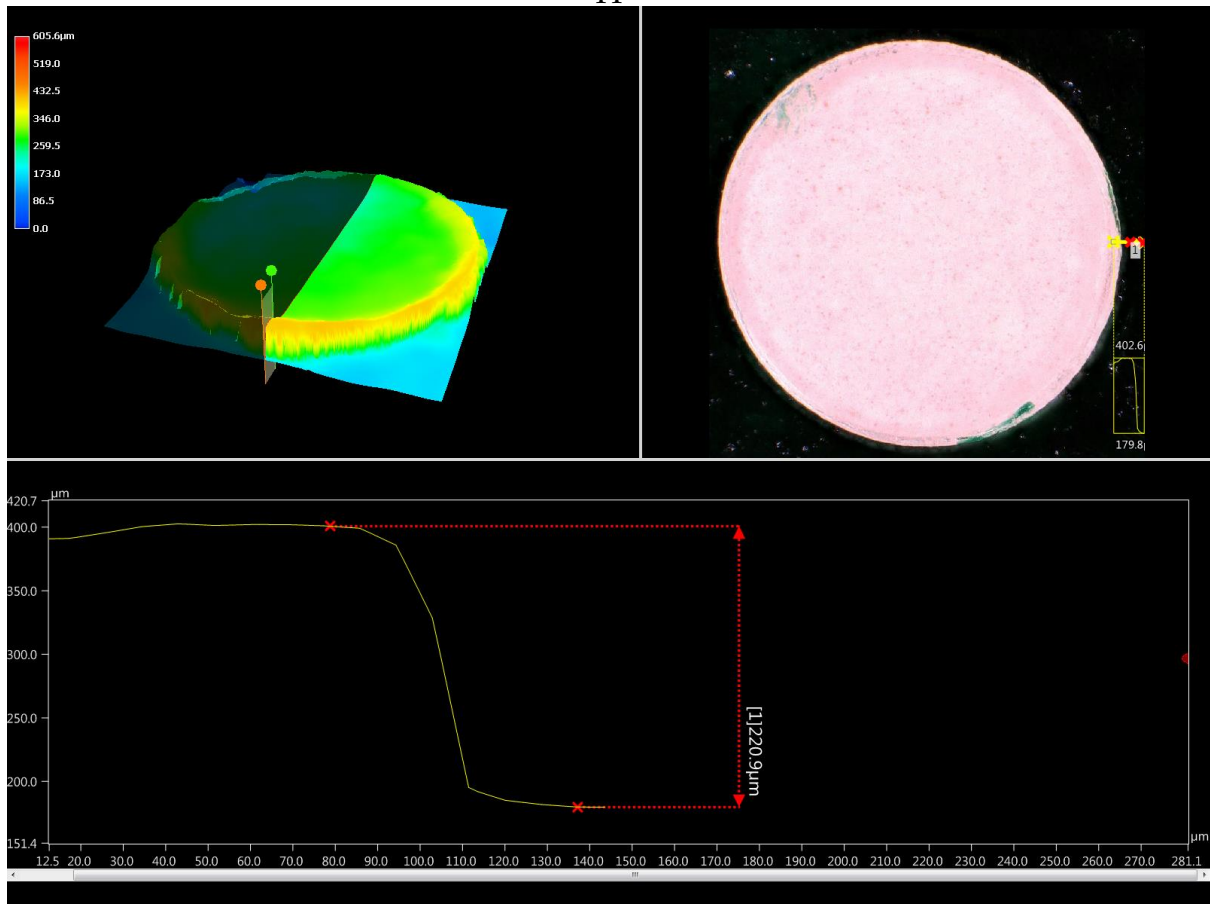
Figure 87.: Sensor spot surface profile, showing a height measurement

O. Equilibrium determination

Both Experiment 1 and Experiment 2 are checked if a steady state in the air saturation is reached, recognizable by a slope %/ min of 0. The slope is calculated for both Experiments in the section where $Q = 175\mu L/$ min is used since this showed the most constant horizontal line behavior. Slope $= (dy/dx)$ for Experiment 1 is calculated as:

$$\text{Slope} = \frac{(8.488 - 8.546)}{(95.016 - 100.849)} = 0.0099\%/min.$$

and for Experiment 2:

$$\text{Slope} = \frac{(1.169 - 1.068)}{(72.022 - 77.855)} = -0.0017\%/min.$$

The used data points and the graph section having $Q = 175\mu L/$ min is shown in Figures 88 and 89.

Figure 88.: Steady state determination in Experiment 1

Figure 89.: Steady state air saturation determination in Experiment 2

P. Video of gas flow reduction system

To watch the gas flow reduction video, please click on the following link:
https://youtu.be/tiVsdumcTCw.

Bibliography

[1]

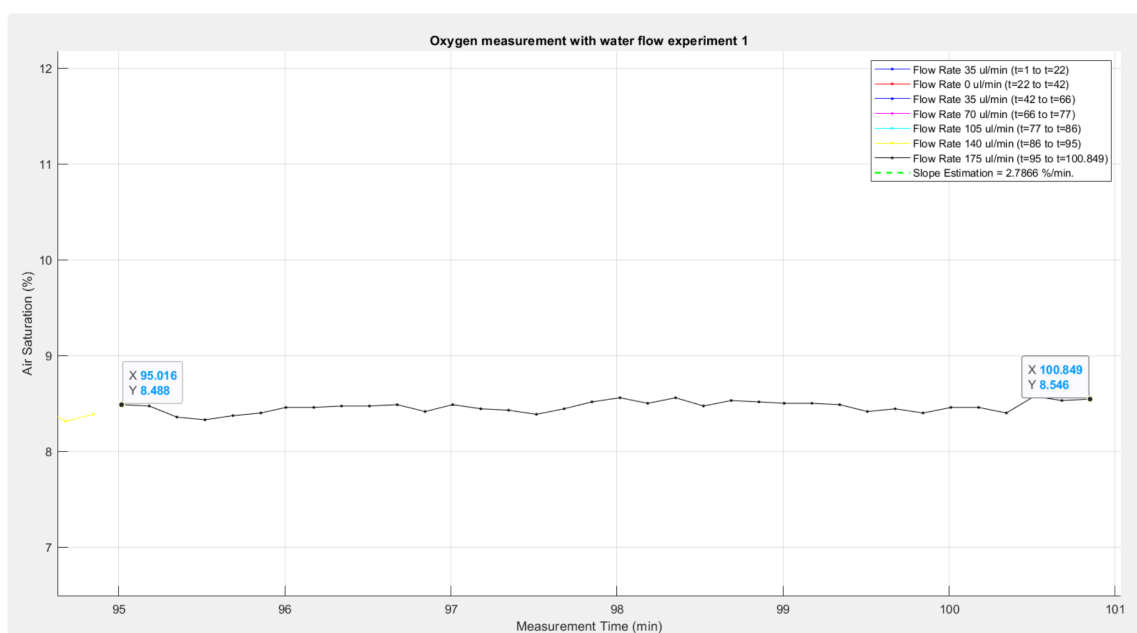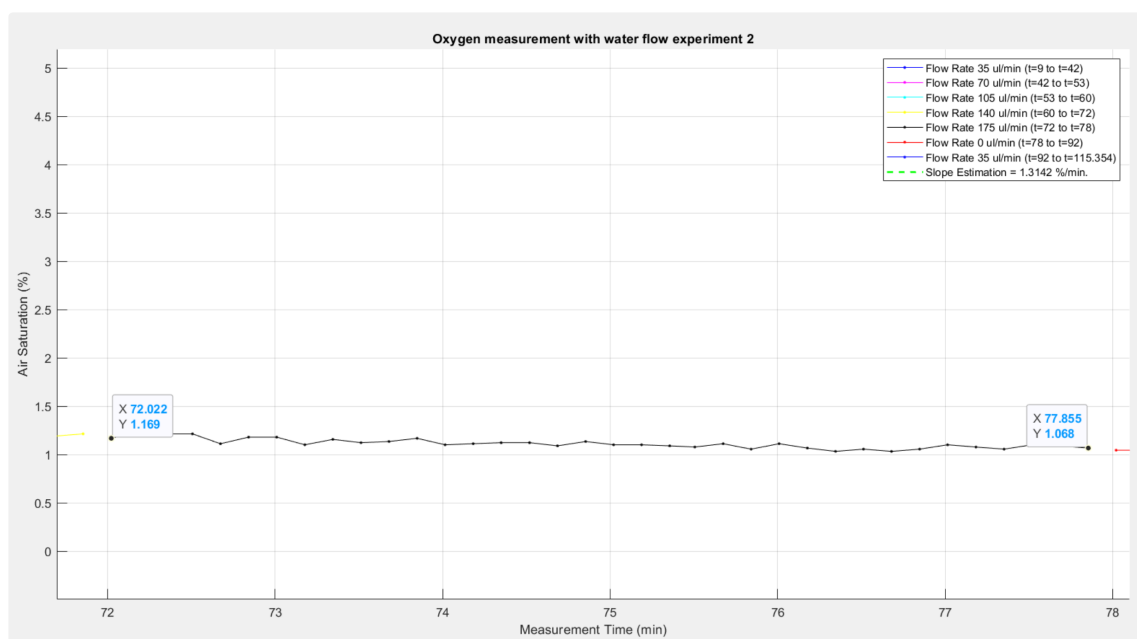[2] Dissolved Oxygen Probes, Solutions Accessories — Thermo Fisher Scientific - IE.

[3] Fiber Optic Perfusion Solution Monitoring (PreSens).

[4] Free textbooks online with no catch.

[5] Solubility o2 in h2o.

[6] William's e medium, no glutamine.

[7] AHYA, S. N., SOLER, M. J., LEVITSKY, J., AND BATLLE, D. Acid-base and potassium disorders in liver disease. In *Seminars in nephrology* (2006), vol. 26, Elsevier, pp. 466–470.

[8] AL-ANI, A., TOMS, D., KONDRO, D., THUNDATHIL, J., YU, Y., AND UNGRIN, M. Oxygenation in cell culture: Critical parameters for reproducibility are routinely not reported. *PloS one 13*, 10 (2018), e0204269.

[9] BAILEY, R. The anatomy and function of the human liver. https://www.thoughtco.com/liver-anatomy-and-function-4058938, June 2016. Accessed: 2022-12-30.

[10] BAVLI, D., PRILL, S., EZRA, E., LEVY, G., COHEN, M., VINKEN, M., VANFLETEREN, J., JAEGER, M., AND NAHMIAS, Y. Real-time monitoring of metabolic function in liver-on-chip microdevices tracks the dynamics of mitochondrial dysfunction. *Proceedings of the National Academy of Sciences 113*, 16 (2016), E2231–E2240.

[11] BOUWENS, L., DE BLESER, P., VANDERKERKEN, K., GEERTS, B., AND WISSE, E. Liver cell heterogeneity: functions of non-parenchymal cells. *Enzyme 46* (1992), 155–155.

[12] CARNEIRO, C., BRITO, J., BILREIRO, C., BARROS, M., BAHIA, C., SANTIAGO, I., AND CASEIRO-ALVES, F. All about portal vein: a pictorial display to anatomy, variants and physiopathology. *Insights into imaging 10*, 1 (2019), 1–18.

[13] CHEGWIDDEN, W. R., AND CARTER, N. D. Introduction to the carbonic anhydrases. *The carbonic anhydrases: new horizons* (2000), 13–28.

[14] Coluccio, M. L., Perozziello, G., Malara, N., Parrotta, E., Zhang, P., Gentile, F., Limongi, T., Raj, P. M., Cuda, G., Candeloro, P., et al. Microfluidic platforms for cell cultures and investigations. *Microelectronic Engineering 208* (2019), 14–28.

[15] Cornell, B. Liver structure, 2016.

[16] Editors, B. Liver (human anatomy): Overview, function, location, Mar 2019.

[17] eFunda, I. eFunda Directory Service: Company Details: PreSens Precision Sensing GmbH.

[18] Ehrlich, A., Duche, D., Ouedraogo, G., and Nahmias, Y. Challenges and opportunities in the design of liver-on-chip microdevices. *Annual review of biomedical engineering 21* (2019), 219.

[19] Eipel, C., Abshagen, K., and Vollmar, B. Regulation of hepatic blood flow: the hepatic arterial buffer response revisited. *Annals of Gastroenterology & Hepatology 9*, 96 (2011).

[20] Elhassan, S. Temperature control system for Organ-on-a-Chip applications, 2023.

[21] EngineerExcel. Loss coefficient for sudden contraction.

[22] Ghatkesar, M. K. Needle separation provided by, 2024. Personal communication.

[23] Hadanny, A., and Efrati, S. The hyperoxic-hypoxic paradox. *Biomolecules 10*, 6 (2020), 958.

[24] Huh, D., Torisawa, Y.-s., Hamilton, G. A., Kim, H. J., and Ingber, D. E. Microfluidic cell culture models for tissue engineering. *Nature reviews materials 1*, 1 (2010), 160–171.

[25] Jorns, C., Ellis, E., Nowak, G., Fischler, B., Nemeth, A., Strom, S., and Ericzon, B. Hepatocyte transplantation for inherited metabolic diseases of the liver. *Journal of internal medicine 272*, 3 (2012), 201–223.

[26] Kang, D., Hong, G., An, S., Jang, I., Yun, W.-S., Shim, J.-H., and Jin, S. Bioprinting of multiscaled hepatic lobules within a highly vascularized construct. *Small 16*, 13 (2020), 1905505.

[27] Kietzmann, T. Metabolic zonation of the liver: The oxygen gradient revisited. *Redox biology 11* (2017), 622–630.

[28] Lauschke, V., and Ingelman-Sundberg, M. Sinusoidal blood flow in the liver: regulation and physiological significance. *Experimental Cell Research 408*, 2 (2021), 112872.

[29] Ledezma, G., Folch, A., Bhatia, S., Balis, U., Yarmush, M., and Toner, M. Numerical model of fluid flow and oxygen transport in a radial-flow microchannel containing hepatocytes.

[30] Liao, C.-M., Chung, Y.-C., and Mu, C.-Y. An overview of dissolved oxygen sensors: calibration, uncertainties, and challenges. *Sensors 17*, 7 (2017), 1586.

[31] Liu, G., and Lin, Y. Microfluidic electrochemical devices for bioanalysis. *Talanta 103* (2013), 42–52.

[32] Lv, P., Le The, H., Eijkel, J., Van den Berg, A., Zhang, X., and Lohse, D. Growth and detachment of oxygen bubbles induced by gold-catalyzed decomposition of hydrogen peroxide. *The Journal of Physical Chemistry C 121*, 38 (2017), 20769–20776.

[33] Ma, L., Wu, Y., Li, Y., Aazmi, A., Zhou, H., Zhang, B., and Yang, H. Current advances on 3d-bioprinted liver tissue models. *Advanced healthcare materials 9*, 24 (2020), 2001517.

[34] Martin, N., and Michael, A. Oxygen scavenging system for cell culture solutions. *BioProcess International 10*, 8S (2012), 24–31.

[35] McKee, T. J., Perlman, G., Morris, M., and Komarova, S. V. Extracellular matrix composition of connective tissues: a systematic review and meta-analysis. *Scientific reports 9*, 1 (2019), 1–15.

[36] McKeown, S. Defining normoxia, physoxia and hypoxia in tumours—implications for treatment response. *The British journal of radiology 87*, 1035 (2014), 20130676.

[37] MEFANET, C., and medical faculties network, S. Bicarbonate buffer - WikiLectures.

[38] Nordson EFD. Optimum disposable reservoir systems. [Dataset], 2024.

[39] Online, B. Cellular respiration - Definition and Examples - Biology Online Dictionary, 6 2022.

[40] Park, J., Berthiaume, F., Toner, M., Yarmush, M. L., and Tilles, A. W. Microfabricated grooved substrates as platforms for bioartificial liver reactors. *Biotechnology and bioengineering 90*, 5 (2005), 632–644.

[41] Patroncini, D. *Water quality investigations of the River Lea (NE London)*. PhD thesis, 01 2013.

[42] Provenzano, M. R., Kunz, A., and Schäfer, H. Optimizing dissolved oxygen measurement in shake flasks: a comparative study of optical and electrochemical sensors. *Bioprocess and Biosystems Engineering 42*, 10 (2019), 1629–1639.

[43] Rahimi, P., and Moosavi-Nasab, M. Recent advances in dissolved oxygen sensing technologies: A review. *Journal of Electroanalytical Chemistry 870* (2020), 114266.

[44] Rehm, B., Consultant, D., Haghshenas, A., Paknejad, A. S., and Schubert, J. Chapter two - situational problems in mpd. In *Managed Pressure Drilling*, B. Rehm, J. Schubert, A. Haghshenas, A. S. Paknejad, and J. Hughes, Eds. Gulf Publishing Company, 2008, pp. 39–80.

[45] Sanyal, A. J., Boyer, T. D., Terrault, N., and Lindor, K. D. *Zakim and Boyer's hepatology: A textbook of liver disease*. Elsevier, 2018.

[46] Stravitz, R. T., and Larsen, F. S. Therapeutic hypothermia for acute liver failure. *Critical care medicine 37*, 7 (2009), S258–S264.

[47] Team, E. The basics of microfluidic tubing amp; sleeves, Oct 2022.

[48] Team, E. Materials for microfluidic chips fabrication : a review 2017 - Elveflow, 10 2022.

[49] Thorne, A. M., Ubbink, R., Brüggenwirth, I. M., Nijsten, M. W., Porte, R. J., and de Meijer, V. E. Hyperthermia-induced changes in liver physiology and metabolism: a rationale for hyperthermic machine perfusion. *American Journal of Physiology-Gastrointestinal and Liver Physiology 319*, 1 (2020), G43–G50.

[50] Underhill, G. H., and Khetani, S. R. Emerging trends in modeling human liver disease in vitro. *APL bioengineering 3*, 4 (2019), 040902.

[51] van Reeuwijk, M. Design of a miniature gas exchanger for oxygen control in microfluids: Design, integration, fabrication and validation of a miniature cell medium gas exchanger to control (sub) physiological oxygen concentrations on a liver chip.

[52] Wang, T., Lü, S., Hao, Y., Su, Z., Long, M., and Cui, Y. Influence of microflow on hepatic sinusoid blood flow and red blood cell deformation. *Biophysical Journal 120*, 21 (2021), 4859–4873.

[53] West, J. B. *Respiratory Physiology: The Essentials*. Wolters Kluwer Health/Lippincott Williams & Wilkins, 2013.

[54] Zhu, H. Portable and integrated organ-on-chip platform using off-the-shelf components.